Politecnico di Torino

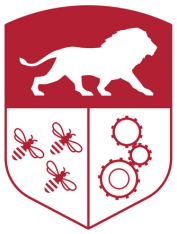

CENTRALE LYON

Doctoral Dissertation

Program in Energy Engineering (38th Cycle)

In international collaboration with Centrale Lyon

Nathan Cadot

Experimental and numerical study of gravity currents produced in polynyas

---

Supervisors:

Prof. Carlo Vincenzo Camporeale	Politecnico di Torino
Prof. Luca Ridolfi	Politecnico di Torino
Prof. Pietro Salizzoni	École Centrale de Lyon

Doctoral Examination Committee:

Prof. Luca Brandt	Politecnico di Torino
Prof.ssa Stefania Espa	Sapienza Università di Roma
Dott.ssa Maria Eletta Negretti	CNRS, LEGI Grenoble
Prof.ssa Donatella Termini	Università degli Studi di Palermo
Prof. Marco Toffolon	Università di Trento

La science, mon garçon, est faite d'erreurs, mais d'erreurs qu'il est bon de commettre, car elles mènent peu à peu à la vérité.

— ***Jules Verne,*** *Voyage au centre de la Terre*

Acknowledgment

I would like to express my deepest gratitude to my supervisors, Carlo Camporeale, Luca Ridolfi, and Pietro Salizzoni, for their invaluable guidance, insightful advice, and patience throughout the course of this thesis.

I am also grateful to Andrea Cagninei and Roberto Bosio for their essential technical support in the laboratory.

My sincere thanks go to my colleagues for their collaboration, encouragement, and the many enjoyable moments we shared together.

Finally, I wish to thank my family for their unwavering support and encouragement during all these years of study.

Abstract

Polynyas are large areas of open water within sea ice. Along the Antarctic coast, they are primarily formed by strong katabatic winds blowing from the continent, which drive sea ice away from the coast and allow new ice to form continuously. During ice formation, salt is rejected from the ice crystal lattice and released into the underlying ocean, a process known as brine rejection. This mechanism increases the salinity and density of the shelf waters. When polynyas form above the continental shelf, the densified water can cascade down the continental slope, ultimately reaching abyssal depths and contributing to the formation of Antarctic Bottom Water. This process plays a central role in driving the global thermohaline circulation, a key regulator of Earth's climate system.

In this thesis, the complexity of this phenomenon is addressed by separating it into two complementary parts. The first part focuses on the densification of water through brine rejection and its ability to generate buoyancy-driven flows. To this end, we developed a novel experimental apparatus capable of producing gravity currents driven exclusively by brine rejection. The experiments demonstrated that brine rejection alone is sufficient to generate gravity currents. Moreover, the results revealed that both flow rate and current thickness were greater without a slope than with one, and that the polynya size exerts a direct control on the current's discharge.

The second part of the thesis investigates the dynamics of cascading currents as they descend along a continental slope in a stratified environment. In such conditions, the current may arrest when it reaches a layer of equal density, with the maximum depth reached referred to as the penetration depth. The key parameters controlling this depth are the initial buoyancy of the current, the background stratification, and the slope angle. The slope angle controls the mixing of the current with the ambient fluid, which reduces its density. Using large-eddy simulations (LES), we examined the influence of slope angle on the penetration depth of turbulent gravity currents. The simulations successfully reproduced the results of previous laminar experiments, while also highlighting significant differences between laminar and turbulent regimes. Whereas slope angle had little effect in the laminar case, turbulent currents exhibited a strong dependence: penetration depth was maximized at intermediate slope angles (40–60°) and reduced at both small and steep slopes.

Résumé

Les polynies sont de vastes zones d'eau libre au sein de la banquise. Le long des côtes antarctiques, elles se forment principalement sous l'effet de forts vents catabatiques soufflant depuis le continent, qui repoussent la glace de mer au large et permettent la formation continue de nouvelle glace. Lors de la formation de glace, le sel est rejeté de la structure cristalline et libéré dans l'océan sous-jacent, un processus connu sous le nom de rejet de saumure. Ce mécanisme accroît la salinité et la densité des eaux de plateau. Lorsque les polynies se forment au-dessus du plateau continental, l'eau densifiée peut se déverser le long du talus continental, atteignant finalement les grandes profondeurs et contribuant à la formation de l'Eau de Fond Antarctique. Ce processus joue un rôle central dans la circulation thermohaline mondiale, l'un des principaux régulateurs du climat terrestre.

Dans cette thèse, la complexité de ce phénomène est abordée en le décomposant en deux volets complémentaires. La première partie se concentre sur la densification de l'eau par rejet de saumure et sur sa capacité à engendrer des écoulements de flottabilité. À cette fin, nous avons développé un dispositif expérimental original capable de produire des courants de gravité générés exclusivement par rejet de saumure. Les expériences ont montré que le rejet de saumure seul suffit à générer des courants de gravité. De plus, les résultats ont révélé que le débit et l'épaisseur des courants est plus important sans pente qu'avec, et que la taille de la polynie exerce un contrôle direct sur le débit du courant.

La seconde partie de la thèse étudie la dynamique des courants en cascade lorsqu'ils descendent le long d'un talus continental dans un environnement stratifié. Dans de telles conditions, le courant peut s'arrêter lorsqu'il atteint une couche de densité égale, la profondeur maximale atteinte étant appelée profondeur de pénétration. Les paramètres clés contrôlant cette profondeur sont la flottabilité initiale du courant, la stratification ambiante et l'angle de la pente. L'angle de la pente gouverne le mélange entre le courant et le fluide environnant, ce qui réduit sa densité. À l'aide de simulations aux grandes échelles (LES), nous avons étudié l'influence de l'angle de la pente sur la profondeur de pénétration des courants de gravité turbulents. Les simulations ont reproduit avec succès les résultats d'expériences laminaires antérieures, tout en mettant en évidence des différences significatives entre les régimes laminaire et turbulent. Alors que l'angle de la pente avait peu d'effet dans le cas laminaire, les courants turbulents ont montré une forte dépendance : la profondeur de pénétration est maximale pour des pentes intermédiaires (40–60°) et réduite pour des pentes faibles ou fortes.

Riassunto

Le polynie sono ampie aree di acqua libera all'interno della banchisa. Lungo le coste antartiche, si formano principalmente a causa dei forti venti catabatici provenienti dal continente, che spingono il ghiaccio marino al largo e permettono la formazione continua di nuovo ghiaccio. Durante la formazione del ghiaccio, il sale viene espulso dalla struttura cristallina e rilasciato nell'oceano sottostante, in un processo noto come brine rejection. Questo meccanismo aumenta la salinità e la densità delle acque di piattaforma. Quando le polynie si formano sopra la piattaforma continentale, l'acqua densificata può scendere lungo la scarpata continentale, raggiungendo infine le profondità abissali e contribuendo alla formazione dell'Acqua di Fondo Antartica. Questo processo svolge un ruolo fondamentale nell'alimentare la circolazione termoalina globale, uno dei principali regolatori del clima terrestre.

In questa tesi, la complessità di tale fenomeno viene affrontata separandolo in due parti complementari. La prima parte si concentra sulla densificazione dell'acqua dovuta alla brine rejection e sulla sua capacità di generare correnti di galleggiamento. A tal fine, abbiamo sviluppato un nuovo apparato sperimentale in grado di produrre correnti di gravità generate esclusivamente dalla brine rejection. Gli esperimenti hanno dimostrato che la sola brine rejection è sufficiente a generare correnti di gravità. Inoltre, i risultati hanno rivelato che sia la portata che lo spessore delle correnti è più importante senza pendenza che con una, e che la dimensione della polynya esercita un controllo diretto sulla portata del flusso.

La seconda parte della tesi analizza la dinamica delle correnti in cascata quando scorrono lungo una scarpata continentale in un ambiente stratificato. In tali condizioni, la corrente può arrestarsi quando raggiunge uno strato di pari densità, e la profondità massima raggiunta viene chiamata profondità di penetrazione. I parametri chiave che controllano tale profondità sono la galleggiabilità iniziale della corrente, la stratificazione ambientale e l'inclinazione della pendenza. Quest'ultima regola il rimescolamento della corrente con il fluido circostante, riducendone la densità. Utilizzando simulazioni a grandi vortici (LES), abbiamo studiato l'influenza dell'inclinazione della pendenza sulla profondità di penetrazione delle correnti di gravità turbolente. Le simulazioni hanno riprodotto con successo i risultati di precedenti esperimenti laminari, mettendo tuttavia in evidenza differenze significative tra i regimi laminare e turbolento. Mentre nel caso laminare l'angolo della pendenza aveva scarso effetto, le correnti turbolente hanno mostrato una forte dipendenza: la profondità di penetrazione risulta massima per inclinazioni intermedie (40–60°) e ridotta per pendenze deboli o molto ripide.

List of acronyms

AABW: Antarctic Bottom Water
AAIW: Antarctic Intermediate Water
AASW: Antarctic Surface Water
ACC: Antarctic Circumpolar Current
AMOC: Atlantic Meridional Overturning Circulation
ASC: Antarctic Slope Current
ASBW: Antarctic Shelf Bottom Water
CDW: Circumpolar Deep Water
CFD: Computational Fluid Dynamic
DAQ: Data Acquisition system
DNS: Direct Numerical Simulation
DSW: Dense Shelf Water
FEM: Finite Element Methods
GOC: Global Overturning Circulation
HSSW: High-Salinity Shelf Water
ISW: Ice Shelf Water
LES: Large Eddies Simulation
LIF: Laser-Induced Fluorescence
MPT: Mid-Pleistocene Transition
NADW: North Atlantic Deep Water
NEW: Northeast Water
NGCC: Northeast Greenland Coastal Current
PIV: Particle Image Velocimetry
PSU: Practical Salinity Unit
RANS: Reynolds Averaged Navier-Stokes
THC: Thermohaline Circulation

List of symbols

Roman symbols

B: integral buoyancy
B_l: buoyancy flux by unit length
C_D: drag coefficient
C_k: a coefficient measuring the efficiency of the local shear production
C_s: a coefficient parameterizing the efficiency of the boundary-introduced turbulent kinetic energy
D: penetration depth
D_a: nondimensional penetration depth
g: constant of gravity of Earth
g': reduced gravity
H: thickness of the current
L: Opening size of the polynya in part 1 and Distance of the source to the wall in part 2
M: momentum flux
N: Brunt–Väisälä frequency that represents the intensity of the stratification
P: pressure
Q: volume flux
q: flow rate by unit length
S: salinity
T: temperature
t: time
u: velocity in the x direction
v: velocity in the y direction
w: velocity in the z direction

Greek symbols

α: entrainment coefficient
β_P: compressibility coefficient
β_S: saline contraction coefficient
β_T: thermal expansion coefficient
E_{eq}: entrainment per unit depth $E_{eq} = \alpha(\theta)/\sin(\theta)$
ρ: density
θ: slope angle

Contents

Preambule

Marine currents play a fundamental role in shaping the circulation of the world's oceans and, by extension, the Earth's climate system. Their formation is governed primarily by two forcings: wind stresses and buoyancy fluxes. Wind acts as a mechanical driver, transferring momentum to the ocean surface and generating flows ranging from small-scale drifts to basin-wide gyres. In contrast, buoyancy forcing originates from variations in temperature and salinity that control seawater density. Surface heating and cooling, freshwater input from precipitation or ice melt, and salinization processes such as evaporation or brine rejection all contribute to these density contrasts. While wind forcing drives the rapid adjustment of surface layers, buoyancy forcing underpins the slower but far-reaching thermohaline circulation, which ventilates the deep ocean and redistributes heat, carbon, and nutrients across basins. The interplay of these two mechanisms establishes the backbone of global ocean circulation, linking surface processes to the abyss.

This thesis focuses specifically on buoyancy-driven oceanic flows, with particular emphasis on those generated by polynyas. It was conducted as a collaboration between the Politecnico di Torino (Italy) and Centrale Lyon (France). Experimental investigations were carried out at the Politecnico di Torino to study buoyancy generation in polynyas through brine rejection. Complementarily, numerical simulations were performed using the computational cluster at Centrale Lyon to investigate the development of buoyancy-driven flows along a sloping boundary in a stratified ambient environment.

The thesis begins with an introductory part. The second part is concerned with the gravity currents induced by polynyas: it contains a review of the literature on polynyas and a description of the experiment performed, as well as the results obtained. The third part is dedicated to the gravity penetration depth of gravity currents flowing along a slope into a stratified ambient: it contains a review of the literature on gravity currents, an explanation of the numerical methods, a validation of our code against experimental data, and the results obtained with our simulations. Finally, some conclusions are drawn at the end of the thesis.

I Introduction

Buoyancy-driven currents formed in coastal polynyas play an important role in the global climate system. When sea ice forms, it increases the salinity and density of the surrounding water, causing it to sink and flow along the seafloor. These dense flows help to drive large-scale ocean circulations, transporting heat, salt, and nutrients. By connecting surface processes with the deep ocean, these currents contribute to the redistribution of energy and matter on a planetary scale, making them a key element in regulating the climate.

In this Introduction, we present polynyas and discuss how they influence the global climate by generating buoyancy-driven ocean currents.

1 Polynyas

Polynyas are extensive areas of open water or thin ice that recur annually at specific geographic locations, persisting through both summer and winter (see Figure 1). The word polynya comes from a russian term for 'ice hole'. Winter polynyas are particularly remarkable, as the presence of open water and minimal ice cover under extremely cold and windy conditions appears counterintuitive. These features represent striking natural phenomena, comparable in their physical intensity and impact to events such as tornadoes, severe storms, or flash floods.

A polynya can vary in dimensions, but the largest ever recorded is the Weddell Sea polynya, which opened in the winters of 1974-1976. At its maximal extent, it reached up to 300,000 km^2 or roughly the size of Italy.

Polynyas have an important impact locally. The intense heat loss to the atmosphere over polynyas modifies local temperature gradients and can affect regional wind patterns and cloud formation [212]. The albedo of the polynya, being much smaller than the surrounding area, also plays a role in the local temperature of the water.

Polynyas are extremely important to the local fauna and flora. Especially in winter, they may be the only points of contact between water and air for hundreds of kilometers around. Enhanced light penetration and nutrient upwelling enable early-season phytoplankton blooms, forming the basis for rich and productive food webs [116]. These blooms support high densities of zooplankton, fish, seabirds, and marine mammals, including key Arctic species such as narwhals, walruses, and polar bears [188]. In the Antarctic, the Ross Sea and Weddell Sea polynyas are vital feeding and breeding grounds for penguins and seals [122].

Climate change, however, poses a significant threat to the stability and function of polynyas. Recent studies indicate changes in the frequency, size, and duration of polynya events, driven by warming ocean temperatures and altered wind regimes [77, 119]. These shifts have cascading ecological impacts, disrupting bloom timing, altering species distributions, and threatening the resilience of indigenous communities who depend on predictable marine productivity for subsistence [76, 121].

2 Cascading of Dense Shelf Water

A distinctive feature of sea-ice formation is the phenomenon known as brine rejection. The crystalline structure of ice excludes dissolved salts, preventing their incorporation into the solid phase. As a result, the salt present in seawater is expelled into the underlying liquid layer [210]. This process locally increases the salinity of the water, thereby enhancing its density, since saltier water is denser. This phenomenon has important consequences in the case of coastal polynyas.

The coastal polynyas of Antarctica are often located above the continental shelf. A continental shelf is the submerged, gently sloping extension of a continent that stretches from the shoreline to the point where the ocean floor drops steeply into the deep ocean basin (the continental slope with a typical slope angle of around 4°). Off the coasts of Antarctica, those shelves can be hundreds of kilometers long and usually 500 meters deep. If a polynya is located above one such area, the salt from the brine rejection can accumulate and form what is called a Dense Shelf Water (DSW) [218]. These dense shelf waters can also be produced or co-produced by the input of supercooled water from ice-ocean interactions at the base of floating ice shelves [87]. Supercooled water refers to a liquid state in which the temperature falls below its equilibrium freezing point, given the local pressure, salinity, and other thermodynamic conditions, yet the water remains unfrozen. Floating ice shelves are extensions of the ice cap that continue over the water. Their temperature is usually very low, much lower than the surrounding water. If there is not too much turbulence or impurity in the water, it can cool past

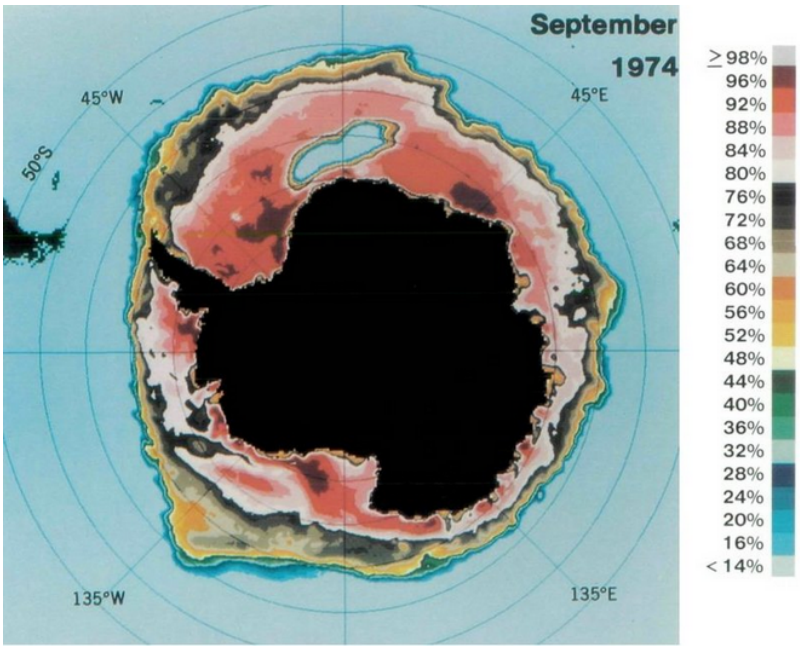

Fig. 1: The Weddell Sea polynya in the Austral winter, September 1974. Violet and red correspond to a high sea ice concentration, and light blue to open ocean. The Weddell Sea polynya is visible across the Greenwich meridian. Reproduced from [227].

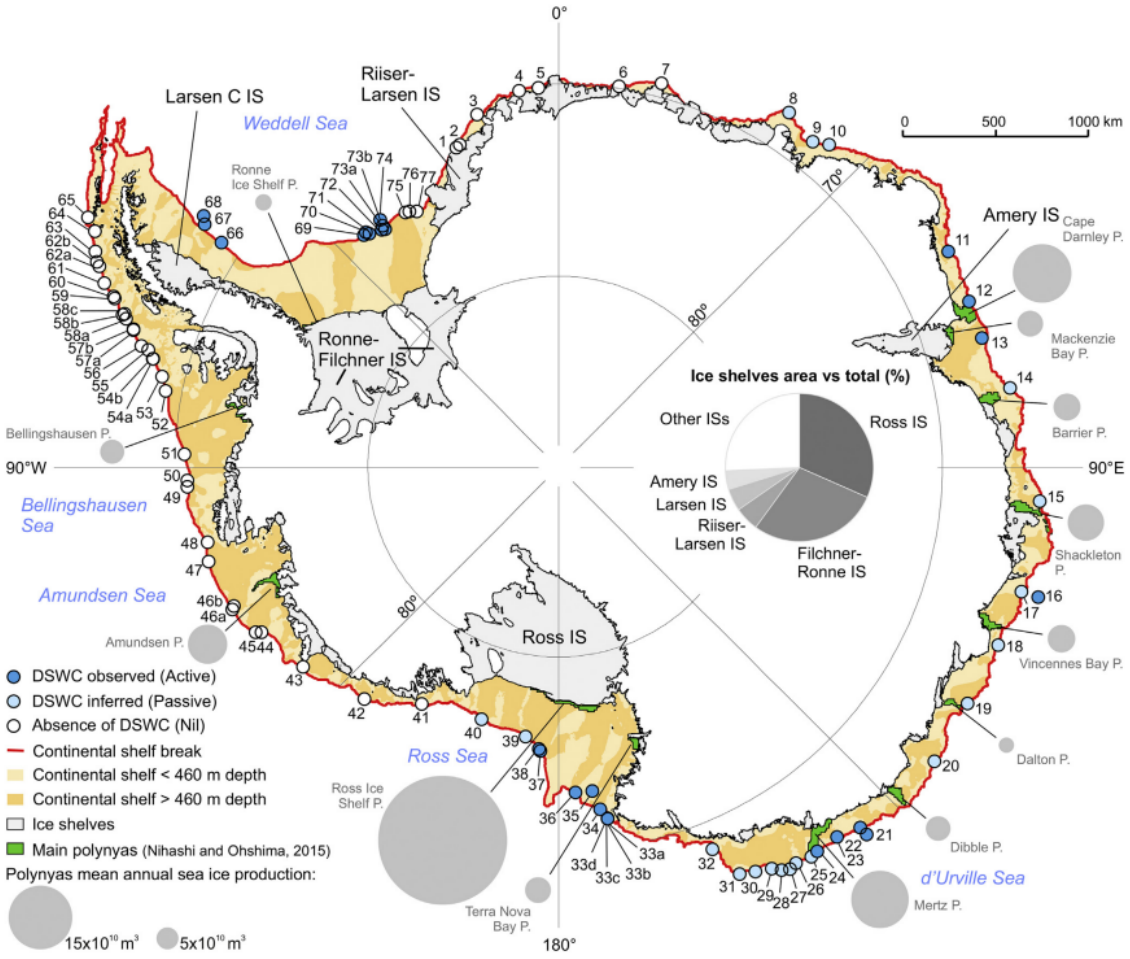

Fig. 2: Location of water column observations showing the presence or absence of dense shelf-water downslope flows around Antarctica. The coastline and ice shelf areas are derived from the SCAR Antarctic Digital Database. The 460 m contour and the continental shelf break are based on IBCSO v. 1.0 [10]. The major coastal polynyas and values of mean annual sea ice production are taken from [142]. The size of the grey circles is proportional to the polynyas' sea ice production. IS is ice shelf; P is polynya. Reproduced from [6].

the freezing point and become supercooled. The supercooled water is also heavier than the rest of the water, contributing to the densification of the shelf water.

In some specific conditions that are still not completely known, the DSW can flow down the continental slope. The current can go down to the bottom of the ocean, where it forms what is called Antarctic Bottom Water (AABW). To be able to go down to the bottom of the ocean and not be stopped at a middle depth, the DSW outflow needs to be very heavy and so very salty. It is generally believed that a large continental shelf is necessary for the accumulation and concentration of dense waters.

The most recent literature review on the role of the physiographic influences on the formation of deep waters was published by D. Amblas and J.A. Dowdeswell in 2018 [6]. They showed that there is a very clear relationship between the DSW cascade and polynyas distribution (see Figure 2). Contrary to previously held beliefs, it was found that the presence of large ice shelves or vast continental shelves was not necessary, although they were related to the biggest outflows. Indeed, some DSW cascades were found in areas with a very small continental shelf. These areas were named 'polynya only' by

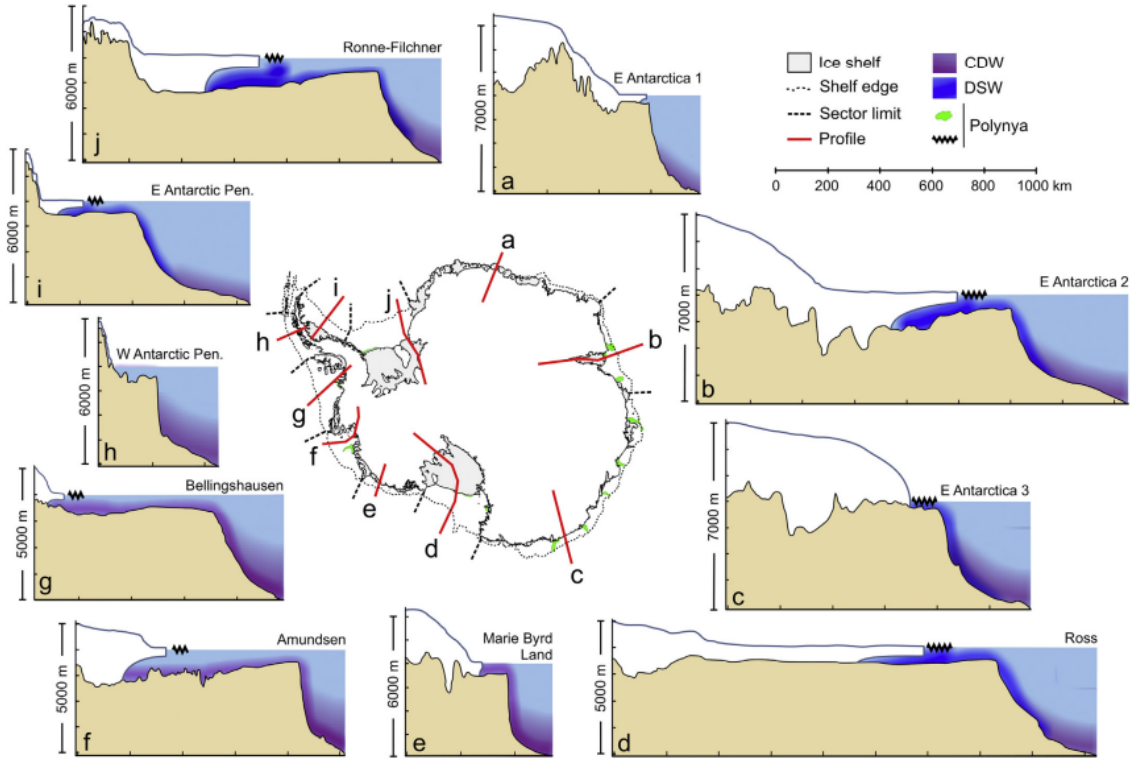

Fig. 3: Sketch of the modern setup of DSW cascades (in blue) and CDW inflows (in purple) in the different Antarctic sectors considered. The distribution of DSW and CDW is based on the observations reviewed in [6] and on the estimated average sea-floor potential temperatures map published in [166], respectively. The topographic and bathymetric profiles have been calculated from the IBCSO v1.0 grid [10] and the subglacial bed elevation from the Bedmap2 grid [70]. The profiles follow main ice-sheet flow directions, cross-shelf trough axes, and slope drainage morphologies, whenever present. The sub-ice shelf cavity delineations are approximate. Reproduced from [6].

the authors. A comparison of the different continental shelves and their effect on the creation of deep water can be found in Figure 3.

The total production of DSW by polynyas is estimated to be approximately 5.4 Sv (1 Sv = 10^6 m^3 s^{-1}) [147]. These Dense Shelf Waters descend the continental slope and mix with the overlying Circumpolar Deep Water, contributing to the formation of Antarctic Bottom Water and increasing its total volume. The global production rate of AABW is estimated to range between 15 and 20 Sv, with regional contributions of approximately 50–60% from the Weddell Sea, 30–40% from the Ross Sea, and the remaining 10% from the Adélie Coast.

3 Impact of polynyas on climate

3.1 The thermohaline circulation

The cascading formation of AABW from DSW is part of a larger, worldwide circulation pattern: the Global Overturning Circulation (GOC). The GOC's main driving mechanism and network of currents is the thermohaline circulation (THC). The thermohaline circulation is driven, as the name indicates, by differences of temperature (thermo) and salinity (haline). The THC connects the different oceans as well as their surface and deep layers. The GOC also includes other wind-driven surface currents that are not part of the THC. Figure 4 is a schematic view of the GOC.

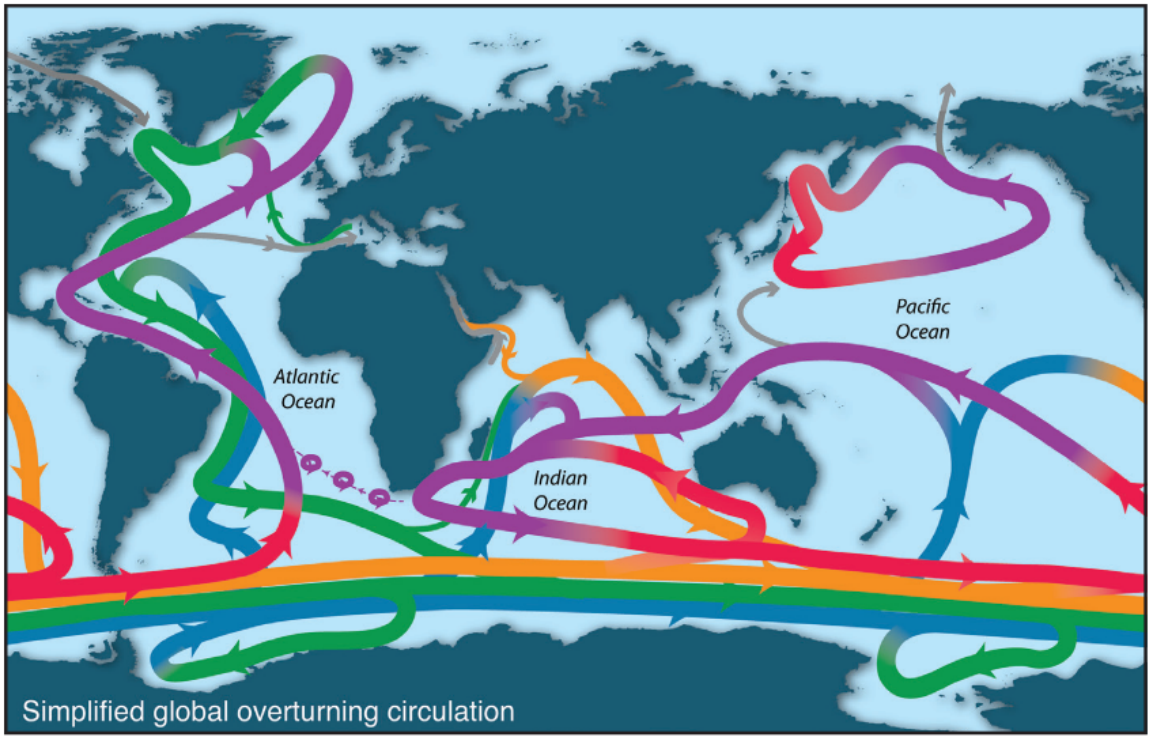

Fig. 4: Schematic of the overturning circulation by Talley et al. [193]. Purple = upper ocean and thermocline. Red = denser thermocline and intermediate water. Orange = Indian Deep Water and Pacific Deep Water. Green = North Atlantic Deep Water. Blue = Antarctic Bottom Water. Gray = Bering Strait components and Mediterranean and Red Sea inflows

The THC begins in high-latitude regions, primarily in the North Atlantic (Labrador and Nordic Seas) and around Antarctica, where cold, salty, and thus dense waters sink to great depths, forming North Atlantic Deep Water (NADW) and Antarctic Bottom Water (AABW), respectively. These water masses spread throughout the deep ocean basins, flowing along the seafloor toward the equator and into other basins.

As deep waters flow and mix, they slowly upwell in the Indian and Pacific Oceans, especially in the Southern Ocean, where strong westerly winds and the Antarctic Circumpolar Current (ACC) drive Ekman divergence (an area where two divergent currents provoke the upwelling of underneath waters), allowing deep waters to rise to the surface. Upwelling also occurs along the equator and eastern ocean boundaries, but it is in the Southern Ocean that most deep and bottom waters return to the surface, forming the primary 'upwelling engine' of the THC. These upwelled waters are then modified by air-sea interaction – gaining heat and freshwater – and are eventually transported back toward the poles via surface currents, completing the global overturning loop.

The THC exerts a profound influence on the global climate system by redistributing heat, freshwater, and carbon between the ocean surface and deep interior, and across latitudes. A key component of the THC is the Atlantic Meridional Overturning Circulation (AMOC). The AMOC is one of the reasons why western Europe is warmer than other regions (such as Canada) at similar latitudes.

The formation of AABW plays another crucial role for climate: the sequestration of CO_2 in the deep ocean. Indeed, the cascading of dense water along the continental slope carries with it some CO_2, which is subsequently trapped in the deep ocean. The carbon in the water comes from two main sources: dissolved inorganic carbon, CO_2 absorbed by the water due to its contact with the

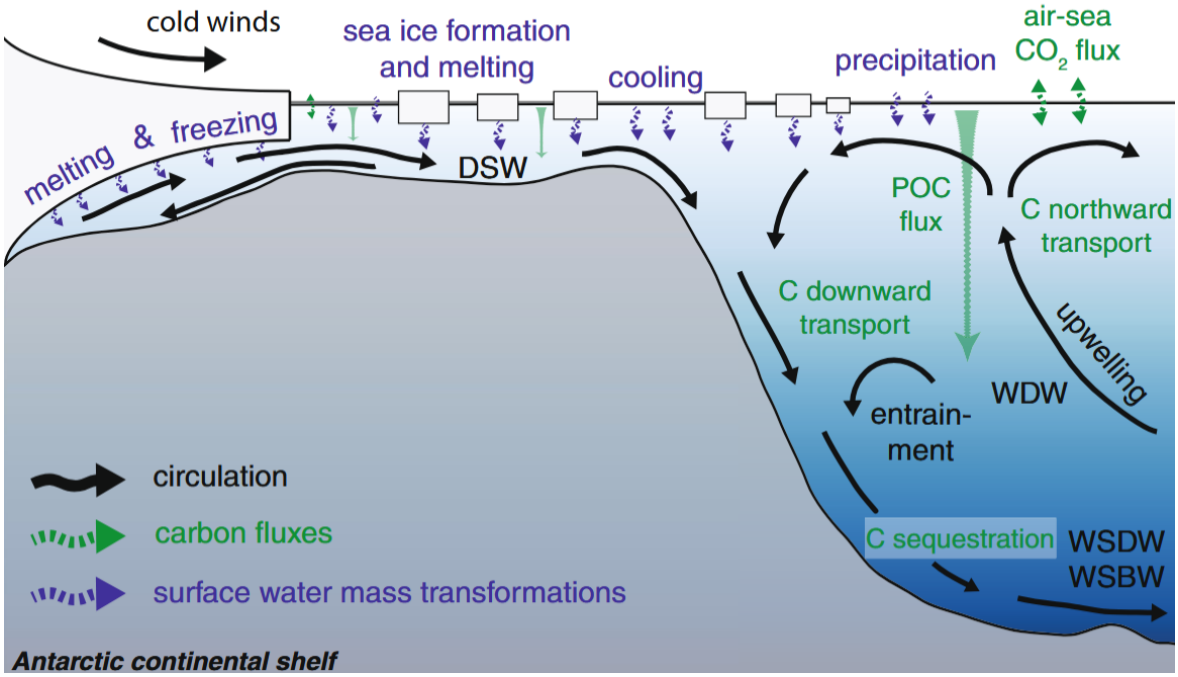

Fig. 5: Typical section from the Antarctic continent, with general features of the overturning circulation sketched in black. Highlighted in blue are surface water mass transformations by buoyancy fluxes, and carbon fluxes are marked in green. CDW Circumpolar Deep Water, WDW Warm Deep Water, WSDW Weddell Sea Deep Water, WSBW Weddell Sea Bottom Water, DSW Dense Shelf Water, POC particulate organic carbon. Adapted from [143].

atmosphere, and organic carbon. This organic carbon is made of shells of some plankton species, dead phytoplankton, and feces. Near the surface of the ocean and especially so in polynyas, there is a strong biological activity. Phytoplankton and bacteria consume CO_2 and transform it into organic matter (mostly made of carbon). These small animals are then eaten or die and sediment. The process of sedimentation or currents like that formed in polynyas can bring this organic matter to the depth of the ocean. This process is known as the biological pump.

It is estimated that Antarctic polynyas absorb atmospheric CO_2 at a rate of around 50 Tg C/yr (teragrams or 10^{12} grams of carbon per year) [143, 169]. The Southern Ocean as a whole absorbs around 1000 Tg C/yr [219] (human activities reject around 10,000 Tg C/yr). Antarctic polynyas overall have a disproportional share of the CO_2 sink for their modest surface [135].

3.2 Possible influence of polynyas on ice age cycles

The Earth's climate has undergone profound and recurrent shifts over geological time, with the Quaternary Period (the last 2.6 million years) distinguished by the repeated alternation between extended glacial phases, during which vast ice sheets advanced over large parts of the continents, and comparatively brief interglacial intervals, characterized by warmer conditions and significant ice-sheet retreat. These cycles left an unmistakable imprint in marine sediment cores, ice cores, and terrestrial deposits, revealing a complex interplay between external forcing and internal climate feedbacks [62, 161]. Figure 6 illustrates the evolution of global temperature and ice volume over the past 450 thousand years, relative to present-day values. The alternation between warmer interglacial phases and colder glacial periods is clearly apparent. A foundational explanation for the pacing of these glacial–interglacial

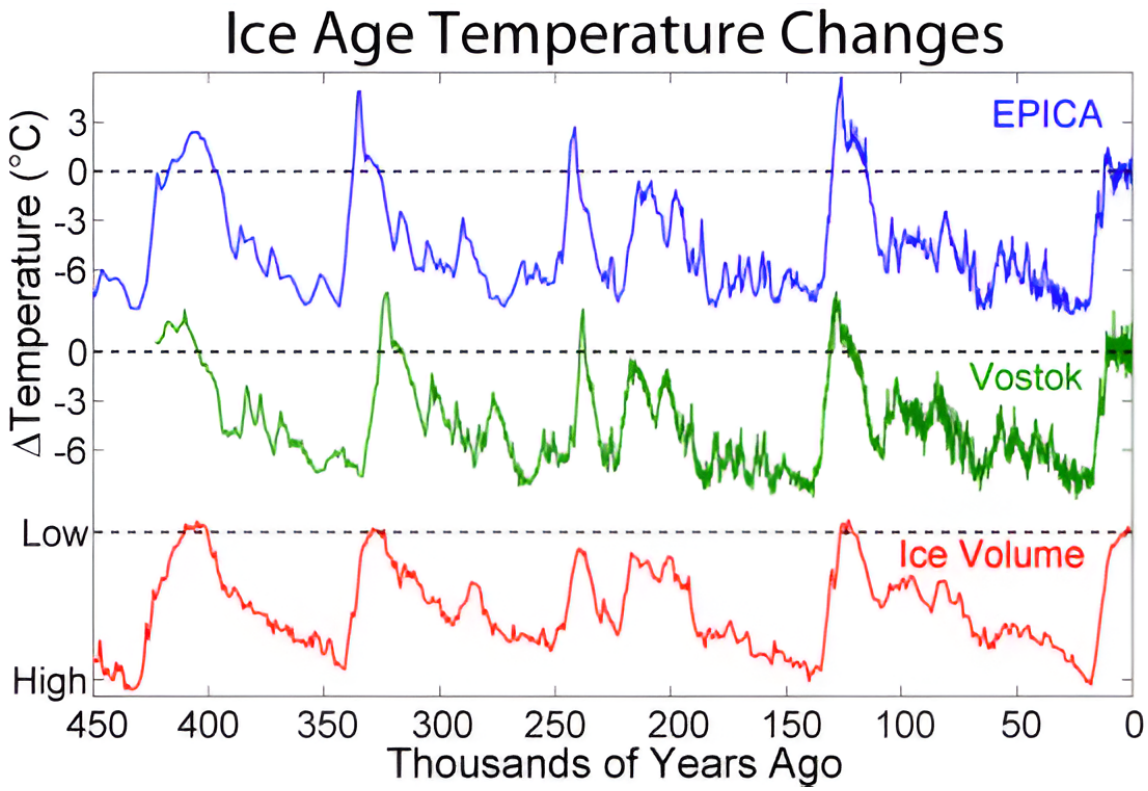

Fig. 6: Temperature and ice volume compared to modern times in the last 450 thousand years. The data come from the station EPICA [62] and Vostok [161] ice cores. Reproduced from Wikipedia.

oscillations was provided by Milutin Milankovitch in the early 20th century [127]. His astronomical theory links the timing of major climate transitions to periodic variations in Earth's orbital parameters: eccentricity, describing the shape of Earth's orbit around the Sun and varying on timescales of ∼100 kyr (10^3 years); obliquity, the tilt of Earth's axis relative to its orbital plane, which oscillates on a ∼41 kyr cycle; and precession, the slow wobble of Earth's rotational axis, occurring on cycles of ∼19–23 kyr. These parameters collectively modulate the seasonal and latitudinal distribution of incoming solar radiation (insolation), with the strongest climatic impact thought to occur in the high northern latitudes, where changes in summer insolation directly influence the survival or melting of winter snow cover and, by extension, the growth or retreat of ice sheets.

While the Milankovitch framework has proven remarkably successful in explaining the overall pacing of glacial–interglacial transitions, it fails to account for several key aspects of the paleoclimate record [71]. Notably, it does not fully explain the rapidity and magnitude of glacial terminations, during which global temperatures and atmospheric CO_2 levels rose sharply within a few thousand years [150]. Furthermore, the dominance of the ∼100 kyr cycle over the past million years – the so-called '100-kyr problem' – is not readily reconciled with the relatively weak direct radiative effect of eccentricity variations [196]. The Mid-Pleistocene Transition (MPT), around 1 million years ago, during which the climate system shifted from predominantly 41 kyr cycles to longer, more intense 100 kyr cycles without a corresponding change in orbital forcing, also remains unexplained within the original astronomical theory [91]. These limitations point to the involvement of amplifying mechanisms within the climate system itself, operating in concert with orbital forcing, and have driven extensive research into the roles of ice-sheet dynamics, ocean circulation, atmospheric CO_2, and other feedback processes in shaping the glacial–interglacial rhythm.

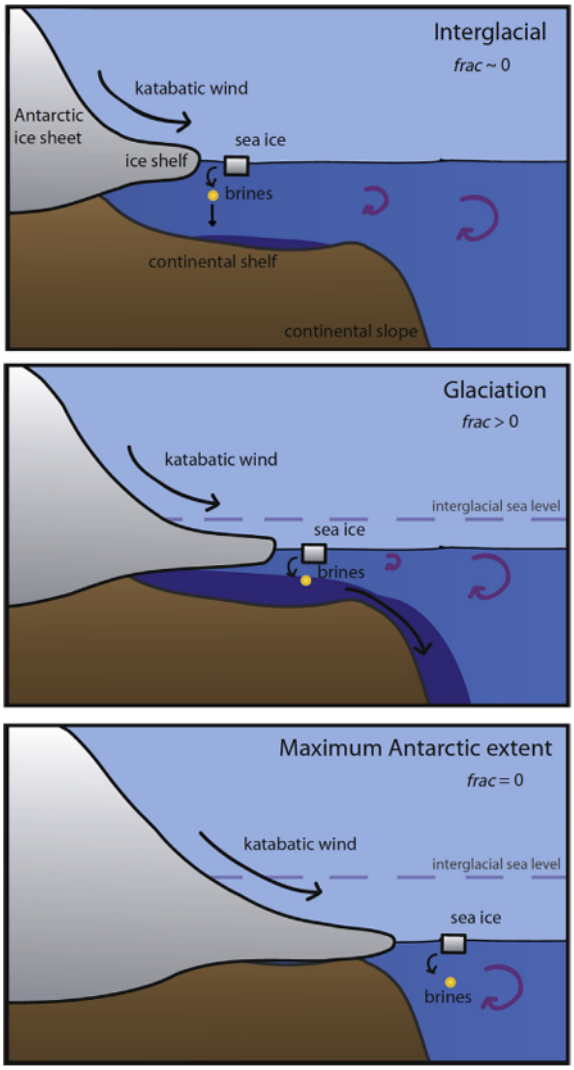

Fig. 7: Schematic representation of the sinking of brines during (a) interglacial, (b) glacial, and (c) deglacial periods. The main drivers of the quantity of dense water sinking to the deep ocean are the Antarctic ice sheet extent on the continental shelf and sea level, which govern the volume of water above the continental shelf. The less water there is, the less brine is mixed, and the more they can sink to the deep ocean. When sea ice formation is shifted to the open ocean, brines are mixed, and the sinking stops. Reproduced from [23].

Among the proposed hypotheses, Didier Paillard introduced a conceptual framework that integrates astronomical forcing with threshold-driven switches in the climate system, placing the Southern Ocean at the core of glacial–interglacial dynamics [149]. In this view, cooling and ice-sheet growth are initiated in the Northern Hemisphere by orbital forcing, but the onset of deglaciation is governed by processes in the Southern Hemisphere, in particular those involving Antarctic Bottom Water formation through brine rejection. During glacial maxima, extensive sea ice formation around Antarctica produces dense, saline brines that sink to the abyss, strengthening ocean stratification and isolating deep CO_2-rich waters from the atmosphere. This sequestration of carbon reinforces cooling and stabilizes the glacial state. Paillard's theory posits that the collapse of this brine-induced stratification is the trigger for rapid deglaciation. Once a critical threshold is reached through a combination of increasing Southern Hemisphere insolation, retreat of the Antarctic ice sheet, and freshening of surface waters from melting ice, the brine pump weakens or ceases. The resulting breakdown of deep-ocean

stratification releases the stored CO_2 back into the atmosphere, initiating a strong positive feedback that drives rapid warming and ice-sheet retreat. The whole mechanism is schematically summarized in Figure 7.

Although Paillard's conceptual framework is not the most widely adopted explanation for glacial–interglacial dynamics, a growing body of paleoclimatic evidence provides substantial support for its underlying mechanisms. Modeling work demonstrates that reproducing the last deglaciation requires a rapid cessation of brine sinking, which accounts for a significant portion of the observed atmospheric CO_2 rise [104]. Isotopic records from the Weddell Sea reveal the absence of AABW export during glacial maxima, pointing to a fundamentally different deep-ocean circulation and highlighting the importance of its resumption during deglaciation [95]. Fully coupled Earth system simulations indicate that a salty deep ocean is a prerequisite for glacial termination, amplifying the warming response to a weakening Atlantic Meridional Overturning Circulation [103]. Multiple studies confirm that the deep Southern Ocean was more stratified and less ventilated during glacial periods, consistent with a deep-ocean carbon reservoir sustained by brine rejection [222]. New isotopic data confirm that this stratification broke down during deglaciation due to a trigger in the Southern Hemisphere, which then released CO_2 into the atmosphere and contributed to the end of the ice age [17].

Thus, the polynyas might have played a very important role in the climate of the past in addition to their crucial role today. This makes it even more important to understand and study them properly.

3.3 Climate change impact on polynyas

If polynyas have an important impact on the climate system, the changes in the climate system could also have an important impact on them. The fate of polynyas in the future is uncertain. The poles are the areas of the globe where warming is occurring at the fastest rate [189]. The areas covered by sea ice have decreased significantly over the last 20 years and are expected to continue decreasing [74, 157]. The ice thickness has also been reduced significantly as multi-year ice tends to disappear in favor of young ice [120].

A primary expectation is that polynyas will become more frequent as climate change progresses. Sea ice in the polar regions is becoming thinner and less compact, which enhances its mobility and increases the susceptibility of the ice cover to atmospheric and oceanic forcing. As a result, mechanically forced polynyas may increase in both size and duration [31].

The reduction of sea ice also means that polynyas that occurred in areas that are no longer covered by ice technically vanish. Some polynya could disappear in areas still covered by ice. Indeed, some polynyas depend on ice-bridges to prevent ice from entering open-water areas. If these ice-bridges melt, these polynya may well not form anymore. This already happened to the Northeast Water Polynya off the coast of Greenland, which no longer exists in the form it had in the 1990' [75].

The changes in climate may well change the timing of the opening and closing of polynyas. This could prove disastrous to many species. Indeed, polynyas are biologically productive oases in the polar oceans, supporting early-season phytoplankton blooms and serving as feeding and breeding grounds for a wide range of marine organisms, including birds and mammals.

Earlier and longer polynya openings may decouple established trophic relationships – for instance, leading to mismatches between peak primary production and the life cycles of key grazers such as zooplankton. This could cascade through the food web, affecting fish, seabirds, and marine mammals that depend on the reliable seasonal productivity of polynyas [58].

Another important impact of climate change is on the production of DSW and its potential cascading along the continental slope. The melting of the ice cap (made of fresh water) significantly decreases the salinity of the shelf waters [167]. With climate change, this could mean the end of AABW formation. Since 1992, a 30% reduction of Weddell Sea Bottom Water volume was measured [225]. The formation of frazil ice in coastal polynyas could also be reduced with higher temperatures, leading to less brine rejection and so less densification of the shelf water [2]. The warming of Circumpolar Deep Water could also be a factor in the freshening of other shelf waters. Circumpolar deep waters can intrude onto the Antarctic shelf, and if they are warm, they can increase the basal melting of ice shelves and add further freshwater into the system [5].

The consequences of the AABW formation would be numerous, as it is one of the main drivers of the thermohaline circulation. The collapse of the global overturning circulation would have consequences difficult to assess, as it is such an important factor in regulating global heat balance. A more concrete consequence would be the warming of the deep ocean and its subsequent thermal expansion, which could lead to sea level rise [129].

The question of whether the AABW formation will stop and, if so, when is still debated. Different models give different predictions [180]. Recent anomalous climatic events have increased the production of AABW in the Ross Sea (Antarctica) [9, 181], further proving the complexity of these phenomena.

4 Outflows in the wider context of gravity currents

The cascading of Dense Shelf Water along the continental slope of Antarctica is not an isolated case. Similar processes occur in other regions of the world ocean, where dense waters formed on continental shelves or in marginal seas descend along topographic gradients, contributing to deep and bottom water masses.

In the North Atlantic, the Denmark Strait Overflow and Faroe Bank Channel Overflow are prominent examples of dense-water cascades, where chilled, saline waters from the Nordic Seas spill into the deep Atlantic, forming North Atlantic Deep Water (NADW) [85, 191]. These overflows are driven by similar thermohaline mechanisms as Antarctic DSW, though without direct sea-ice influence.

Meanwhile, the Mediterranean Outflow represents a contrasting case, where warm, hypersaline water exits the Strait of Gibraltar and plunges into the intermediate depths of the Atlantic, creating a distinct water mass that spreads across the basin [16].

Even in the Arctic, cascading phenomena occur, such as the outflow of brine-enriched shelf water from the Barents and Kara Seas [177], which contributes to the formation of Arctic Intermediate Water.

All of these flows fall within the broader category of gravity currents: fluid motions driven by horizontal density gradients. Such gradients may arise from variations in salinity, temperature, suspended particle concentration, or even differences between immiscible fluids. Gravity currents are ubiquitous in both geophysical and anthropogenic contexts. Natural examples include sea breezes, katabatic winds, avalanches, pyroclastic flows, sandstorms, thunderstorm outflows, tidal bores, and turbidity currents. Human-driven cases include oil spills, brine discharge in estuaries, wastewater release into rivers or oceans, and accidental leakage of dense gases in mines.

Some gravity currents can be extremely impressive and have disastrous consequences. Such examples include the PEMEX oil well leak in the Gulf of Mexico in 1979 (see Figure 8). The oil, lighter than water and heavier than air, floated up to the surface and spread at the interface between water and

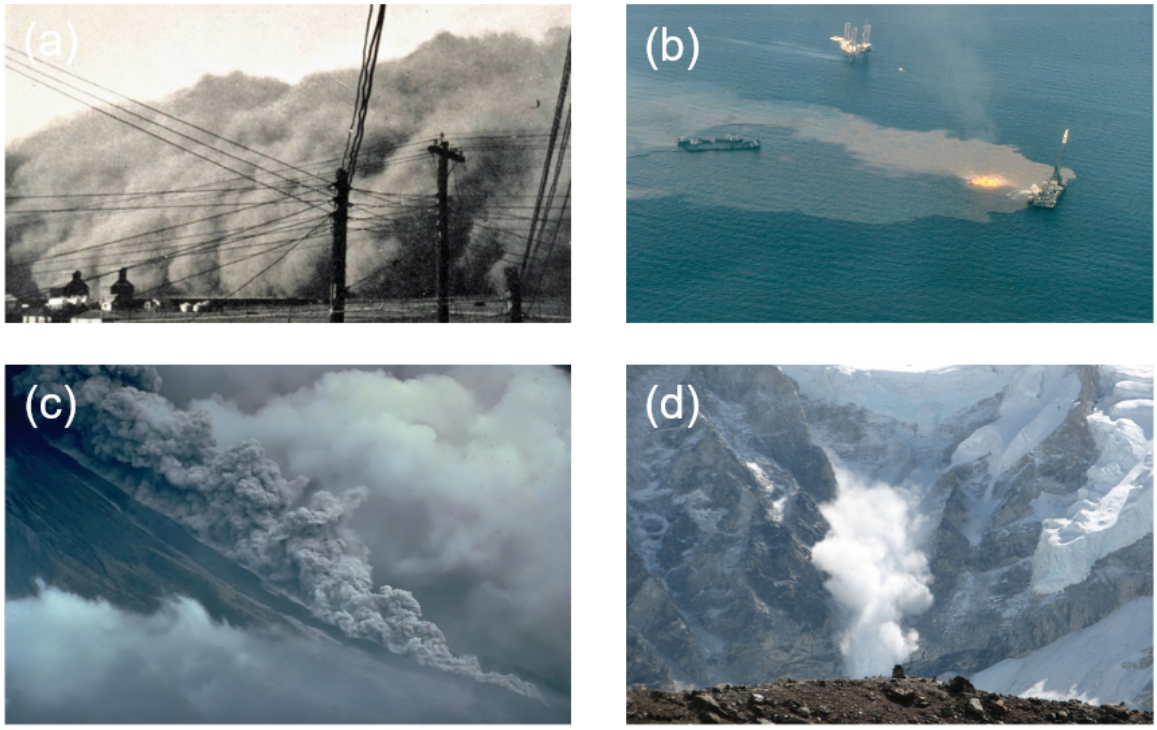

Fig. 8: Example of gravity currents in the natural and industrial environment: (a) A sand storm in Texas in 1935, (b) an oil spillage in the Gulf of Mexico in 1979, (c) a pyroclastic flow down the flanks of the Mayon volcano in the Philippines in 1984, (d) an avalanche on Mount Everest.

air. Volcanoes can create different types of gravity currents depending on the weight of the material ejected. The fumes can form an enormous plume that spreads laterally when reaching their neutral buoyancy, and the pyroclastic flows can hurtle down slopes at hundreds of kilometers an hour, destroying everything in their path.

Another phenomenon closely associated with gravity currents is the buoyant plume. Plumes are characterized by the vertical transport of a buoyant fluid into a denser ambient, driven primarily by buoyancy forces. Typical examples include emissions from chimneys, convective columns from fires, and volcanic eruptions. Gravity currents propagating down inclined boundaries represent intermediate cases between horizontal gravity currents and vertical plumes. Their dynamics exhibit characteristics of one or the other regime, depending on the slope angle.

5 Intrusion of gravity currents

In addition to sloping topography, gravity currents frequently intrude into stratified environments – a characteristic feature of estuaries, lakes, and the open ocean. For instance, dense brine produced by polynyas or discharged from desalination plants descends into a stably stratified ambient, eventually equilibrating with its surroundings.

The vertical extent reached by such currents is a fundamental parameter, as it determines the depth of mass, heat, and salt redistribution. Upon encountering a layer of equal density, the current ceases vertical propagation and transitions into a horizontal intrusion. Figure 9 schematically illustrates a gravity current forming an intrusion. The evolution of these intrusions depends on the balance between

buoyancy forcing, ambient stratification, and entrainment of lighter fluid. In the case of polynya-generated waters, insufficient initial density or excessive mixing with ambient fluid can hinder descent to the ocean floor, limiting their contribution to deep water formation.

Mixing processes play a pivotal role in shaping the final equilibrium depth of the current. A well-known example is the Mediterranean outflow: although initially denser than North Atlantic bottom waters, it entrains sufficient lighter fluid during descent through the Strait of Gibraltar to equilibrate at an intermediate depth ($\sim$ 1 km), rather than reaching the abyss [163].

Accurate representation of gravity currents descending along inclined boundaries in stratified environments is essential for understanding and predicting large-scale ocean circulation, particularly the formation and spreading of Antarctic Bottom Water and the Mediterranean overflow.

Analogous processes also occur in lacustrine systems. For example, cold river inflows into warmer stratified lakes can generate underflows, in which dense inflows plunge beneath the thermocline and propagate along the bottom [90]. These currents may also form in shallow lake regions due to differential surface cooling.

The intrusion depth of such flows has significant ecological implications. It influences the vertical distribution of pathogens [8], the formation of biological hot spots [114], and the depth at which nutrient-rich runoff is deposited—whether within the euphotic zone or in deeper benthic regions [123].

6 Organization of the thesis

This thesis is organized into two main parts that correspond to two part of the process of the cascading of dense shelf waters.

Indeed Figures 20 and 5 illustrate that the cascading of dense waters can be considered in two distinct stages: (i) the densification of shelf waters, and (ii) the subsequent dynamics of the gravity current and its interaction with surrounding water masses.

While the overall mechanism is broadly understood, the specific conditions under which brine rejection leads to Dense Shelf Water formation – and ultimately to Antarctic Bottom Water – remain poorly constrained. Field observations are hindered by the remoteness and harshness of polar environments, and laboratory analogues are rare. In particular, no previous experimental work has directly

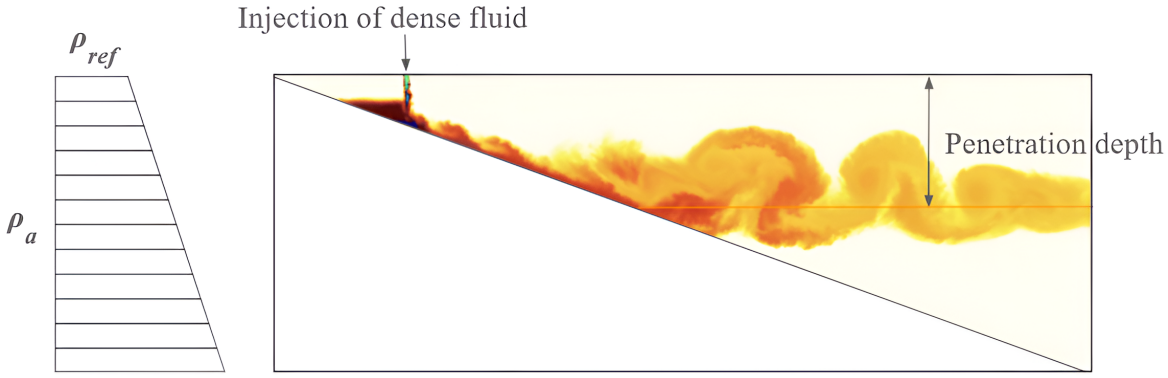

Fig. 9: Schematic representation of a gravity current propagating downslope into a stratified ambient fluid obtained using the author's simulations. The color scale within the gravity current indicates the concentration of a passive tracer, with darker shades corresponding to higher concentrations. The background stratification is not depicted using color for clarity, but is illustrated schematically on the right-hand side.

examined brine rejection as the sole source of buoyancy for initiating a gravity current, despite its central role in polynya dynamics.

To address this gap, a novel experimental apparatus was developed to reproduce the key features of polynya-driven dense water formation and the ensuing gravity current within a controlled laboratory setting. The design, construction, testing, and use of this setup formed the initial phase of the present doctoral research, conducted at the Politecnico di Torino (Italy).

This work investigates two main questions: (i) can brine rejection alone generate a gravity current, and (ii) how do its characteristics depend on the spatial extent of the ice-free area and the underlying topography? To explore these questions, controlled cold-room experiments were performed in which ice was allowed to form over part of a water surface while the resulting flow field was measured using Particle Image Velocimetry (PIV). The findings provide new insights into brine-driven flow dynamics and supply experimental evidence in a domain where observational data remain scarce.

The subsequent dynamics of the gravity current and its interaction with surrounding water masses were more challenging to study in a laboratory setting using brine rejection as the source of buoyancy. Indeed, it would have been difficult to produce a stable stratification in the tank; stratification is a key parameter in controlling the dynamics of the flow, while having to deal with salinity and temperature gradient, both influencing the density of the water. To avoid this problem, we could have done an experiment at room temperature, replacing the brine rejection as a source of buoyancy with an injection of saline water. However, this type of experiment has already been extensively performed and its results are well known (see Sect. 11.6 for more details). Indeed, the cascading of DSW is analogous to a gravity current propagating along a slope into a stratified ambient, and these currents have been extensively studied.

We found that one key open question in the study of the gravity current flowing along a slope into a stratified ambient was the influence of the slope angle on the depth reached by the current. To answer this question, we performed numerical simulations using a Large Eddies Simulation (LES) software. These simulations were performed using the cluster available at Centrale Lyon. They consisted of having a dense current flowing along a slope into a stratified ambient and measuring the depth it reached. By varying the slope angle, we were able to study its influence on the penetration depth.

II Experimental investigation of deep water production in polynyas

Polynyas are regions of open water within the sea ice cover of the polar oceans (see Figure 10). They play a critical role in the global climate system, as they are sites of dense water formation that contribute to large-scale ocean circulation. However, their remote and often inaccessible locations make direct in situ observation and study challenging. For this reason, it would be interesting to try to replicate them in a laboratory to study more easily some of their properties.

In this part, we first provide a review of the existing literature on polynyas, highlighting key findings and unresolved questions. We then describe the experimental setup developed for this study, followed by a presentation of the main results obtained from our laboratory investigations.

7 Literature review on polynyas

7.1 Formation mechanisms

Polynyas are classified into different categories based on their formation. One common classification is: mechanically forced and connectively forced polynyas.

7.1.1 Mechanically forced polynya

A polynya may develop when sea ice is mechanically displaced from the surface by wind or ocean currents, while a geographical barrier inhibits the inflow of new ice into the region. This mechanism gives rise to what is classified as a latent heat polynya.

Wind-driven polynyas

Wind-driven polynyas represent the most common type of polynya. Their formation mechanisms and typical configurations are illustrated in Figure 11. They form on the coast or on the edge of landfast ice or an ice tongue. The wind pushes the ice and allows the water underneath to be in contact with the fresh air. This water then freezes again, creating frazil ice. Frazil ice is a type of ice that forms in turbulent water and is made of an accumulation of ice crystals. The frazil itself is pushed by the wind and accumulates at the edges of the polynya. A balance can be reached between the wind that tends

to increase the width of the polynya and the accumulation of frazil ice that tends to close it. A simple model proposed by Pease [159] illustrates the situation. In this model, the width of the polynya is:

$$W = \frac{VH}{F}(1 - e^{-1F/H}), \tag{1}$$

where W is the polynya width, V is the offshore speed of the solidified ice, F is the rate of production of new ice in the polynya, H is the accumulation depth of the new ice at the downwind side of the polynya, and t is time. The maximum width of the polynya is then VH/F.

The formation and persistence of wind-driven polynyas are strongly modulated by the mechanical properties of sea ice, particularly its resistance to deformation under stress, which is largely determined by ice thickness and age. Multi-year ice, which is significantly thicker and more structurally coherent than recently formed first-year ice, offers greater resistance to wind-induced displacement. In the Antarctic, where multi-year ice is largely absent due to seasonal melting, coastal polynyas frequently emerge under the influence of persistent katabatic winds descending from the interior ice sheet [1]. These winds exert substantial offshore stress, facilitating the removal of newly formed sea ice and the maintenance of open water areas. A notable Arctic analogue is the St. Lawrence Island polynya in the Bering Sea, which forms south of the island during episodes of sustained northerly to easterly winds [159]. In this region, the relative weakness of first-year sea ice and the open exposure to deep water in the southern and western sectors allow efficient ice advection towards the pack ice margin, thereby promoting polynya development.

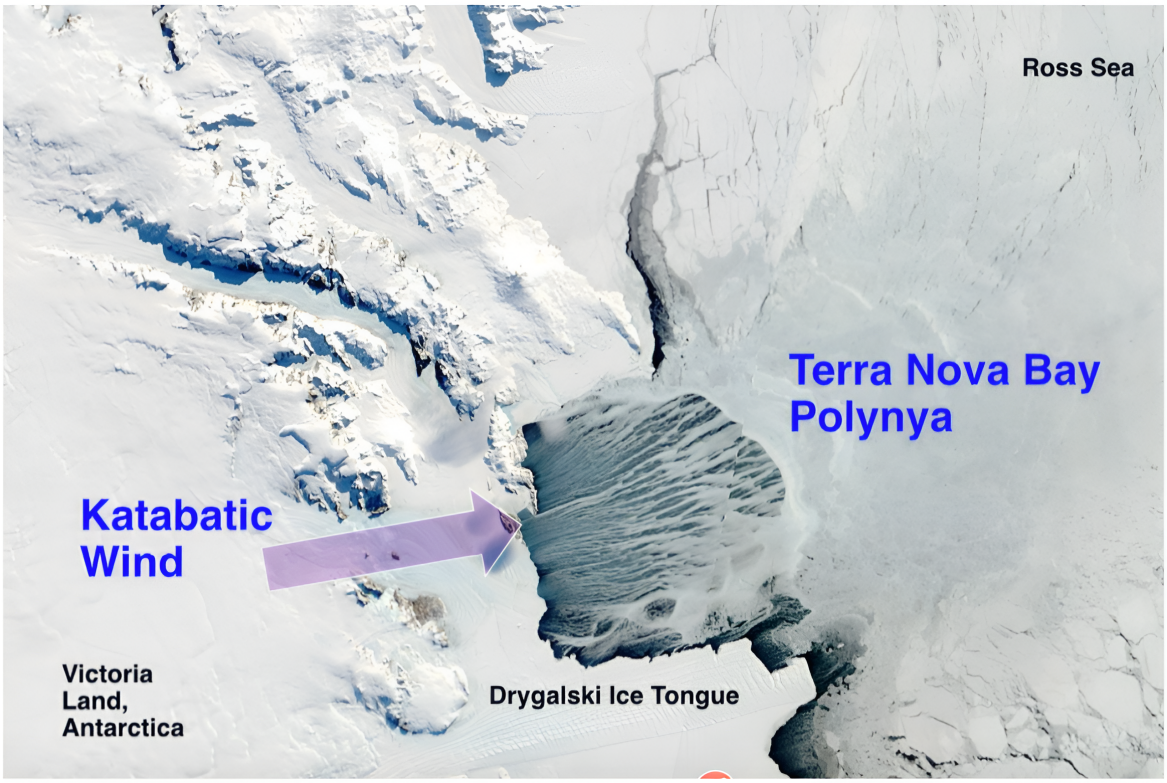

Fig. 10: Satellite image of a coastal polynya (the Terra Nova Bay polynya in Antarctica) with the direction of the strong (katabatic) winds that keep the ice from forming. Image Credit: Lamont-Doherty Earth Observatory.

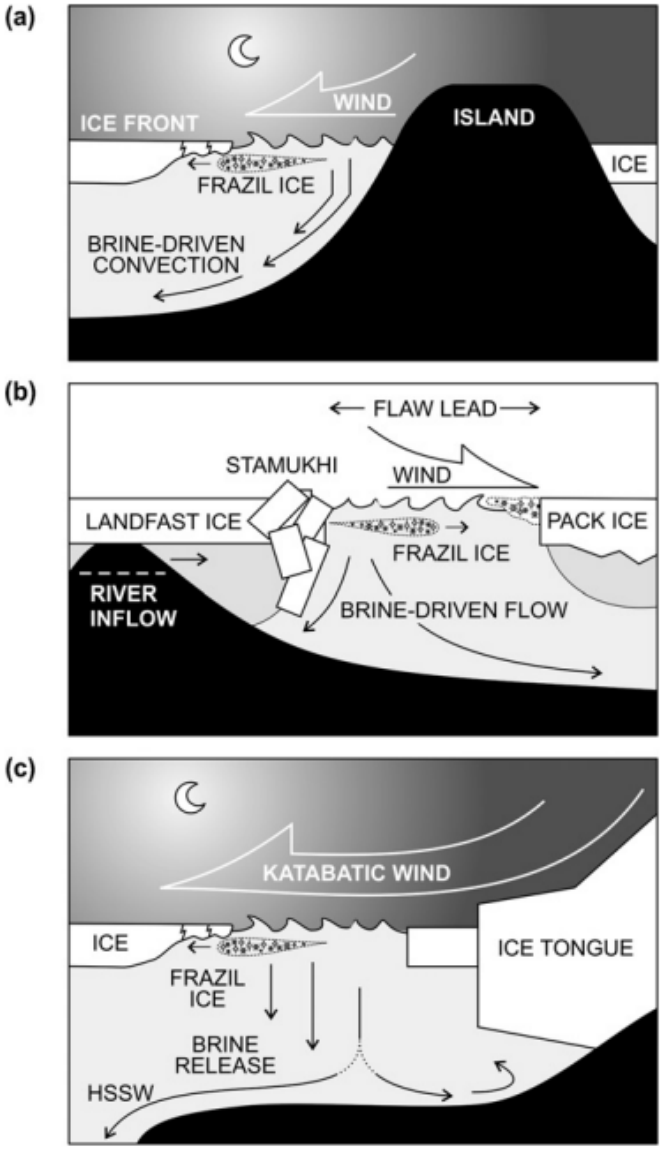

Fig. 11: Physical processes within wind-driven polynyas: (a) a wind-driven polynya forming in the lee of an island (e.g., St. Lawrence Island); (b) the flaw polynya that forms on the Mackenzie Shelf in the southern Beaufort Sea; (c) a flaw polynya in the Antarctic. All diagrams are vertical sections across the polynya. Reproduced from [185].

Current-driven polynyas

Although wind-driven ice divergence is the primary mechanism behind most polynyas, certain systems can also form through divergence induced by ocean currents. However, such current-forced polynyas are relatively rare, since horizontal divergence of oceanic flow is typically weak unless amplified by local bathymetric or coastal features. A well-documented example is the Northeast Water (NEW) polynya, situated off the northeastern coast of Greenland. Its formation is strongly influenced by the regional geography between the Ob Bank to the north and the Norske Øer Bank to the south [32, 178]. In this system, grounded ice floes, or 'floebergs', accumulate over the Ob Bank, acting as a barrier to sea ice advection from the north, while landfast ice over the Norske Øer Bank inhibits southern ice intrusion.

The Northeast Greenland Coastal Current (NGCC) flows northward beneath the landfast ice and enters the polynya region, transporting newly formed frazil ice out of the area and preventing its

consolidation [190]. Although ocean currents provide the principal dynamical control over polynya persistence, NEW exhibits strong seasonal variability and is modulated by additional factors including atmospheric conditions, sea surface temperature anomalies, and large-scale circulation patterns [93].

7.1.2 Convectively forced polynya

Convectively forced polynyas form when sea ice is melted by the upward transfer of heat from warm ocean waters. This heat supply can arise from either free convection, where dense plumes sink and drive vertical mixing, or forced convection, where turbulence generated by shear or large-scale upwelling lifts warmer water toward the surface. Both mechanisms have been observed to sustain polynya formation. Such features are often referred to as sensible heat polynyas. The different convection-driven configurations are illustrated in Figure 12.

Free convection

Free convection in polynya systems typically occurs in regions where cold atmospheric temperatures induce strong surface cooling of relatively warm ocean water. This cooling increases the density of surface waters, causing them to sink and be replaced by warmer waters from below. The continuous vertical overturning maintains surface temperatures close to the freezing point of seawater (approximately −1.8°C), thus inhibiting or delaying ice formation [133, 184].

This process is particularly effective when the mixed layer is deep and weakly stratified, when warm water is present at intermediate depths, such as Circumpolar Deep Water in the Antarctic or

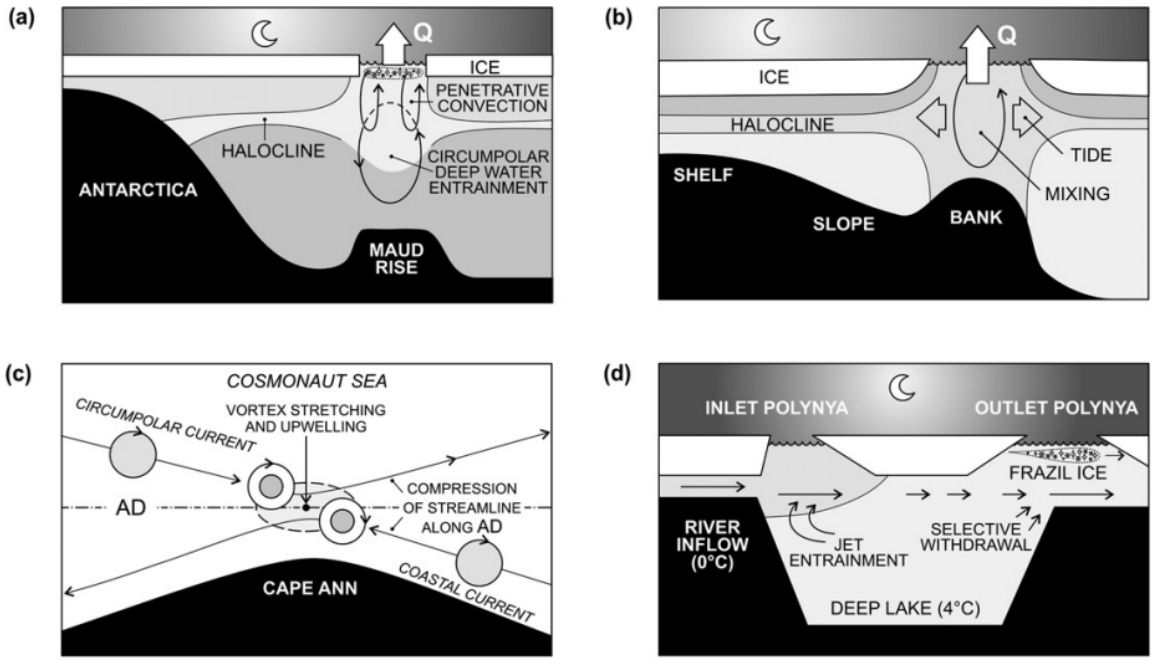

Fig. 12: Diagrams illustrating a variety of physical processes causing convectively forced polynyas: (a) free convection polynya at Maud Rise in the Weddell Sea (Q represents the heat flux to the atmosphere); (b) tidal mixing at Kashevarov Bank in the Okhotsk Sea (adapted from [171]); (c) a polynya maintained by upwelling in the Cosmonaut Sea, Antarctica (adapted from [42]; AD is the Antarctic divergence); and (d) a polynya forced by river throughflow such as Lake Laberge in the Yukon, Canada. Diagrams (a), (b), and (d) are vertical sections across the polynya, and (c) is a view from above. Reproduced from [185].

Atlantic Layer water in the Arctic, and when wind speeds are low, resulting in minimal mechanical ice advection.

A well-known example is the Maud Rise polynya in the Weddell Sea, which has been periodically observed during austral winters (in 1974, 1975, 1976, and 2017). The central mechanism is a weak ocean stratification over the Maud Rise seamount, which shoals warm Circumpolar Deep Water (CDW) and reduces the density gradient between surface and deeper layers. This preconditioned the water column for vertical mixing [78, 93].

Wind forcing and associated surface cooling initiated deep convection by increasing surface water density. As the surface cooled under cold atmospheric conditions, convection penetrated downward, bringing relatively warm subsurface waters to the surface. This heat influx from below inhibits sea ice formation despite continuous heat loss to the atmosphere, thereby maintaining an open-water area [35]. Once deep convection initiates, it reinforces itself via feedback loops: frazil ice formation rejects brine, increasing surface salinity and density, which further enhances convective overturning [56]. However, such convection is episodic, and the polynya typically closes as stratification reestablishes or atmospheric conditions change. Indeed, this polynya has been observed in only a handful of winters in the last 50 years.

Forced convection

Heat can also be brought to the surface by a current and cause the melting of the ice on the surface. There are three main ways this happens: tidal mixing, upwelling, and river throughflows in lakes.

An example of tidal mixing is at Kashevarov Bank in the Okhotsk Sea [171]. The Kashevarov Bank is home to a unique polynya that opens and closes in sync with the fortnightly spring–neap tidal cycle (alternation of strong and more modest tides). The dominant tidal components in this region are the K1 and O1 diurnal tides (some harmonics from the spectrum of tides). Due to the shape and size of the bank, these tidal waves resonate with local wave modes, which amplify the tidal motion and lead to enhanced vertical mixing over the bank.

At the top of the bank, a well-mixed water column develops as a result of this intensified tidal activity. Surrounding this area is a tidal mixing front that separates the mixed region from more stratified waters. Additionally, the interaction between the tidal flow and the bank's topography generates an anticyclonic, or clockwise, circulation around the bank.

The slight difference in frequency between the two main tidal components creates a natural rhythm with a two-week cycle. This resonance causes mixing to be much stronger during spring tides compared to neap tides. As a result, the region experiences alternating periods of strong vertical mixing followed by calmer phases, which leads to repeated cycles of stratification and de-stratification. These physical cycles are believed to influence biological activity in the area, potentially introducing a fortnightly rhythm in biological processes such as nutrient availability and plankton blooms.

Transfer of heat from deep to surface waters can occur as a result of upwelling (current flowing from the depth to the surface of the ocean), either at the coast or in the middle of a gyre. An example of upwelling is the Cosmonaut polynya, which forms in early winter off Cape Ann (50°E) in Enderby Land, Antarctica [42]. At Cape Ann, the interaction between flow and topography generates a vortex that induces the upwelling of warmer waters, thereby creating a polynya.

In some frozen lakes like Lake Laberge in the Yukon, Canada, a river throughflow can create a polynya through its injection of warmer waters. A second polynya, current-driven this time, is created at the outlet of the lake.

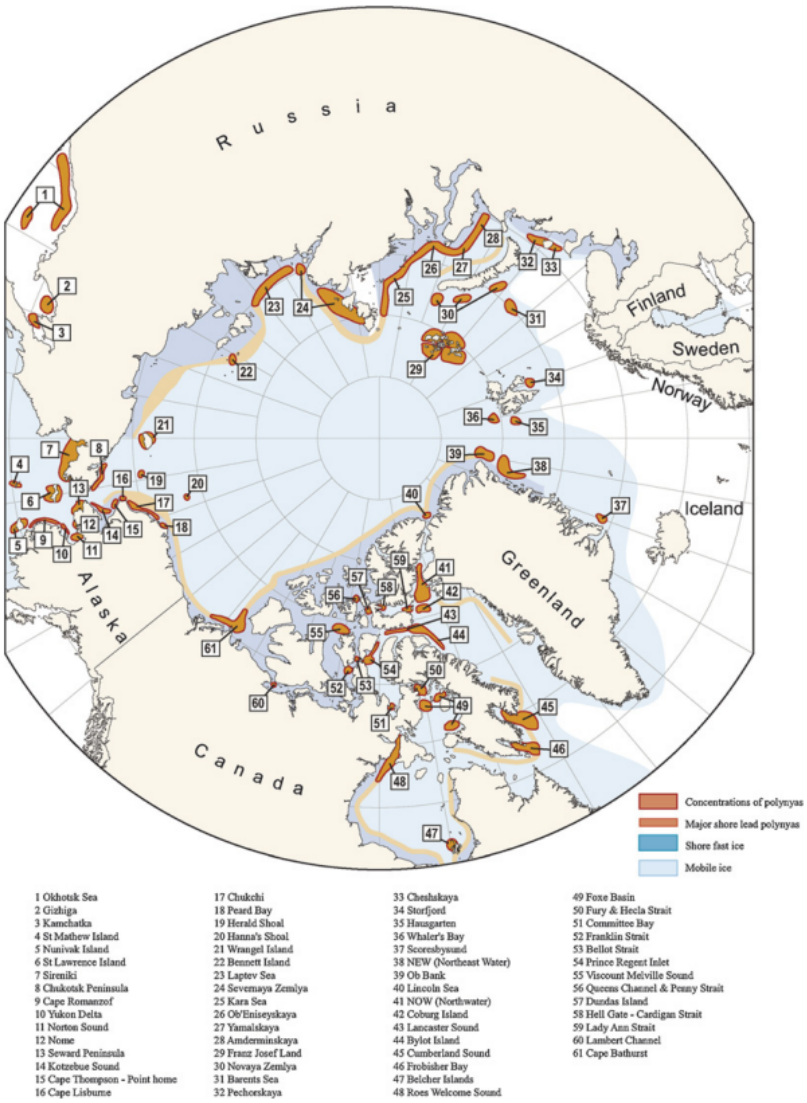

Fig. 13: Distribution map showing the number and names of Northern Hemisphere polynyas detected and identified from (a) an analysis of DMSP SSM/I data using the PSSM method [118] and (b) a literature review. This listing provides a minimum estimate of the number of recurrent polynyas. Some of these polynyas no longer exist in a fashion analogous to their recent history (e.g., the NEW polynya). Reproduced from [185].

7.2 Location

Polynyas are located in the polar regions, both in the Antarctic and Arctic. Despite their superficial similarity, polynyas in the Arctic and Antarctic exhibit significant differences due to contrasting geography, atmospheric dynamics, ocean circulation, and sea ice characteristics.

The Arctic is an ocean basin enclosed by continents, leading to a semi-contained sea ice regime dominated by multi-year ice. In contrast, the Antarctic is a continent surrounded by open ocean, which favors the seasonal melting and regeneration of sea ice [184]. This fundamental difference results in distinct polynya characteristics: Arctic polynyas are generally smaller, longer-lived, and constrained by coastlines and fast ice (ice attached to the shore), whereas Antarctic polynyas are typically larger, shorter-lived, and strongly influenced by katabatic winds and coastal topography [59].

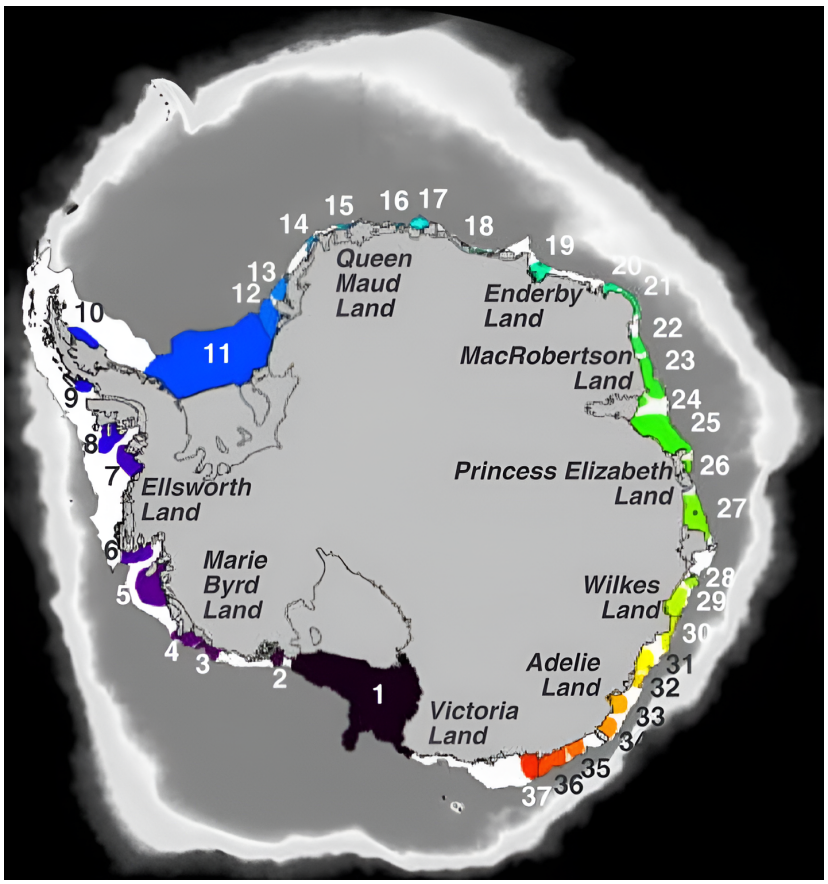

Fig. 14: Map of the Antarctic showing locations of 37 polynyas off the coast of Antarctica. Colors have been assigned to polynyas to individualize them. The numbers refer to the following places: 1. Cape Darnley 2. Davis 3. Prydz Bay 4. Barrier Bay 5. Shackleton Ice Shelf 6. Dibble Iceberg Tongue 7. Mertz Glacier 8. George V Coast 9. Ninnis Glacier 10. Cook Ice Shelf 11. Vincennes Bay 12. Amery 13. West Ice Shelf 14. Shackleton 15. Dibble Ice Shelf 16. Cape Ann 17. Cape Poinsett 18. Cape Colbeck 19. Sulzberger Bay 20. Getz Ice Shelf 21. Dotson Ice Shelf 22. Pine Island Bay 23. Ronne Ice Shelf (western Weddell Sea) 24. Brunt Ice Shelf 25. Riiser-Larsen Ice Shelf 26. Lazarev Sea 27. Cosmonaut Sea 28. Cooperation Sea 29. Davis Sea 30. Mawson Coast 31. Vincennes Bay West 32. Vincennes Bay East 33. Ross Sea 34. Terra Nova Bay 35. Cape Hallett 36. Cape Adare 37. Filchner-Ronne Ice Shelf (eastern Weddell Sea) Adapted from [11].

In the Arctic, polynyas most often arise from persistent offshore winds or ocean currents that drive ice away from the coast or from fixed ice edges. Wind-driven divergence is particularly common, though tidal and current-driven mechanisms also play an important role in narrow straits, as exemplified by the North Water Polynya and the St. Lawrence Island Polynya [178].

In the Antarctic, katabatic winds descending from the interior ice sheet are the primary driver of coastal polynyas. These cold, dense airflows frequently generate expansive open-water regions, such as those observed in the Ross Sea and Terra Nova Bay. Topographic constraints and oceanic heat fluxes further modulate polynya persistence, especially in regions like the Weddell and Amundsen Seas [105]. Figures 13 and 14 highlight the location and names of several major Arctic and Antarctic polynyas. In this study, we concentrate on coastal Antarctic polynyas.

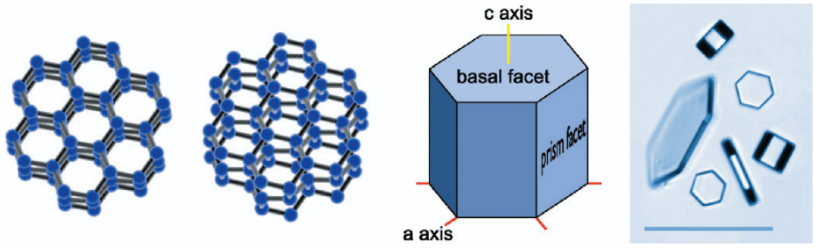

Fig. 15: Left: Two views of the crystal structure of ice Ih, showing a lattice of 'puckered' hexagons. Here, balls represent oxygen atoms and bars represent hydrogen atoms. Middle: A schematic picture of a simple ice prism, defining the principal crystal axes and facet planes. Right: A mosaic image of some typical small ice prisms grown in the lab, showing different aspect ratios. The scale bar is 100 μ m long. Reproduced from [109].

7.3 Formation of sea ice

Pure ice, as found in natural conditions on Earth, almost always crystallizes into the hexagonal crystal form known as ice Ih (9 other forms exist but do not form under natural conditions on Earth) [110]. In this arrangement, the ice crystal adopts a hexagonal arrangement in which each oxygen atom occupies the center of a tetrahedron formed by four neighboring oxygen atoms located at its vertices, with an O–O spacing of about 0.276 nm. These oxygen atoms are clustered near a sequence of parallel layers, called basal planes. The crystal's main symmetry direction, known as the c-axis, is oriented perpendicular to these planes. Overall, the lattice resembles a beehive, built from stacked sheets of slightly distorted hexagons.

During crystal growth, it is energetically more favorable for additional molecules to attach to an existing basal plane rather than initiate a new one. As a result, ice tends to extend more rapidly in the directions of the a- and b-axes, which lie within the basal plane, than along the c-axis.

The open lattice structure of ice means that its density is lower than that of liquid water. At 0°C, the density of pure ice Ih is approximately 917 kg.m^{-3}, compared to 999.8 kg.m^{-3} for pure water at the same temperature. This decrease in density upon freezing (about 9%) explains why ice floats on water – a property of great importance for polar ocean processes.

When water cools to its local freezing temperature, initial ice formation begins with the appearance of small, plate-like crystals in the upper layers. In calm conditions, these crystals nucleate and grow at the surface, merging into a thin, continuous sheet known as nilas. Growth proceeds primarily by direct freezing at the ice–water interface, with minimal mechanical disturbance, producing a smooth and level surface. As the ice thickens, crystal alignment evolves into a columnar structure, with the crystallographic c-axes tending to orient horizontally.

In contrast, under turbulent or wave-affected conditions, nilas formation is inhibited by constant agitation. Instead, the dominant ice type is frazil ice – a suspension of small, typically sub-millimeter to millimeter-sized crystals that may appear as a coarse slush when collected. These crystals often assume disk-like, needle-like, or hexagonal shapes and, unlike surface ice, originate throughout the water column. This occurs because turbulence mixes the upper layers, preventing the establishment of a stable ice cover and promoting uniform cooling.

Frazil ice develops when the water becomes supercooled – cooled below its freezing point without immediate ice formation – while remaining turbulent. In this state, crystals nucleate either spontaneously or via secondary nucleation, in which existing ice particles act as seeds for further growth. The process can generate large quantities of frazil within a short period. The rate of formation and

Fig. 16: Pancake ice on Lake Michigan 2024. Author YJ CHOI.

the physical characteristics of frazil ice are controlled by factors such as the degree of supercooling, turbulence intensity, and salinity; for example, elevated salinity can enhance crystal production but reduce interparticle cohesion.

Frazil ice poses several dangers, particularly to infrastructure and aquatic ecosystems [158]. Its adhesive properties can cause it to cling to submerged structures like water intakes, trash racks, and hydroelectric dams, leading to blockages that reduce water flow and increase the risk of flooding or operational failures. In rivers, frazil ice can contribute to ice jams by accumulating beneath existing ice covers, raising water levels, and potentially causing sudden, destructive floods. Additionally, anchor ice – formed when frazil attaches to the riverbed – can disrupt fish habitats by altering flow patterns and trapping sediment or organisms. In marine environments, frazil ice can hinder shipping and offshore operations by clogging equipment or forming dense slush layers that impede vessel movement. Its rapid and unpredictable formation makes it a significant hazard in cold-region hydrology and engineering.

As concentrations of frazil increase, crystals begin to stick together, forming mats of grease ice, a soupy, opaque layer that dampens wave motion. Continued agitation causes the grease ice to organize into distinct, roughly circular pancake ice floes. Pancakes are typically 0.3–3 m in diameter and 50-70 cm in thickness, with raised edges caused by repeated collisions and rafting in the wave field. Over time, pancake floes can freeze together into a continuous sheet known as consolidated pancake ice as conditions calm, providing a pathway from turbulent frazil formation to stable sea ice cover.

Consolidated pancake ice exhibits a bottom morphology distinct from that of typical sea ice. At the moment of consolidation, the individual pancakes are irregularly packed and often rafted over one another, with frazil ice filling the gaps and bonding the floes together. This process produces an underside that is rough and uneven, with rafted layers locally doubling or even tripling the average ice thickness. On the upper surface, the rims of the original pancakes may remain visible, creating a rugged “stony field” appearance.

7.4 Brine rejection

When sea ice forms from seawater, the phase change presents a clearly distinct behavior from its freshwater counterpart. Indeed, unlike freshwater, seawater contains dissolved salts – primarily sodium chloride – which are not easily incorporated into the ice crystal lattice. The formation of ice leads to the exclusion of the salt, a process known as brine rejection [202, 210].

This exclusion occurs because the hexagonal crystalline structure of pure ice cannot accommodate the ions present in seawater. As a result, the forming ice is composed of relatively fresh water, while the surrounding unfrozen water becomes increasingly saline [107]. During the early stages of ice growth, some brine remains trapped in narrow, quasi-liquid channels and pockets within the ice matrix, creating what is referred to as mushy layer structure [213].

As the sea ice thickens and cools from the top (due to heat loss to the atmosphere), the internal temperature of the ice drops. This promotes further freezing of the residual brine in the channels, which in turn increases its salinity and density. When this denser brine exceeds a threshold density compared to the underlying seawater, it drains downward via gravity through brine channels, contributing to the formation of a denser water mass below the ice [126].

These processes of brine drainage explain why multi-year ice is less salty than younger ice [46]. Young ice typically presents a salinity of 10 PSU, one-year ice has a salinity of 3-4 PSU, and multi-year ice 1-3 PSU. PSU is the unit used to measure salinity, which means Practical Salinity Unit. A water at one PSU has one gram of salt diluted per liter. As a reference, oceanic water typically has a salinity of about 34-35 PSU.

The brine rejection has a deep impact on the water masses. The polynyas forming off the coasts of Antarctica due to a strong forcing of katabatic wind are sometimes called 'ice factories' because of their substantial production of frazil ice [44]. Although they represent only about 1% of the total sea ice extent, they account for up to 10% of the total sea ice volume production in the Southern Ocean [194]. This large production of ice (mostly frazil ice) also produces a large quantity of brine rejection. This leads to a concentration of salt in the waters of the polynyas. Saltier waters are also heavier. The state equation of seawater that governs the dependence of the density of water on the salinity, temperature, and pressure is a very complex, non-linear equation. A simple linear approximation is enough to give a taste of how the density varies with the different variables, but it is not enough for quantitative oceanography. Around a reference density ρ_0 small variations of density follow this linearized equation:

$$\rho(S,T,P) = \rho_0(1 - \beta_T(T - T_0) + \beta_S(S - S_0) + \beta_P(P - P_0)), \tag{2}$$

where $\beta_T = 2(\pm 1.5).10^{-4}$ T^{-1}, $\beta_S = 0.76(\pm 0.2).10^{-3}$ S^{-1},and $\beta_P = 4.4(\pm 0.2).10^{-10}$ Pa^{-1} [205].

We can see from this equation that the increase in temperature decreases the density, and that an increase in salinity increases the density; an increase in pressure also increases the density. Thus, the increase in salinity under coastal polynyas locally increases the density of the water.

From this equation, we can also see an interesting effect of the salinity: the disappearance of the maximum density. In fresh water, the point of maximum density for a given pressure is obtained for a temperature of 4°C. If the temperature goes lower than 4°C, the density of the water diminishes. This behavior disappears with the addition of salt. Salty water does not present a maximum of density, but the evolution of the density is monotonous with respect to the temperature. Another effect of salinity

is its influence on the freezing point of water. The saltier the water, the colder it needs to be to freeze. For a salinity of 34 PSU, the freezing point is around -1.8°C.

7.5 Shelf water

Continental shelves are the submerged, gently sloping extensions of the continents, typically stretching from the shoreline to depths of about 200 m before dropping off at the continental slope [61]. They are among the most productive marine regions due to nutrient mixing and sunlight penetration. Some of the most famous shelves include the Arctic Siberian Shelf, the world's largest, spanning over 2.7 million km^2 with shallow, ice-covered waters; the North Sea Shelf, known for rich fisheries and oil and gas reserves; the Great Barrier Reef Shelf off Australia, hosting the world's largest coral reef system; and the Amazon Shelf, shaped by massive sediment discharge from the Amazon River. These shelves are crucial for marine biodiversity, energy resources, and global ocean circulation.

The continental shelves around Antarctica are unusually deep and wide compared to those of other continents, often extending to depths of 400–800 m instead of the global average of $\sim$ 200 m [7]. They are largely covered by floating ice shelves that are extensions of the ice shelf covering the continent. Occasionally, some large chunk of ice detaches from the ice shelf and floats off the coast. They are known as icebergs. If an iceberg melts above the continental shelf, it can considerably freshen the shelf water as icebergs are made of fresh water.

Basal melting of ice shelves occurs when relatively warm ocean water flows beneath the floating ice, transferring heat across the ice–ocean boundary [166]. This process thins the ice shelves from below and can accelerate ice-sheet discharge into the ocean. Basal melting is highly variable, being most intense near grounding lines and beneath deep ice cavities, and it plays a critical role in regulating Antarctic mass balance and global sea-level rise. Contrarily, if cold water lies beneath a floating ice shelf, it can cool down even more due to the colder temperature of the ice and become supercooled. Both of these phenomena directly impact the density of the shelf water: basal melting freshens the water, making it lighter, and the supercooling cools it, making it heavier.

The main driver of shelf water density in Antarctica is the presence of coastal polynyas. Opened by strong katabatic winds, these regions produce large amounts of frazil ice. Through brine rejection, enormous quantities of salt are released into the ocean, increasing water salinity and density. This process generates Dense Shelf Water (DSW), which, if sufficiently dense, can cascade down the continental slope to the abyss, where it contributes to the formation of Antarctic Bottom Water (AABW) (Figure 17).

However, not all Antarctic shelves produce DSW. Shelf waters are generally classified into three regimes: fresh shelf water, dense shelf water, and warm shelf water [200]. Their distribution and interaction with surrounding waters are illustrated in Figure 18, and the spatial location of these regimes along the Antarctic coast is shown in Figure 19.

The fresh shelf regime dominates large parts of East Antarctica and the Amundsen–Ross Sea sector. Here, persistent easterly winds drive onshore Ekman transport, leading to a sea surface height anomaly and a westward Antarctic Slope Current (ASC). Cold shelf waters, limited cross-slope exchange, and surface convergence-induced downwelling combine to establish a strong front that separates fresh, cold shelf waters from warm, salty Circumpolar Deep Water (CDW). In this regime, density surfaces align closely with isotherms, reducing along-isopycnal gradients in temperature and salinity, while strong lateral density gradients form near the shelf break. These fronts often tilt downward and poleward toward the continental slope, in some cases intersecting it, which effectively blocks CDW

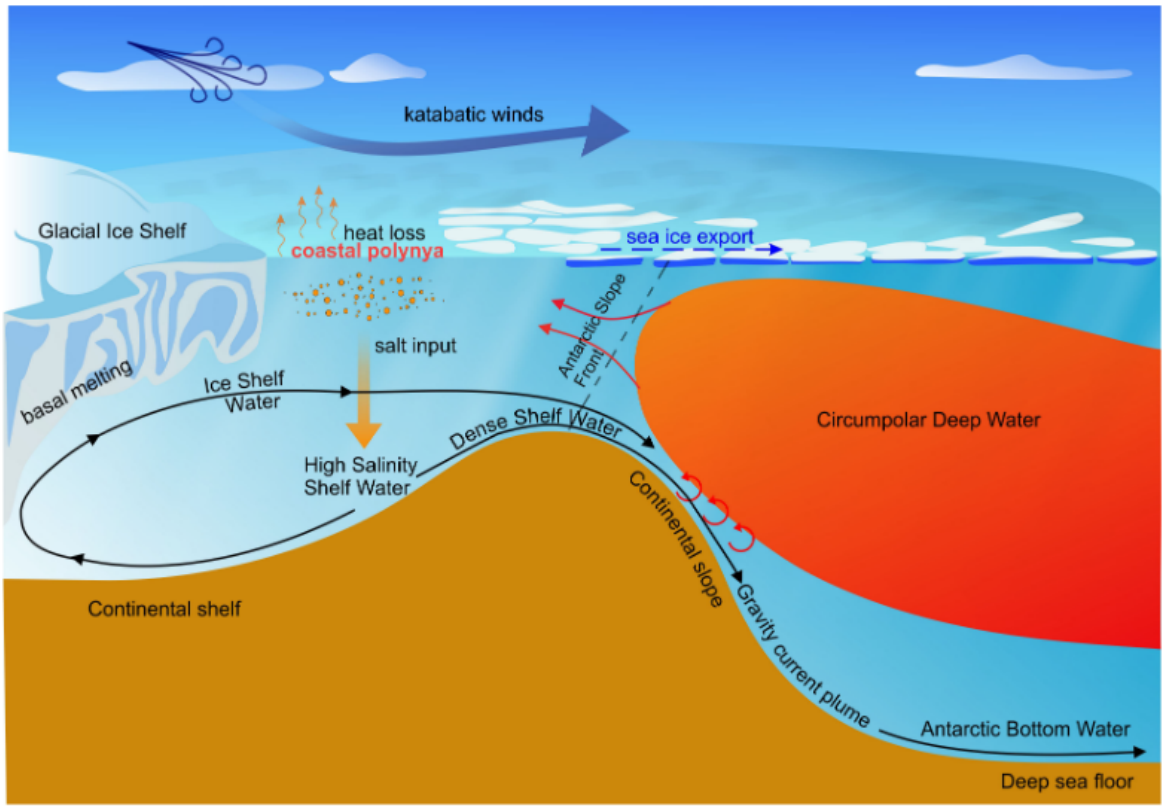

Fig. 17: Schematic diagram summarizing Antarctic Bottom Water (AABW) formation. AABW originates on the Antarctic continental shelf, where intense surface cooling and salt input occur during sea ice formation. Enhanced sea ice formation in coastal polynyas allows High-Salinity Shelf Water (HSSW) formation. In some regions, HSSW interacts with the ice shelf base to produce supercooled (below the surface freezing point) Ice Shelf Water (ISW). These cold shelf waters are often referred to as Dense Shelf Water (DSW), as they are dense enough to descend down the continental slope as a gravity plume. Entrainment with Southern Ocean waters during their descent produces AABW. Reproduced from [182].

from intruding onto the shelf. The resulting sea surface height gradients intensify the near-surface westward ASC. At depth, however, vertical shear weakens this current, and in some locations an eastward undercurrent forms, transporting glacial meltwater across the Antarctic Slope Front.

The warm shelf regime occurs where CDW intrudes directly onto the shelf, raising water temperatures by 2–3°C relative to other shelf waters (sometimes above 0°C). This situation is common in regions such as the Amundsen Sea Low and Bellingshausen Sea Low, where weak easterlies and limited polynya activity fail to block CDW inflow. As a result, warm water penetrates the shelf, enhancing basal melting of floating ice shelves and reducing their extent.

The dense shelf regime forms through brine rejection in polynyas and/or supercooling beneath ice shelves. These processes create shelf waters that are sufficiently dense to cascade down the continental slope, where they ventilate the abyss and form AABW (see Figure 17).

7.6 Water masses transformation

The AABW and DSW are not the only water masses of the Southern Ocean. The Southern Ocean is composed of several distinct water masses, each characterized by specific physical and chemical properties such as temperature, salinity, and density.

One of the primary surface layers is the Antarctic Surface Water (AASW), formed through direct interaction between the ocean, atmosphere, and sea ice [153]. AASW is typically cold and relatively fresh due to heat loss to the atmosphere and freshwater input from precipitation and seasonal ice melt. During the austral winter, strong katabatic winds and enhanced sea ice formation further intensify surface cooling. In contrast, during summer, ice melt increases the freshwater content, lowering the surface salinity. AASW serves as the precursor for both Antarctic Intermediate Water (AAIW) and Antarctic Bottom Water (AABW), and it plays a central role in modulating air-sea exchanges and the extent of seasonal sea ice.

Antarctic Intermediate Water (AAIW) forms to the north of the Antarctic Circumpolar Current (ACC), where subduction of surface waters occurs at intermediate depths (approximately 700–1200 meters) [162]. AAIW is characterized by relatively low salinity and high oxygen content, resulting from

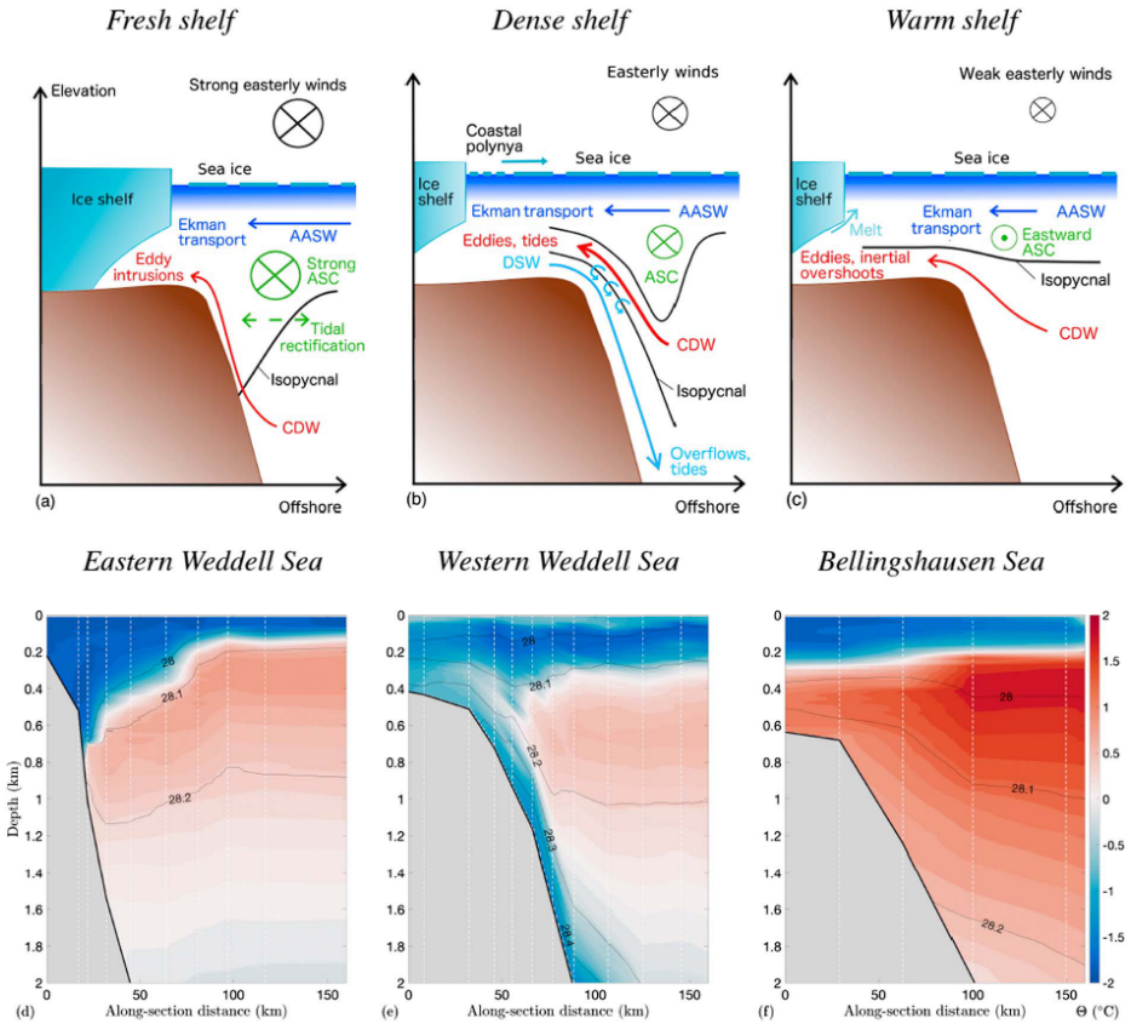

Fig. 18: (a–c) Key water masses, along- and across-slope flows and supporting mechanisms in the (a) Fresh shelf, (b) Dense shelf, and (c) Warm shelf Antarctic Slope Current (ASC) regimes defined in this article. (d–f) Measurements of conservative temperature (colors) and neutral density (black contours) across the ASC in locations corresponding to each ASC regime: (d) the eastern Weddell Sea [92], (e) the western Weddell Sea [199], and (f) the Bellingshausen Sea [217]. Section locations are shown in Figure 19, and white dashed lines indicate locations at which hydrographic casts were taken. The following water masses are identified: Antarctic Surface Water (AASW), Circumpolar Deep Water (CDW), Dense Shelf Water (DSW). Reproduced from [200].

the mixing of AASW with warmer, saltier subtropical waters. Once formed, AAIW spreads northward into the subtropical gyres of the Atlantic, Indian, and Pacific Oceans, where it ventilates the upper ocean layers and participates in the meridional redistribution of heat and gases.

In the abyssal layers, the Antarctic Bottom Water represents the densest water mass in the global ocean [182]. It is primarily generated in coastal polynyas via the cascading of DSW along the continental slope. This allows for the transport of oxygen and nutrients to the depths of the ocean. Thus, nourishing the life forms of the abyss.

The entire vertical exchange is driven by the upwelling of Circumpolar Deep Water (CDW), a relatively warm and saline water mass found at mid-depths [198]. CDW upwells south of the ACC as a

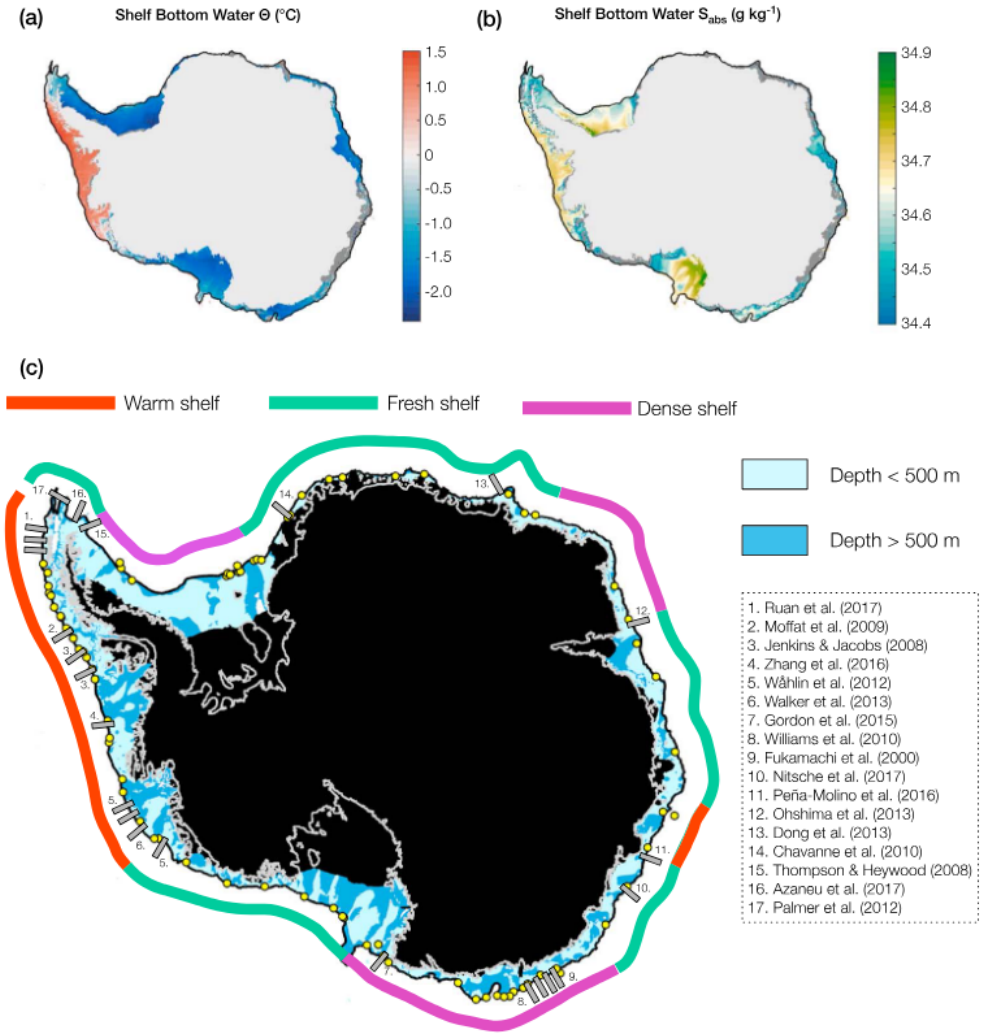

Fig. 19: Classification of the Antarctic Slope Current system around Antarctica. (a) Conservative temperature and (b) absolute salinity of Antarctic Shelf Bottom Water (ASBW). (c) The colored bar shows the spatial distribution of the three types of shelves: Warm shelf, Fresh shelf, and Dense shelf. The shelf break is indicated by the black contour marking the 1,000 m isobath. The shading shows the bathymetry of the continental shelf. Yellow circles show the position of historical hydrographic measurements used to determine the presence of Dense Shelf Water from [15] and [6]. Gray bars indicate the positions of recent hydrographic sections that were used in determining the classification of the shelves. References to descriptions of the hydrographic sections are provided in the dotted box. Reproduced from [200].

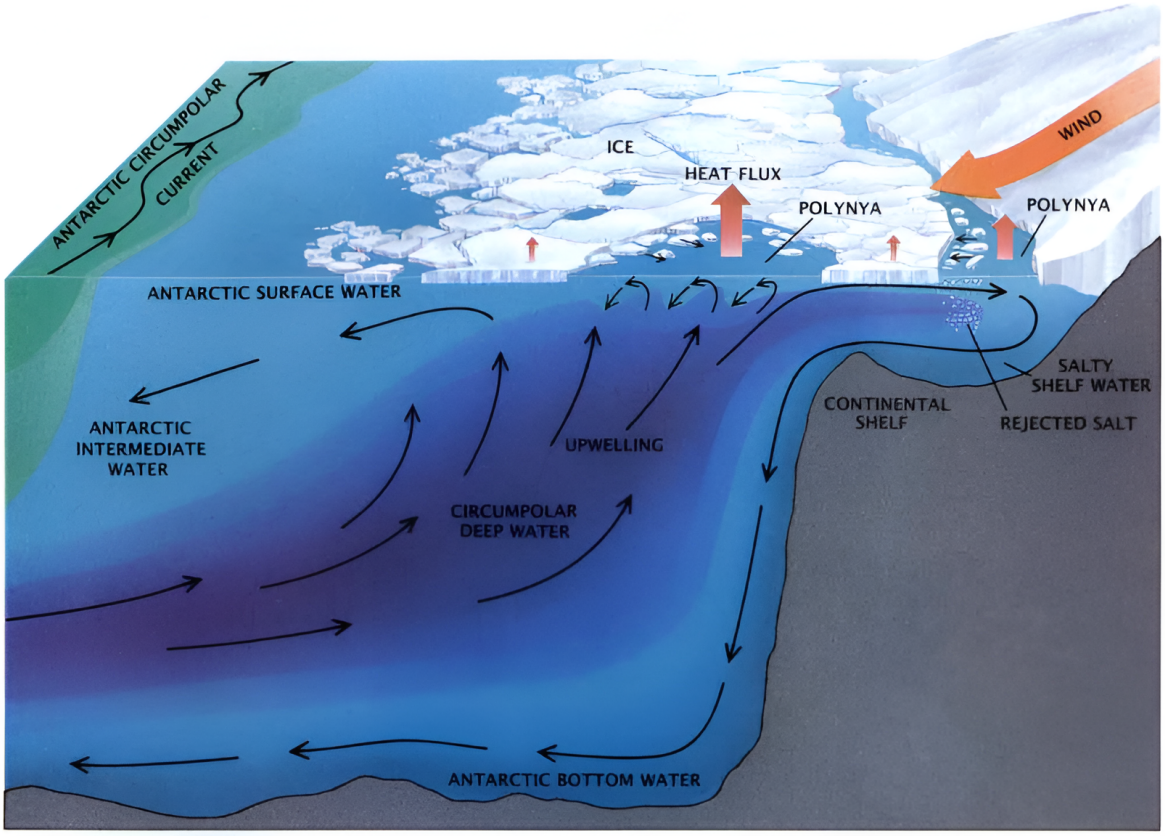

Fig. 20: Schematic of the formation of the meridional circulation pattern of the southern ocean. Reproduced from [79].

result of wind-driven Ekman divergence and is brought to the surface, where it undergoes transformation into AASW. This transformation involves both heat loss to the atmosphere and the gain of freshwater from precipitation and melting ice, reducing its density.

The fate of this modified surface water follows two principal pathways. A fraction is transported northward, where it gradually subducts to form Antarctic Intermediate Water (AAIW). The remainder is advected southward, where it undergoes further cooling and densification within coastal polynyas before sinking to form Antarctic Bottom Water (AABW) [69]. This large-scale exchange constitutes the meridional overturning circulation of the Southern Ocean, illustrated in Figure 20. It represents a key branch of the global thermohaline circulation, introduced in Sect. 3.

7.7 Open questions

From this literature review, we have seen that polynyas are areas of crucial importance to the climatic system. The main mechanism by which they impact the overall climate is the formation of AABW by the cascading of DSW along the continental slope.

Despite the importance of AABW, the specific conditions leading to its formation are still not fully understood. It is clear that there is a need for a significant increase in the density of surface water so that it can flow down the continental slope. The density of AABW is very high with respect to surface water because it is colder and more saline. It is generally hypothesized that the continental shelf beneath polynyas facilitates the accumulation of density coming from the brine rejection by reducing the mixing with the surrounding water and allowing shelf waters to get dense enough to flow

down the slope and form AABW. However, the necessary size of the plateau for such accumulation is not well-defined [6]. Indeed, some polynyas do not produce DSW, and some polynyas induce AABW formation even without a large continental shelf (for example, the Cape Darnley polynya) [145]. The factors affecting the production of brine rejection in polynyas and their temporal evolution are not fully understood, especially the impact of seasonal and meteorological forcing [182].

Furthermore, the dynamics of DSW cascading down the continental slope are poorly described due to the challenges associated with obtaining underwater measurements in these remote regions. Submarine canyons along the slope have been suggested to play a role in directing these flows [4]. However, many small-scale and local processes affecting DSW formation and its downslope flow remain poorly understood. These include tidal influences on the continental shelf, the influence of the topography of the bottom, the entrainment of seawater, the mixing of the DSW with other water masses, turbulence-induced processes, the role of shelf meltwater, and the interaction of the brine plume with water stratification [182]. This lack of understanding leads to uncertainties in the numerical models used for climate simulations [125].

Given the challenges inherent in conducting field measurements about DSW and AABW, one might expect experimental studies to be prevalent. Such studies offer the advantage of controlled environments, allowing for precise measurements of different variables. However, experimental studies in this area remain scarce. The closest attempt at replicating a polynya in the laboratory was conducted by Ushio and Wakatsuchi in 1993 [204], where an air flow was applied over a water tank in a cold room to simulate polynya conditions. Figure 21 shows the setup used in this experiment. A key limitation encountered in the experiments was that the polynya consistently closed over time, as ice accumulated at the end of the tank and gradually extended across its surface. The limited number of laboratory studies is likely due to the substantial challenges inherent in reproducing such complex phenomena within controlled settings.

The cascading of DSW down the continental slope is analogous to gravity currents [80], namely, flows driven by buoyancy differences. A complete presentation of gravity currents can be found in Sect. 11 of the present thesis. In the context of AABW formation, the increase in density arises from higher salinity and lower temperatures. Gravity currents have been extensively studied; in particular, many experimental studies have been carried out with an influx of saline water as a source of buoyancy [26, 139, 215]. Sinking gravity currents along slopes, with or without stratification, are a common focus of these studies [138]. Various sources of buoyancy for gravity currents and plumes have been studied. Mainly, heat flux, influx of saline water, or gases heavier than air (CO_2, for example) were considered as triggers of density gradients [144].

The generation of buoyancy in the case of a polynya, other than the sea-surface cooling due to exchanges with the colder atmosphere, is the brine rejection. The phase change at play in this mechanism is peculiar and different from the simple addition of saline water or the heating of a surface without phase change. Even though several authors noted the clear similarities between DSW flowing down the continental slope and gravity currents, no published article presented experiments using brine rejection as a source of buoyancy to induce a gravity current. These authors worked mainly with numerical simulations or experiments involving the addition of saline water [15, 101].

Although not investigated as a buoyancy source, many aspects of brine rejection have been studied, both with laboratory experiments [141] and numerical simulations [137]. The study that proposed experiments closest to using brine rejection as triggers of density gradients was [68]. In this article,

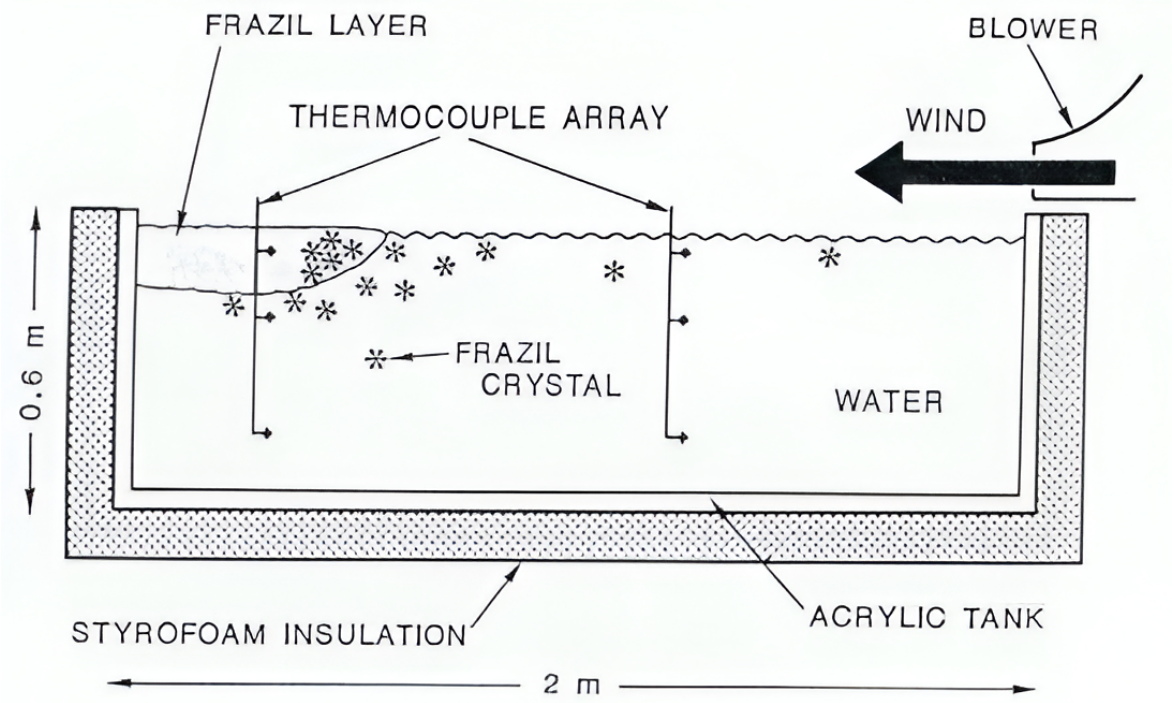

Fig. 21: Experimental setup used by Ushio and Wakatsuchi to create a polynya in the laboratory. Reproduced from [204].

the convection induced by brine rejection in a tank of water was studied; the brine rejection was homogeneous at the surface of the water and not confined in a polynya.

In this general picture, two key open questions are addressed in this study: is brine rejection alone capable of generating a gravity current? If so, how does the latter depend on the system geometry (i.e., spatial extent of brine rejection and topography of the bottom)?

This study aims to shed light on the above questions by conducting a preliminary laboratory study, in which polynya-like conditions are reproduced. The focus is on the effects of brine rejection on the velocity field within a water tank. The experiments were conducted in a cold room where ice was allowed to form on part of the water surface, creating conditions similar to a polynya. To assess the influence of brine rejection, the experiments were performed using both saline and freshwater, and the velocity field was measured using Particle Image Velocimetry (PIV).

This preliminary study aims to provide novel laboratory data on polynyas, filling a gap where previous analog studies are lacking.

An article named 'Laboratory experiments on Dense Shelf Water formation' was published by the author of this thesis on the 25th of April 2025 in the Journal of Environmental Fluid Mechanics [34]. This article presents the experiments that were done to answer the scientific question presented above. The next two sections are a modified version of the text of this article.

8 Experimental setup and methodology

8.1 Setup

The experiments were carried out in the Water Engineering Laboratory of the Department of Environment, Land and Infrastructure Engineering (DIATI) of the Politecnico di Torino in Italy. The

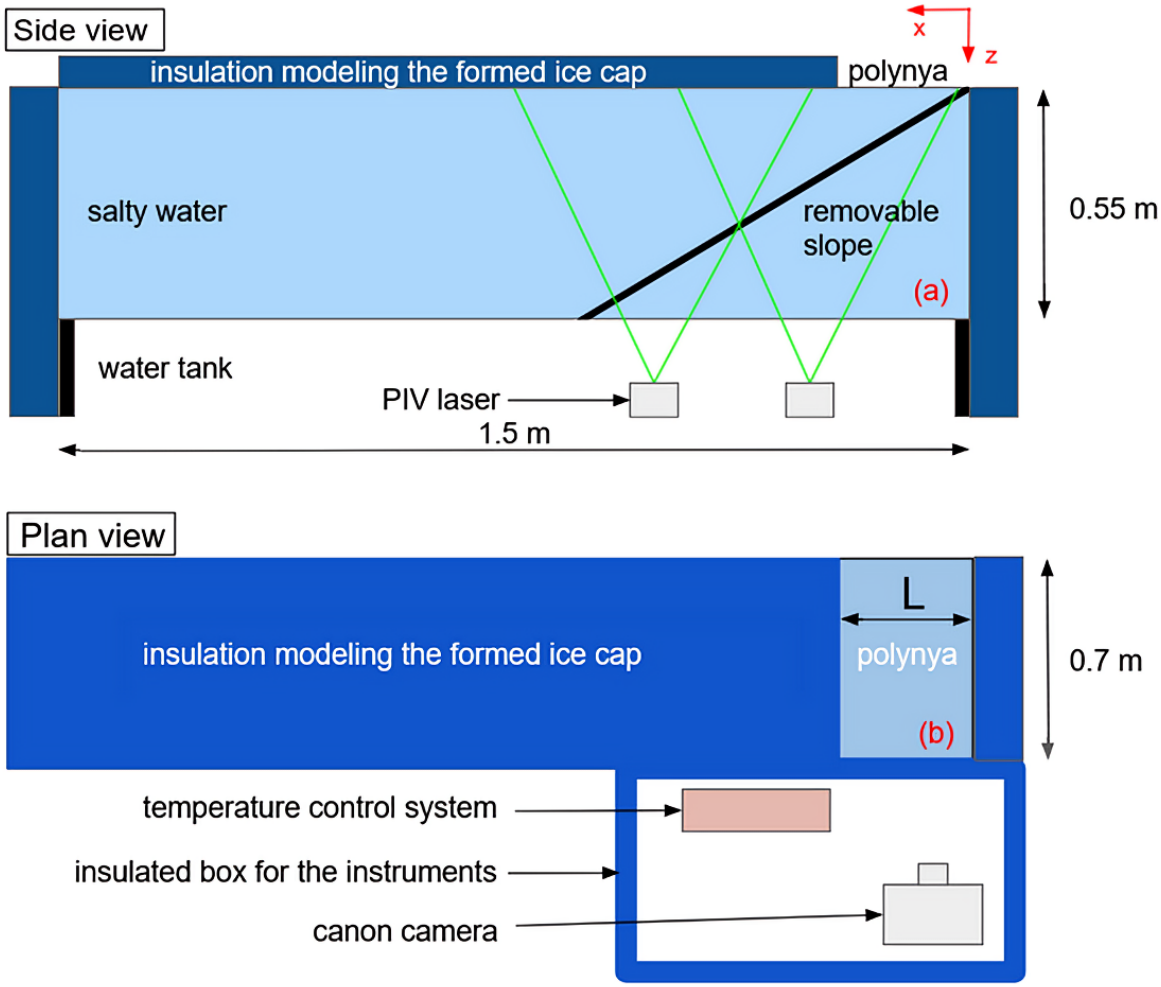

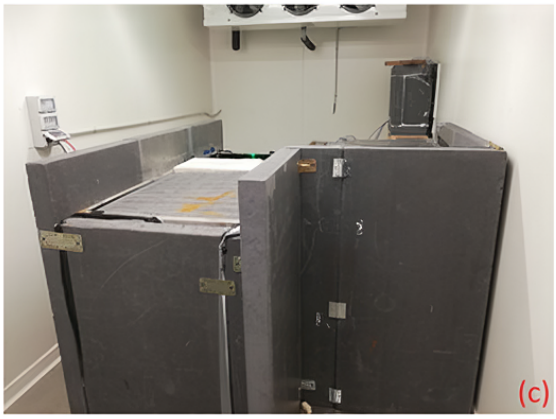

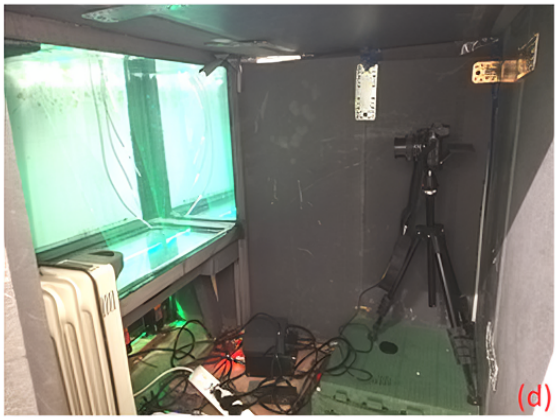

Fig. 22: Schematics **(a,b)** and pictures **(c,d)** of the experimental setup: **(a)** side view, **(b)** top view, **(c)** experimental setup in the cold room, **(d)** inside of the insulated box with the PIV system.

schematics and pictures of the experimental setup are shown in Fig. 22. It consists of a tank made of stainless steel for the structure and glass for the walls, sizes of 1.5 m × 0.70 m × 0.55 m, filled with fresh or salt water (Fig. 22a-b). The axis system is $\{x,z\}$, with x being the horizontal axis and z the vertical (see Fig. 22a). The point (0,0) is located in the upper-right angle of the water body, and both axes are directed toward the tank (the x-axis is directed toward the left and the z-axis is directed toward the bottom). The tank was placed inside a cold room maintained in a temperature range of -5°C to -20°C, with a precision of ±1°C. The temperature within the cold room is homogenized by fans, ensuring a consistent thermal distribution around the target temperature. The system operates by allowing the temperature to decrease by one degree below the target before deactivating the cooling mechanism. Once the temperature increases to one degree above the target, the cooling system is reactivated, thereby maintaining the desired thermal conditions. To insulate the tank from external temperature, the walls were surrounded by a 20 cm thick layer of polystyrene. Two geometries were considered, one with a vertical wall and one with a 45° inclined wall starting at the free surface. To simulate a polynya, most of the free surface was covered with a 20 cm thick layer of polystyrene, mimicking the insulation provided by a thick ice pack. An area of open water was preserved at one end of the tank. Its width was equal to the tank width, and three different lengths, L, (see Fig. 22b) were used during the experiments: 25 cm, 35 cm, 45 cm. Two different kinds of experiments were carried out: an experiment that aimed at measuring the velocity field inside the tank and an experiment that aimed at measuring the salt flux generated by the brine rejection.

An insulated box was constructed within the cold room to house the instrumentation (Fig. 22c-d). This insulated box was maintained at a temperature of approximately -1°C using a heating system. This setup ensured that the glass wall inside the box maintained no flux conditions, with the water temperature during the experiments being around -1.2°C.

Velocity measurements were obtained using the particle image velocimetry (PIV) technique. A laser plane was created in the x-z plane by two lasers MDL-III 520 nm, 300 mW, 30° angle from CNI Laser positioned beneath the tank. A Nikon Z5 camera, housed inside the insulated box, recorded the water movements at 24 frames per second. The PIV method used was a simplified version. Due to the slow movement of the water in these experiments (of the order of magnitude of the millimeter per second), a constant laser sheet was sufficient, and the natural impurities in the water served as tracers. The recorded videos were processed using the PIVlab software from Matlab to determine the velocity fields [197]. One image out of every two from the video was used, resulting in a relative acquisition sampling frequency of 12 Hz. Interrogation windows were chosen to be 128 × 128 pixels^2 with an overlap of 50 %. This allowed us to obtain one vector for every centimeter. The measurement area was 33 cm x 59 cm and was situated 13 cm deeper than the free surface and 5 cm above the bottom.

Salinity measurements were obtained using an OAKTON 35419-35 CON 550 Series Benchtop Conductivity Meter Kit. This instrument allows for a precision of 0.1 g/L. The salinity measurements were used for the setup of the experiments, as well as to measure the salt flux released by the brine rejection.

Furthermore, four PT100 temperature measurement probes, with a precision of ±0.2°C, were immersed in water along the wall at four different depths (respectively 5 cm, 19.5 cm, 34 cm, and 38.5 cm below the surface of the water). The probes were connected to a Data Acquisition System (DAQ) from National Instruments to monitor the temperature of the water. A calibration of five points (-5° C, -2° C, 0° C, 2° C, 5° C) was performed before taking the measurements. The temperature measurement allowed us to control the experimental conditions with regard to the water temperature.

The temperature of the water in the tank was -1.2°C for the salinity 34 PSU and -2.6°C for the salinity 70 PSU with a precision of 10% (notice that these temperatures are close to the corresponding freezing point of the salty water). The water was stirred to ensure homogeneity of the temperature.

8.2 Runs

The experiments aimed to investigate the effect of brine rejection in polynya-like conditions. To do this, the velocity field in the tank and the salt flux released by the brine rejection were measured.

The experimental procedure was as follows:

1. the cold room temperature was adjusted to the desired setting, which typically requires a few hours to stabilize;
2. the water was cooled to its freezing point as a result of thermal exchanges with the cold air. Usually, it takes twelve hours, depending on the initial temperature of the water, so it was initiated the day before the experiment;
3. when the temperature of the water was close to its freezing point (which depends on the salinity [27]) the water was stirred with a stick to ensure homogeneity;
4. the water was allowed to settle for five minutes to wait for the dissipation of the movements in the water and the formation of the ice;
5. when the ice started forming at the surface of the polynya, the PIV measurement was set for 30 minutes;
6. 30 minutes after the ice started to form on the polynya surface, the PIV measurement was stopped, and then the ice was retrieved with a net;
7. the retrieved ice was melted, and its salinity and volume were measured. The salinity in the melted ice and in the salt water were compared, and the salt flux was computed according to the relation $(S_{water} - S_{ice}) \cdot V_{ice}/(A \cdot T)$, where S_{water} is the salinity of the water, S_{ice} and V_{ice} are the salinity and the volume of the melted ice, respectively, A is the area of the open free-surface and T is the duration of the experiment.

This experimental procedure was chosen after trying various methods to keep a polynya open. The original aim was to use an air flow to open and sustain the artificial polynya. This procedure, described by Ushio and Wakatsuchi [204], involved using airflow over the aquarium in the cold room to create and maintain a polynya. The study demonstrated that the polynya gradually closes over time. The same procedure was applied here: a fan and a convergent nozzle were used to induce an air flow at the water surface. This enabled the polynya to remain open for a brief period. However, the air flow induced excessive movement in the water, generating surface waves and internal fluid cells, due to wind shear stresses. This interference masked the actual effect of brine rejection while being insufficient to maintain an open polynya for an extended period. Therefore, a simpler procedure was adopted. The absence of wind introduces a difference in the type of ice formed compared to that in a natural polynya. In polynyas, frazil ice is typically produced, whereas without wind, a more coherent, mushy layer of consolidated ice forms. Both differ from the solid slab of ice commonly observed in freshwater. Brine rejection occurs in both types of ice, but in a different way. In frazil ice, almost all the salt is rejected at the formation of the ice crystals, whereas in consolidated ice, a part of the salt is rejected in the surrounding water, and a part is trapped inside the ice in the form of brine cells. The brine is then slowly released via drainage channels. For the experiment, we are presenting the practical difference that the consolidated ice will reject less brine than frazil ice.

During the experimental campaign, various conditions were tested to investigate the effects of different parameters (Table 1 is a summary of these conditions). Two temperatures (-10°C and -20°C) were chosen, both within the cold room's operational range (the cold room temperature of -5°C was not selected because ice formation was too slow at this temperature). Three salinities (0 PSU, 34 PSU, and 70 PSU) were used: 0 PSU is fresh water, i.e., the benchmark test, 34 PSU represents typical Antarctic Ocean salinity [192], while 70 PSU, being double, was used to assess the influence of salinity on brine rejection. Three different opening sizes L of the polynya (25 cm, 35 cm, and 45 cm) were tested to determine if a wider opening would amplify the effect of brine rejection. Lastly, two geometries (vertical wall and 45° inclined wall) were examined to compare the flow behavior on a slope versus a vertical surface. The different combinations of the parameters give 24 cases with salt and two cases without salt (i.e., a total of 26 different cases). For the control tests without salt, only the geometry was changed, the air temperature was set to -20°C, and the opening size to 35 cm. For each combination of the parameters, the experiment was repeated at least twice to ensure repeatability, obtaining a total of 83 experiments with salt and 10 experiments without salt.

Table 1: The different experimental conditions.

Opening size L	25 cm	35 cm	45 cm
Temperature	-10°C	-20°C	
Salinity	0 PSU	34 PSU	70 PSU
Geometry	Vertical wall	45 degree inclined wall	

8.3 Pre-processing of the measures

In the 83 experiments conducted with salt water, the water in the tank exhibited some kinematic patterns resembling gravity currents or convective cells. These patterns will be presented in detail in the Results section.

Note that the duration of ice formation and brine release is significantly longer than the 30-minute interval during which we acquire velocity measurements. Velocity measurements are initiated once the first layer of ice has formed. We can therefore consider that this experimental window allows us to observe the velocity field in a (statistically) quasi steady-state.

Among these saline experiments, some were found to be fairly steady (albeit with fluctuations) during the 30 minutes of the recording, while others showed clear trends; namely, the velocity field and flow rate of the brine-induced gravity current showed a significant temporal evolution and were not in a statistically steady state. It follows that a selection was necessary to identify the most reliable cases. The aim was, in fact, to obtain a pseudo-steady state (possibly after an initial period of flow pattern formation) that lasts for 30 minutes, in which it was then possible to average to eliminate short-term fluctuations.

To select the steady cases, the flow rate of the observed current was calculated at eight regularly spaced depths along the wall, using the vector field retrieved by PIVlab (see Fig. 53). To determine the flow rate at a specific point, the velocity was integrated along a line normal to the wall. The axis normal to the wall changes depending on the geometry of the experiment. For the case with a vertical wall, the axis normal to the wall is x and the axis parallel to the wall is z, while for the case with the inclined wall, the axis normal to the wall is x^* and the axis parallel to the wall is z^* (see Fig. 53).

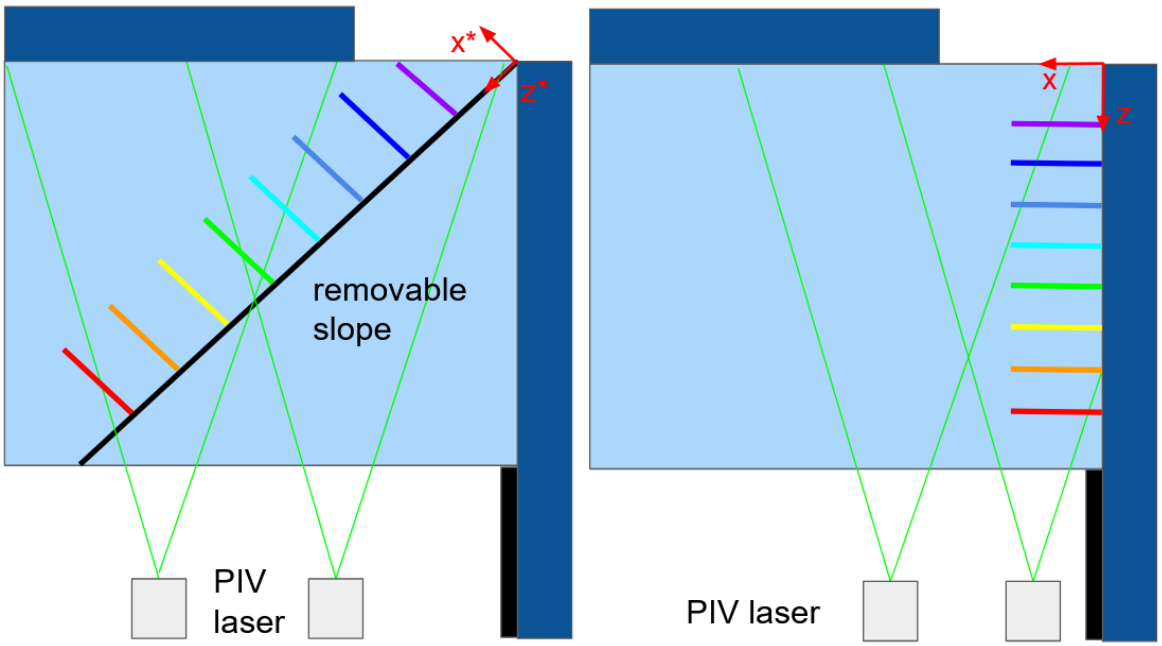

Fig. 23: Localization of the sections (perpendicular to the wall) where the velocity profiles were measured and flow rates were evaluated. The colors of the sections are the same as the colors of the velocity profiles reported in Fig. 27.

The integration was carried out over the distance from the wall to the location where the velocity component parallel to the wall (z or z^*, depending on the geometry) becomes zero. This gives a result in cm^2/s, which is a planar flow rate (the flow being considered planar as will be explained in more detail in the Result section). This calculation was performed for one frame every 10 frames, resulting in one value every 0.8 seconds. This gives a total of 2,250 images for each experiment. This generated a time series of flow rates at different transects along the slope, showing the flow evolution over time. Only experiments exhibiting simple oscillation patterns around a mean value, with no particular trend, were retained. The Student's t-test [3] was applied to the time series to test for the presence of a trend: when the p-value was greater than 0.05, no significant statistical trend was assumed. Fig. 54 shows one of these time series in which there are fluctuations around a stable mean value, and the trend is non-significant (p-value=0.8).

In this way, we eliminated runs where, due to the imperfect control of the experimental conditions, unsteady kinematic patterns were manifested.

A total of 32 cases successfully passed the stationarity test and were deemed valid for analysis. These included 19 cases with a vertical wall and 13 cases with an inclined wall.

Finally, it is worth noting that some cases were repeated in order to evaluate the reliability of the experiments. In particular, two cases – (i) temperature of -20°C, salinity of 34 PSU, an opening of 45 cm, inclined wall, and (ii) temperature of -20°C, a salinity of 70 PSU, an opening of 35 cm, inclined wall – were repeated four times. In all repetitions, we found differences in the values of q and H less than 10%. This demonstrates that the experiments presented here exhibit a good level of repeatability.

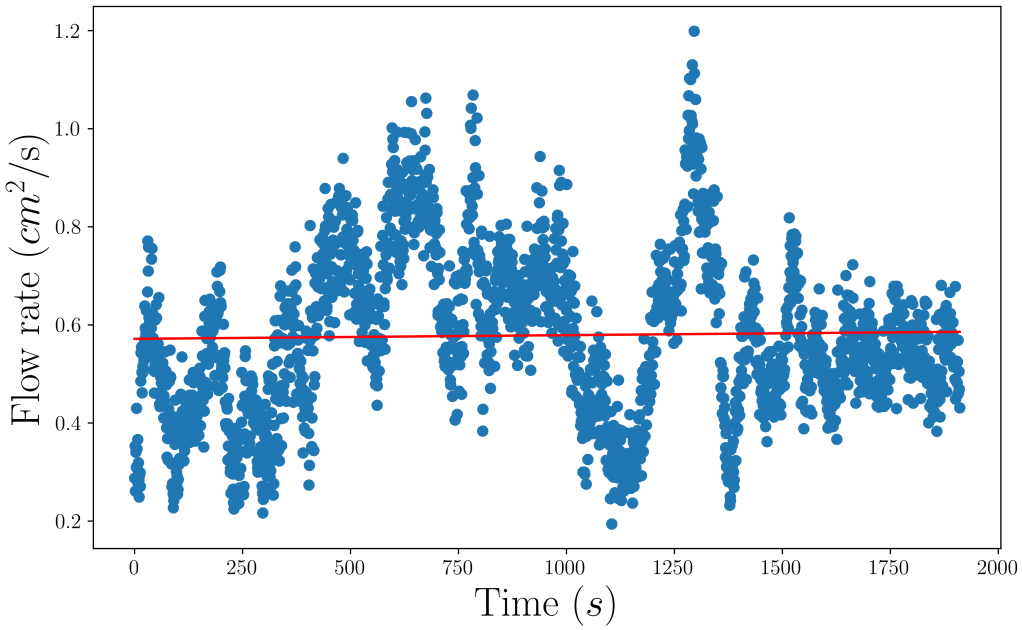

Fig. 24: Flow rate as a function of time in a transect located 30 cm beneath the surface of the water. In red, the linear regression (p-value=0.8, the trend is statistically non-significant). The experimental conditions were: -20°C for the cold room temperature, 35 cm for the polynya opening, an inclined wall of 45 degrees, and a salinity equal to 34 PSU.

Table 2: Number of stable experiments depending on the experimental parameters

	Vertical wall			Inclined wall (45°)		
Number of experiments	25 cm	35 cm	45 cm	25 cm	35 cm	45 cm
34 PSU -20°C	1	1	4	1	2	1
70 PSU -20°C	1	4	1	1	1	1
34 PSU -10°C	1	1	0 data[1]	1	1	1
70 PSU -10°C	1	2	2	1	1	1

[1]Data not available due to backup issues.

9 Results

9.1 Flow fields

The role of brine rejection in generating buoyancy and driving a gravity current was investigated. Figure 25 presents representative cases comparing the velocity field with and without brine rejection. In all experiments, the cold room temperature was set to $-20°C$, and the polynya opening put to 35 cm (from $x = 0$ cm to $x = 35$ cm). Panels (a) and (b) correspond to freshwater control cases, in which no brine rejection occurs, whereas panels (c) and (d) show the saltwater cases (34 PSU). For each pair, the left panel represents an inclined wall configuration and the right panel a vertical wall configuration. The experiments with freshwater were performed to check that the experimental system behaved as expected, that the measurements were correct, and to highlight the key changes due to the salt addition. There are two main differences between the case with the freshwater and that with the salt water. The first one is the dependence of the density on the temperature: for the freshwater, density exhibits a maximum at 4°C, which does not occur for salty water. In our experiments – as the

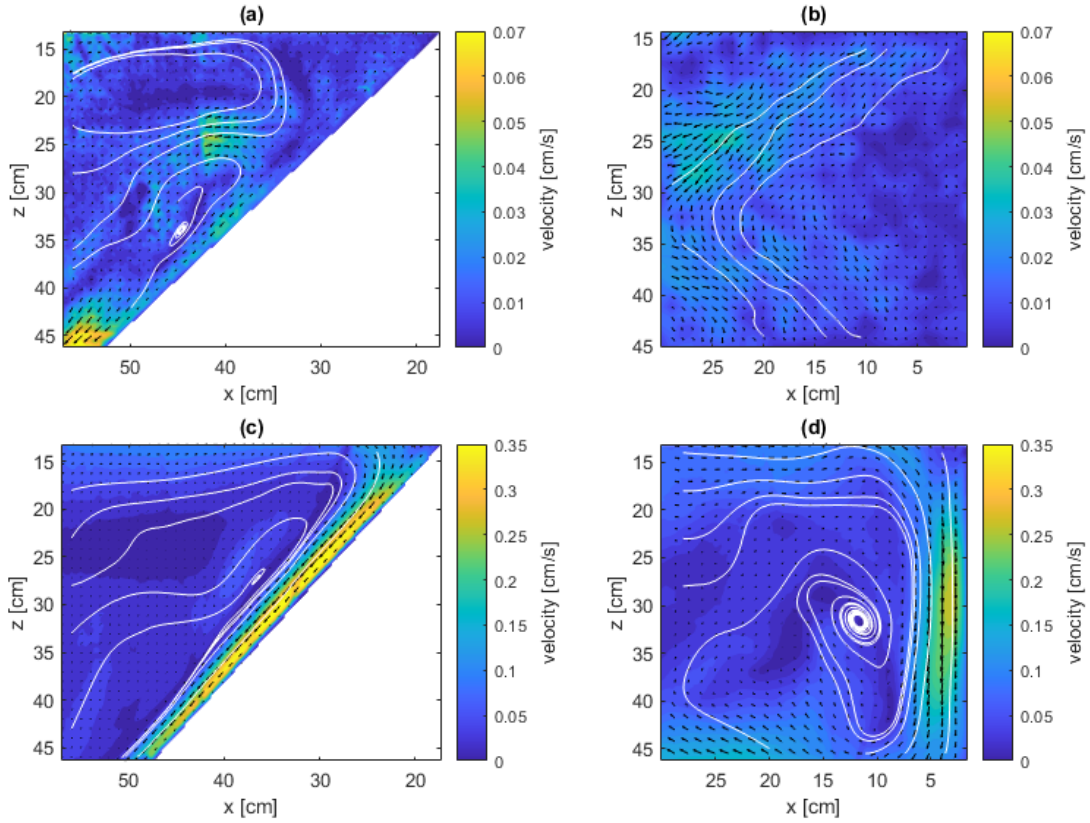

Fig. 25: Mean velocity field averaged over 30 minutes using the velocity field calculated every 0.8 second for a total of 2,250 images. The axes x and z are defined in Fig. 53. The cold room was set to -20°C, and the polynya had an opening size of 35 cm in all four cases (i.e., from $x = 0$ cm to $x = 35$ cm). Panels (**a**) and (**b**) refer to fresh water, while panels (**c**) and (**d**) refer to salt water (34 PSU); left/right correspond to inclined/vertical walls, respectively. It should be noted that the color scales for the fresh and salt water cases are different.

formation of ice at the top of the domain establishes an upper boundary condition of 0°C – the non-monotonic behavior of density leads to a stable stratification in the case of the freshwater. However, it should be noted that, in the experiments, the temperature of the water was nearly uniform and close to 0°C, while the bottom of the tank was only about 0.3°C warmer than the top (a difference close to the precision limit of the temperature measurement), indicating a minimal stratification. The second difference is the brine rejection, which doesn't occur in the freshwater case.

All the measurements presented here are planar and evaluated on the vertical measurement plane located at the midpoint of the tank. Other parallel plans showed similar results. In fact, some measurements on a perpendicular plane were made to test the presence of 3D patterns, but no relevant 3D motions were detected. Thus, we consider that the flow is mainly two-dimensional and that the middle plane is representative of all other parallel planes.

Four cases are compared in Fig. 25: 45° inclined wall and fresh water (panel **(a)**), vertical wall and fresh water (panel **(b)**), 45° inclined wall and salt water (panel **(c)**), and 45° inclined wall and fresh water (panel **(d)**). In all cases, the cold room was set to a temperature of -20°C, and the polynya had an opening size of 35 cm (the free-surface opening extends from $x = 0$ cm to $x = 35$ cm, see Fig. 22). In Fig. 25, the location of the polynya-like opening is on $z = 0$ cm, above the image.

Fig. 25 shows a marked difference between the experiments with and without salt. The experiments with salt water exhibit distinct gravity currents along the wall, whereas the experiments with fresh water show a (weak) cellular pattern (panels **(a)**) or incoherent movements (panels **(b)**). The magnitude of the velocity field also differs significantly between salt and fresh conditions. In the fresh water, the velocity magnitude is of the order of 10^{-2} cm/s (0.025 cm/s for the vertical wall and 0.035 cm/s in the case of the inclined wall), while in the salt water condition, it is of the order of 10^{-1} cm/s (0.2 cm/s and 0.25 cm/s in the case of the vertical and the inclined wall, respectively). In the fresh water, the small movements are quite randomly distributed, erratic, and are unable to create clear flow patterns. Additionally, we noted a considerable variability of the velocity field (particularly in the case of the vertical wall) between different realizations of the same experimental conditions; this demonstrates the lack of a clear pattern and the extreme sensitivity to small differences in initial or boundary conditions. Thus, in the absence of salt, the water is almost at rest, with very weak residual cellular or incoherent motions arising from the stirring of the water at the start of the experiment.

In contrast, when salt was present, the formation of a clear gravity current along the wall was observed, and velocities were an order of magnitude greater than in the freshwater case. This current was consistently observed across all experiments, with variations between experiments being much less pronounced than those in the fresh water condition. Therefore, the presence of salt in the water has a significant impact, which can be attributed to the brine rejection. The temperature measurements show a homogeneous temperature along the wall. This strengthens the relationship between observed currents and brine rejection to the exclusion of potential thermal effects. In polynyas, brine rejection acts as a source of buoyancy, increasing local salinity and, consequently, water density.

A notable difference between the experiments with a vertical wall and an inclined wall occurs (see Fig. 25 panels **(b)** and (**d**)): in the case of an inclined wall, the current develops over a greater length and becomes more pronounced and localized along the wall. The vertical velocity gradient along the wall is far greater in the case with the inclined wall. This can be due to two effects: the first is linked to the greater length of the inclined wall (about 1.4 longer than the vertical one), and the second effect is the capability of the inclined wall to intercept the brine rejection over almost the entire length of the opening at $z = 0$ cm; differently, the vertical wall 'collects' the salt released by the freezing of the water in a smaller portion of the polynya-like opening.

9.2 Vorticity fields

To gain a clearer understanding of the general flow structure, it is insightful to analyze the vorticity fields presented in Fig. 26. Similar to the velocity fields, these plots reveal a stark contrast between the cases without salt water (Fig. 26a-c) and those with salt water (Fig. 26b-d). In the former, no distinct spatial patterns in the vorticity are observed, indicating the unstructured nature of the flow. Conversely, the saltwater cases display layers of vorticity with opposite signs emerging near the lateral walls, whether inclined or not.

Understanding these patterns requires recalling that vorticity arises from two primary mechanisms. The first is the diffusion of (positive) vorticity from the walls, driven by velocity gradients imposed by the no-slip boundary condition. The second is the generation of vorticity due to density gradients, also referred to as 'baroclinic generation of vorticity' [220], expressed as $\vec{S}_\rho \times \vec{g}$, where $\vec{S}_\rho = \nabla(\ln \rho)$ is the so-called stratification vector. Close to the solid boundary, the flow develops a thin layer of positive (i.e., counterclockwise) vorticity, highlighting the dominant role of positive velocity gradients imposed by the no-slip condition at the wall (Fig. 26). This thin layer is overlain by a thicker layer of negative

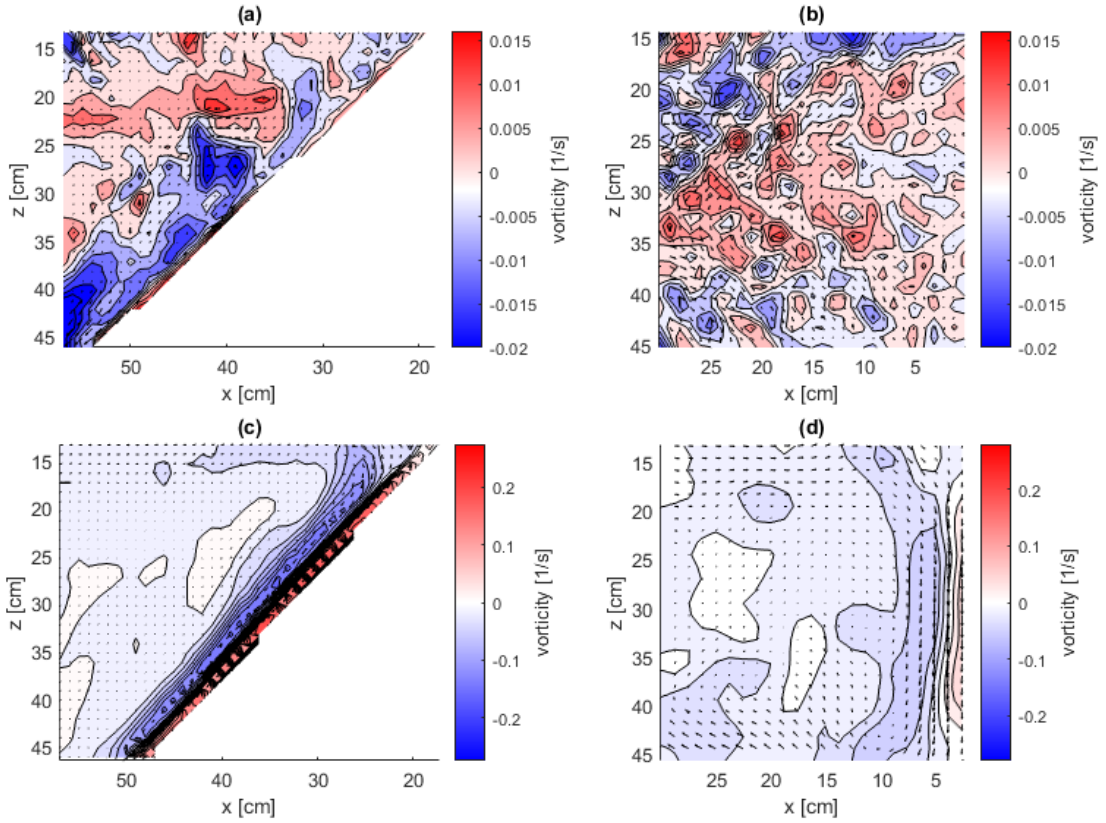

Fig. 26: The figure shows the same velocity fields as in Fig. 25, reporting the vorticity field in the background.

vorticity due to the action of $\vec{S}_\rho$. This pattern therefore reflects the persistent presence of a denser fluid layer flowing along the lateral walls, driven by continuous brine rejection at the water surface.

The two saltwater cases also exhibit a background of negative vorticity, indicating the presence of a wall-structured, clockwise, large-scale recirculating motion induced by the sinking of the dense fluid layer.

9.3 Velocity profiles

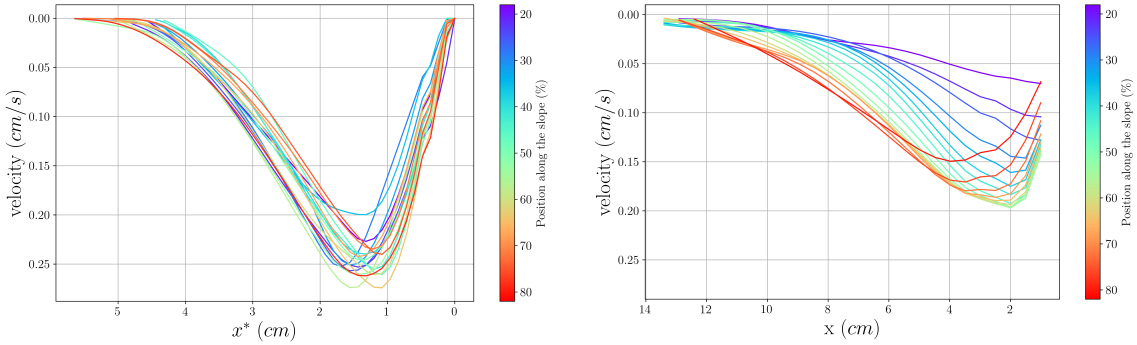

Fig. 27: Velocity profiles at different transects along the inclined (on the left) and the vertical (on the right) walls. The color represents the percentage of the wall length traveled by the current: 0% is the freezing free-surface and 100% is the bottom of the tank.

To describe the kinematics of the gravity current along the wall, some velocity profiles were evaluated (see Fig. 27). The velocity profiles were located uniformly along the wall; their positions are shown in Fig. 53. The axes along which the velocity profiles are taken are x^* for the inclined wall and x for the vertical wall as defined in Fig. 53. The component of the velocity that is shown is parallel to the wall (i.e., along the z and z^* axis, respectively). Velocity profiles are obtained from the velocity field averaged over 30 minutes in the measurement window; the flow regions close to the surface and the bottom were not measured. In the case of the vertical wall, a zone of around 0.1 cm from the wall could not have been measured due to technical limitations in the PIVlab software. This explains why the velocity is not seen reaching zero at the wall when the wall is vertical; this limitation was not present in the inclined case, allowing for more accurate measurements near the wall. The profiles are shown from the wall to the point where the velocity reaches zero.

Two cases are presented: one refers to the vertical wall and one to the inclined wall. These two cases represent well what was observed in the other experiments. Both cases had identical experimental conditions, except for the wall geometry; specifically, the cold room temperature was -20°C, the salinity was 34 PSU, and the polynya opening size was 35 cm.

Vertical and inclined walls exhibit common features: they show comparable velocities (around 0.1-0.2 cm/s), profiles have similar shapes, and, starting from 60% along the vertical wall, profiles are quantitatively quite similar to those measured on the inclined wall. However, they also exhibit some key differences. The first notable difference is the thickness of the gravity current, that is, the distance from the wall to the point where the velocity reaches zero. It is larger in the case of the vertical wall (about 12 cm) than in the case of the inclined wall (about 5 cm). This can again be attributed to geometric factors: the inclined wall facilitates the collection of descending motions (induced by brine rejection) that develop along the full length of the opening, leading to steeper density gradients in the gravity current, which becomes more 'concentrated ' into a reduced thickness. This greater 'salt collection' by the inclined wall also explains the higher velocity reached by the gravity current in the case of an inclined wall.

The second difference is the dependence of the velocity on depth. For the vertical wall, there is a clear progression: the velocity increases and then decreases with depth. The shape also develops from a flat profile to a bell-like profile. In contrast, for the inclined wall, the depth-wise evolution is less pronounced, and the profiles are more similar to each other. The difference between the two cases can be attributed to the different motion patterns: in the case of a vertical wall, a convective cell develops near the wall and we measured a vertical portion of it – therefore, velocity profiles are affected by the curvature of the trajectories in the initial and final measurement sections – instead, in the case of an inclined wall, a density current develops (on a path that is also longer than the vertical wall) which shows an almost self-similarity of the profiles.

The inclined wall case is thus more similar in shape to a classical gravity current, such as one formed by introducing a saline flow into the water, while the vertical wall case exhibits characteristics more akin to Rayleigh-Bénard cells [132]. In both cases, the descent of the denser water generates a large-scale recirculating motion; however, in the inclined wall case, the recirculating cell is more diffuse and less well-defined compared to the more prominent structure observed in the vertical wall case.

9.4 Dependence on experimental parameters

The study investigated the influence of four parameters on the gravity current generated by brine rejection: salinity, external temperature, wall inclination, and opening size of the polynya. Table 3

Table 3: Flow rate and flow thickness depending on the experimental parameters

	Vertical wall			Inclined wall (45°)		
q (10^{-1} cm^2/s)	25 cm	35 cm	45 cm	25 cm	35 cm	45 cm
34 PSU -20°C	20	9.2	13	5.7	6.2	7.7
70 PSU -20°C	11	11	14	4.5	8.2	8.7
34 PSU -10°C	6.1	11	no data[1]	13	11	13
70 PSU -10°C	4.7	14	22	1.7	2.4	3.4

	Vertical wall			Inclined wall (45°)		
H (cm)	25 cm	35 cm	45 cm	25 cm	35 cm	45 cm
34 PSU -20°C	12	12	18	5.1	5.0	6.5
70 PSU -20°C	7.4	7.6	11	4.1	5.2	5.3
34 PSU -10°C	7.4	8.9	no data[1]	9.3	6.9	6.7
70 PSU -10°C	5.8	16	22	3.4	4.6	7.0

[1]Data not available due to backup issues.

illustrates the values of the flow rate (q) and the thickness of the gravity current (H). This latter is defined as the distance from the wall to the point where the z^* component of the velocity reaches zero. The flow rate per unit length (expressed in cm^2/s) is defined as $q = \int_0^H u(x^*)dx^*$, where $u(x^*)$ is the z^*-component of the velocity.

Table 4: Brine-rejection-salt flux, depending on the water salinity and air temperature.

Salt flux	-10°C	-20°C
34 PSU	0.003 $g/m^2/s$	0.01 $g/m^2/s$
70 PSU	0.005 $g/m^2/s$	0.02 $g/m^2/s$

Salt flux measures are presented in Table 4. They were obtained at the end of the experiments by measuring the salinity and the volume of the ice (see Section 2.2). The ice was found to be 20% less salty than the seawater. Additionally, approximately four times more ice formed when the cold room temperature was -20°C compared to -10°C. As expected, measured data indicate that the salt flux increases with higher salinity and lower temperatures. Specifically, the salt flux approximately doubles when the salinity increases from 34 PSU to 70 PSU and quadruples when the temperature decreases from -10°C to -20°C.

Table 3 shows a large variability for both q and H. The flow rate q goes from 0.17 cm^2/s in the case with $L = 25$ cm, 70 PSU salinity, -10°C air temperature, and inclined wall to 0.25 cm^2/s when $L = 45$ cm, 34 PSU, -20°C, and vertical wall. The current width H goes from 1.6 cm for $L = 35$ cm, 70 PSU, -10°C, and vertical wall to 18 cm for $L = 45$ cm, 34 PSU, -20°C, and vertical wall. Thus, there is one order of magnitude difference between the lowest and the greatest values. This difference clearly shows that parameters have an influence on the values of q and H.

The parameter most consistently associated with an increase in both q and H was the opening size of the polynya, as can be seen in Fig. 28. This result aligns with the intuition, as a larger opening size allows for increased ice formation and brine rejection. However, significant variability in the magnitude of this effect was observed. Under constant temperature, salinity, and geometric conditions, increasing the opening size from 25 cm to 45 cm can have an effect that ranges from multiplying the flow rate by 1.25 to multiplying it by 4.5.

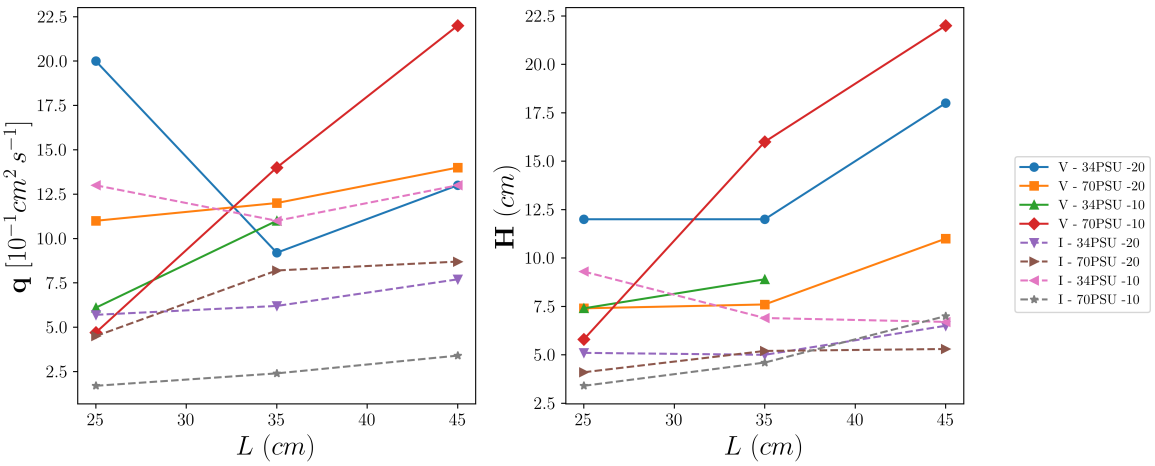

Fig. 28: Influence of the opening size L on **q** and **H**. The vertical wall cases (V) are in solid lines, and the inclined wall cases (I) are in dotted lines.

The geometry of the lateral wall was also found to have a significant impact, as can be seen in Fig. 28. The cases with a vertical wall exhibited higher values of both q and H compared to the same case with the other geometry. Similarly to the opening size effect, the range of the influence of the geometry varied considerably, ranging from negligible changes to a doubling of the flow rate. This variation is likely due to the increase in mixing and friction along the longer flow path when an inclined wall is present and the smaller effect of gravity due to the angle.

The role of water salinity was not as clear as that of the size of the polynya opening and the slope. As indicated by results reported in Table 4, the salt flux increases with salinity, suggesting that the flow rate q should also increase with higher salinity. In Table 3, this trend is observed for q in the majority of cases; however, exceptions occur for the opening size of 25 cm with the vertical wall and for half of the cases with the inclined wall. In general, the increase of q with salinity is quite small. Differently, for H, no significant trend was observed with respect to salinity.

The role of temperature in the experiments remains somewhat ambiguous. The expected outcome is that lower temperatures would lead to increased ice formation, resulting in greater brine rejection and, consequently, a higher flow rate. This expectation is supported by the data in Table 4, where a clear increase in salt flux is observed at lower temperatures. However, in Table 3, the values of q were not consistently higher in the lower temperature cases (-20°C). In fact, in many instances, the opposite trend was observed. For H, no significant trend was observed with respect to temperature.

9.5 Discussion

As highlighted in Table 3, there are two clear trends that arise from our results: (i) the effect of the opening of the polynya and (ii) the effect of the slope. Both q and H increased with the increase of the opening, and both q and H were greater in the case of the vertical wall than in the case of the slope, all other parameters being equal. The effect of the temperature and the salinity is, instead, not so clear. It would be expected that the decrease in the temperature and the increase in the salinity should give greater q. Table 4 clearly indicates that the salt flow induced by brine rejection followed this trend. Table 3 shows that in the case of the salinity, q seems to increase with the increase of salinity, but not H. Conversely, neither q nor H was found to follow a particular trend with respect

to the temperature. This is surprising and remains unexplained. Further experiments will be needed to clarify this behavior.

Apart from understanding the role of the different parameters, the results of Table 4 also allow us to conduct a scaling analysis that can help explain the order of the average velocity measured in the experiments. Table 4 indicates a salt flux on the order of 10^{-2} g/m^2/s at -20 C for a salinity of the water of 34 PSU. For these conditions and an opening size of 35 cm, the average velocity was found to be on the order of magnitude of a few millimeters per second. Given that the surface area of the polynya is 0.245 m^2, during the 30-minute duration of a single experiment, this flux results in the injection of approximately 4.4 g of salt. In a total volume of about 0.1 m^3, this leads to an increase in salinity of 0.044 PSU. With the haline contraction coefficient being β_S=0.78 $\times$ 10^{-3} PSU^{-1}, the corresponding relative increase in density is calculated as $\Delta\rho/\rho = \beta_S \Delta S = 3.4 \times 10^{-5}$.

From dimensional analysis, the velocity associated with buoyancy-induced natural convection can be expressed as $u \sim \sqrt{gl\Delta\rho/\rho}$, where l represents the length scale relevant to the flux. In this case, we can select l as the width of the boundary layer, 5 cm. This yields a final average velocity estimate of $u \sim 4$ mm/s, which is what was found in the experiments.

From these values, it is instructive to derive the pure numbers that control the experiments, namely the Prandtl, Reynolds, and Rayleigh numbers. The Prandtl number, Pr=ν/α , where ν is the kinematic viscosity and α is the thermal diffusivity, is equal to 14 for water at the freezing temperature. The Reynolds number reads $Re = uL/\nu$, where u is the typical velocity, L is the length scale, and ν is the kinematic viscosity. The experiments provide u around 0.3 cm/s, and the characteristic length can be set equal to the opening of the polynya, namely $L = 35$ cm. This provides $Re \sim 1000$, which is compatible with a laminar flow, in agreement with measurements.

The Rayleigh number reads Ra=$gL^3\Delta\rho/(\mu\alpha)$, where μ is the dynamic viscosity, α is the thermal diffusivity, and $\Delta\rho$ is the density difference induced by the brine rejection. After adopting the order of magnitude analysis reported above, we find $\Delta\rho$=$\rho_0\beta_s\Delta S$=0.034 kg/m^3. This gives a large value of the Rayleigh number, around 5.5×10^7, indicating a prevalence of convection effects as observed in the experiments. In the case of a Rayleigh-Bénard cell, such a large value of the Rayleigh number usually implies a turbulent flow. However, this is not the case in our experiments, where we always observed clear laminar motions.

It is worth comparing the scales of different parameters and measurements from the experiments to their counterparts in the real polynyas. The opening length of a coastal polynya is typically 10 km, the depth of the ocean 3 km, and the inclination of the continental slope 1° to 3°. As for the formation of deep waters, the typical velocity along the slope is 0.5 m/s, and the density difference between the dense water and the surrounding waters at the beginning of the slope is given mainly by the salinity difference, which is 0.2 PSU, which gives a density difference of about 0.7 kg/m^3 [136]. These values imply very large values for both the Rayleigh and the Reynolds number, far beyond their respective critical values.

To compare the experimental case to the field case, the Rayleigh number is much larger in the latter, but the qualitative meaning does not change, always indicating that convection dominates over diffusion. What changes substantially is the Reynolds number, which in the case of ocean polynyas is much larger than the critical one and indicates turbulent convective motions (different from the approximately laminar motions observed in the experiments). This aspect suggests that – although qualitatively the results obtained here are to be considered valid also in real cases (i.e., the existence

of currents totally induced by brine rejection) – caution is needed in transferring the quantitative aspects since turbulence could significantly alter them.

Indeed, some aspects that are not fully understood in the DSW and AABW formation are those regarding turbulent mixing [128]. Therefore, future experiments would have to face this issue. One possible solution would be to increase the brine rejection rate by increasing the heat exchange above the ice (e.g., by means of forced convection).

10 Result summary and closing remarks

Experiments on gravity currents using brine rejection as a source of buoyancy were carried out. The source of buoyancy resembled a polynya-like condition in a controlled laboratory environment. The experiments examined the effects of polynya size, external temperature, water salinity, and bottom geometry on the resulting velocity field.

The key result was to demonstrate that brine rejection is capable of generating clear gravity currents, having a velocity (in our experimental setup) of the order magnitude of millimeters per second. Both the flow rate and the thickness of the current were found to vary depending on the experimental parameters. Specifically, increasing the polynya opening size led to higher flow rates and thicker currents. The flow rate was also slightly increased with the salinity of the water. In addition, the flow rate and current thickness were greater when a vertical wall was present, compared to configurations with an inclined wall. The wall inclination also influenced the structure of the motion due to the brine rejection: the vertical wall induced a cell structure resembling Rayleigh-Bénard flow, while more defined and developed currents were observed along the inclined wall. Finally, changes in external air temperature within the tested range did not significantly influence the flow rate or current thickness, though no clear physical mechanism was identified to explain this result.

The main difference between these experiments and real flow conditions beneath a polynya lies in the Reynolds number. In the laboratory experiments, the Reynolds number is relatively low and the flow remains in a laminar regime, whereas in the ocean the flow is fully turbulent. This difference has important consequences, particularly for mixing at the interface between the gravity current and the ambient fluid, which is significantly more intense at higher Reynolds numbers.

III Numerical simulations of gravity currents along a slope in a stratified ambient

Gravity currents are flows driven by density differences, occurring frequently both in natural environments (e.g., sea breezes, avalanches) and in industrial contexts (e.g., oil spills, brine discharge in estuaries). Owing to their relevance, gravity currents have been extensively investigated. Among them, some propagate downslope into a stratified ambient and mix with the ambient fluid, such as the cascading of DSW into the Southern Ocean. These currents penetrate the stratification until reaching an equilibrium. We present numerical simulations designed to investigate how the penetration depth of such gravity currents depends on the slope angle and the strength of the ambient stratification.

The part is structured as follows. We first provide a review of the literature on gravity currents. We then describe the numerical method employed, followed by a validation of the simulations against experimental data. Finally, we present the results obtained from the numerical simulations.

11 Literature review on gravity currents

11.1 Generalities on gravity currents

Some fundamental parameters characterize gravity currents, including the current density ρ, the ambient fluid density ρ_a, the current thickness h, the density difference between the current and the ambient fluid $\Delta\rho = \rho - \rho_a$, and the corresponding reduced gravity $g' = g\,\Delta\rho/\rho_a$. A schematic representation of a gravity current illustrating these parameters is provided in Figure 29.

A gravity current typically consists of three main regions: the front, the head, and the body. These regions are illustrated in Figure 30, where the arrows indicate the velocity field. The front represents the interface between the ambient fluid and the gravity current, and its velocity is often analyzed to characterize the current's propagation. Immediately behind the front lies the head, which is thicker than the remainder of the current – approximately twice as thick, according to Simpson et al. [183] – and contains most of the current's buoyancy. The resulting pressure imbalance, created by the momentum difference between the head and the ambient fluid, forces the flow to bulge. The body constitutes the bulk of the current that follows the head.

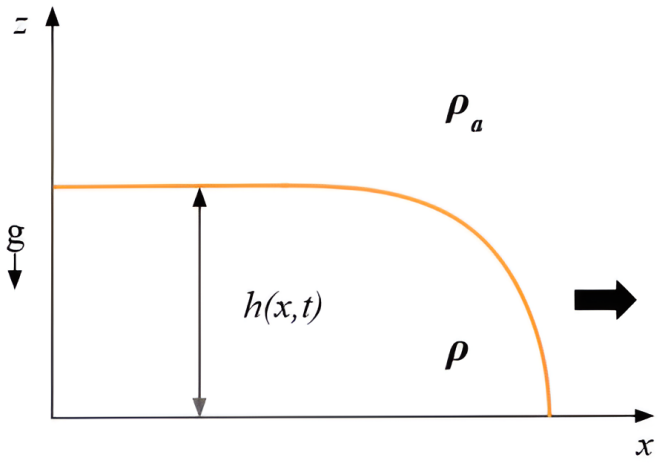

Fig. 29: Schematic representation of a gravity current. The orange line marks the interface between the current and the surrounding fluid. The flow propagates from left to right, as indicated by the arrow.

Gravity currents can be characterized and classified based on two key parameters: the density difference between the current and the ambient fluid, and the characteristics of the source.

Categories related to density difference

1. When the gravity current is lighter than the ambient fluid, the current is called an upper gravity current. This is the case of oil spillage into water or fumes from chimneys.

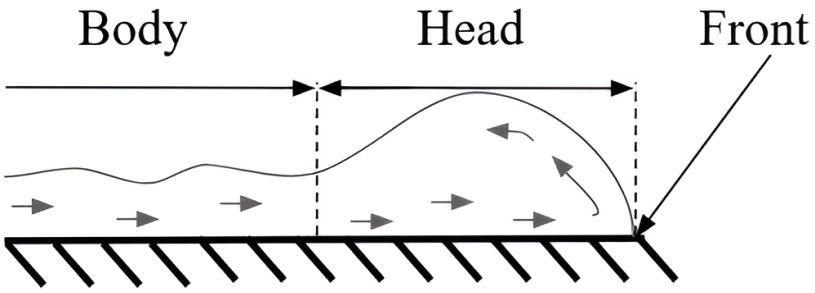

Fig. 30: Schematic representation of the different parts of a gravity current.

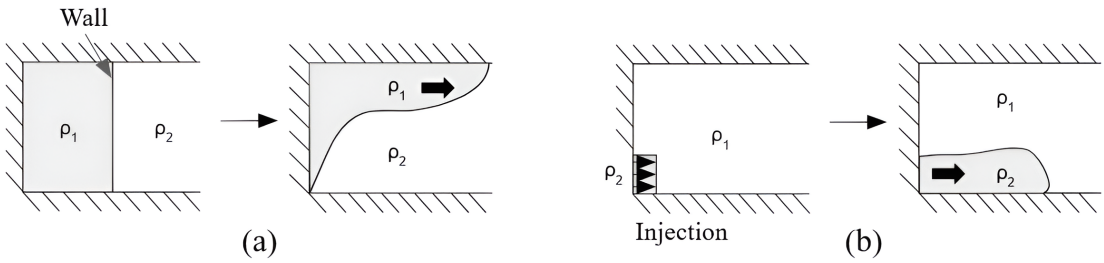

Fig. 31: Schematic illustration of two types of gravity currents: (a) fixed-volume release and (b) continuous supply. The fluids have densities $\rho_1 < \rho_2$. In panel (a), the fluids are initially separated by a barrier (left), and the current develops once the barrier is removed (right). In panel (b), the denser fluid is continuously injected into the lighter ambient with a prescribed velocity.

2. When the gravity current is heavier than the ambient fluid, it is called a bottom gravity current. This is the case of turbidity currents, avalanches, pyroclastic flows, etc.
3. When the ambient fluid is stratified (i.e., forming layers of different densities) and the gravity current has an intermediate density with respect to different layers, it is called an intrusive current. In this case, the density difference $\Delta\rho$ is interpreted as the difference between ρ and the density of the layer of the stratification that the current first encounters (typically the upper layer).

If the density difference between the gravity current and the ambient fluid is smaller than 10%, then the Boussinesq approximation can be used, which assumes a constant density in the Navier-Stokes equations except where it is multiplied by gravity g. This allows for a significant simplification of the equation.

If the density difference is greater than 10%, then the current instead is considered non-Boussinesq. An important difference between Boussinesq and non-Boussinesq currents is the head thickness. As the lighter fluid opposes a lot less resistance to the progression of the flow in the non-Boussinesq case, the head does not gain as much thickness as in the Boussinesq case. The Boussinesq currents have been by far the most extensively studied (e.g., [20, 173]), while non-Boussinesq currents have also been the focus of several important investigations (e.g., [50, 108]).

Categories related to the type of the source

1. When the gravity current is produced by the sudden release of a fixed volume of a fluid with a different density into an ambient fluid, it is called a constant-volume or lock-exchange gravity current (see Figure 31a). Examples include dam breaks or avalanches.
2. When the gravity current is produced by a continuous source, it is called a continuous release gravity current (see Figure 31b). Examples include pyroclastic flows or oil spills.

Dimensionless numbers

The behavior of the gravity currents may be described by a few dimensionless numbers that are ratios between some important parameters of the flow. These numbers are:

1. the Reynolds number: $Re = UH/\nu$, where U is a characteristic velocity, H is a length scale (typically the current depth), and ν is the kinematic viscosity. Reynolds number quantifies the relative importance of inertial to viscous forces. It determines whether the flow is laminar, transitional, or turbulent. Most laboratory and environmental gravity currents operate at moderate to high Reynolds numbers, where turbulence plays a significant role;

2. the Froude number: $Fr = U/\sqrt{g\prime H}$. It expresses the ratio of inertial to buoyancy forces and is crucial in defining flow regimes such as subcritical or supercritical propagation. The Froude number governs front speed and is often used in theoretical predictions;

3. the Richardson number: $Ri = g\prime H/U^2 = Fr^{-2}$. It measures the ratio of potential to kinetic energy and is a key parameter in stability analyses. A low Richardson number (typically $Ri < 0.25$) indicates a flow susceptible to shear instabilities like Kelvin–Helmholtz, whereas higher values correspond to more stable, stratified currents.

These dimensionless numbers provide a framework to analyze and compare gravity current behavior across laboratory, numerical, and field scales.

11.2 Behavior of gravity current on a horizontal plane

Gravity currents were first studied by Theodore von Kármán in 1940 [209], who applied Bernoulli's theorem to the streamline separating the current from the ambient, assuming that the ambient was in motion while the current remained at rest (see Figure 32a). This led to the following expression for the velocity of the head:

$$u = \sqrt{\frac{2gh\Delta\rho}{\rho_a}}, \tag{3}$$

where h is the height of the head of the current. The limitation of this approach is that, due to the assumptions made in applying Bernoulli's theorem, no mixing between the current and its environment was allowed.

Thomas Brooke Benjamin later extended von Kármán's work [20]; considering a continuous source of buoyancy in a confined environment and performing a mass and momentum balance while neglecting friction and entrainment in a non-dissipative case (see Figure 32b). From this analysis, he obtained the following expression for the front velocity:

$$u = \sqrt{\frac{gh\Delta\rho(2H-h)H(H-h)^2}{\rho_a H^2}}, \tag{4}$$

where H is the height of the confined environment and h the thickness of the current. Furthermore, he demonstrated that h can take only two values, 0 and $H/2$. A lower value of h would imply a dissipative current. According to Benjamin, the Froude number should always equal 0.5 for a non-dissipative current. If $Fr < 0.5$, this indicates the presence of dissipation (e.g., due to friction), whereas if $Fr > 0.5$, it suggests that external energy is supplied (e.g., through continuous injection). This study was highly influential.

One of the most common methods to study fixed-volume gravity currents in the laboratory is the lock-exchange technique. The classical setup consists of a tank of water in which a reservoir of denser liquid (typically brine) is placed on one side, separated from the rest of the fluid by a removable wall.

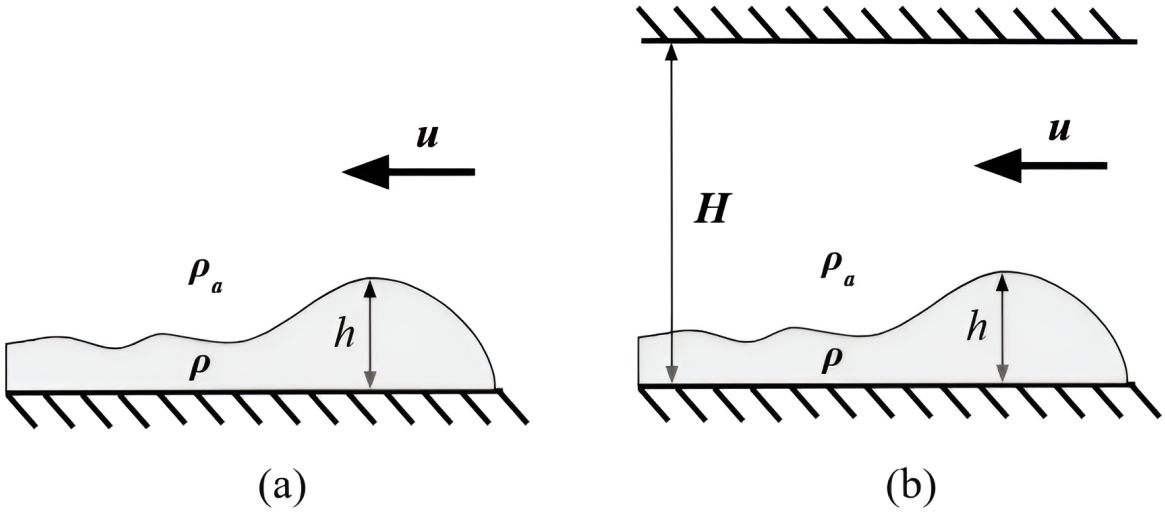

Fig. 32: Schematic representation of the gravity currents theoretically analyzed by von Kármán [209] (panel (a)) and Benjamin [20] (panel (b)). In both cases, the gravity current is treated as stationary, while the ambient fluid approaches it with velocity U. Benjamin's formulation further considers a confined ambient of height H.

The experiment begins when the wall is removed, and the denser fluid propagates into the ambient fluid due to the difference in hydrostatic pressure.

One of the first important experimental studies employing a lock-exchange configuration was conducted by Huppert and Simpson (1980) [97]. They were the first to challenge Benjamin's model through systematic laboratory experiments using brine. In their work, they identified two distinct regimes for the Froude number. In the first regime, the Froude number remains constant when the ambient depth is large compared to the current height. In the second regime, the head Froude number scales as:

$$\mathrm{Fr}_H \propto \left(\frac{h}{H}\right)^{-1/3}. \tag{5}$$

Compared to Benjamin's theoretical prediction ($Fr = 0.5$), the measured Froude number was smaller, likely due to frictional effects present in the experiments. Since the scaling proposed by Huppert and Simpson is based on experimental evidence, it is often preferable to use it rather than the purely theoretical law, which neglects a number of aspects inherent in real flows.

In addition to these insights on the Froude number, Huppert and Simpson also identified three distinct stages in the evolution of a gravity current:

1. the *slumping phase*, during which the front advances at nearly constant speed due to gravitational collapse;
2. the *inertial phase*, characterized by gradual deceleration as buoyancy and inertia reach equilibrium,
3. the *viscous phase*, during which viscous diffusion dominates and further decelerates the flow.

Fay [63] later proposed different laws for the propagation of gravity currents depending on the phase:

$$\begin{cases} \text{slumping phase} & x_f \propto t \\ \text{inertial phase} & x_f \propto t^{2/3} \\ \text{viscous phase} & x_f \propto t^{1/5} \end{cases}$$

where x_f is the position of the front and t the time.

The study of the Froude number in gravity currents has been particularly fruitful, and numerous other formulations have been proposed in the literature.

The most common technique for creating a continuous gravity current in the laboratory is to connect a pipe to a reservoir of dense fluid (typically brine) and discharge it into a tank containing a lighter fluid (usually water). Unlike the lock-exchange configuration, where a finite volume of dense fluid is suddenly released, this setup provides a sustained injection of dense fluid into the ambient environment. Such a configuration is particularly relevant to geophysical and industrial flows, for instance, brine discharge into estuaries, pyroclastic flows, or dense overflows from marginal seas.

In this configuration, the source continuously releases a fluid, and the behavior of the current can be separated into two phases. The transitional and the stationary regimes. In the transitional phase, the flow propagates inside the observed area. Eventually, the current exits the observed area. The current then enters a statistically steady state, called a stationary state. The continuous release case was first studied by Von Karman [209] and Benjamin [20], followed by many others, among which Ellison and Turner [60], Baines [130], and Ungarish [21].

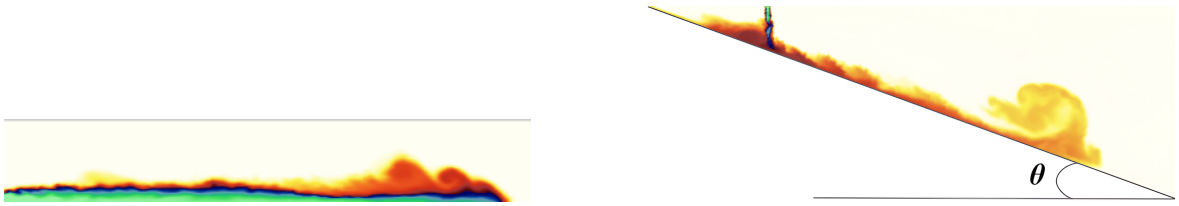

Fig. 33: Gravity current propagating either horizontally (on the left) or downslope (on the right). The color scale represents the fluid density, with darker/green shades indicating denser regions and lighter/yellow shades corresponding to lighter fluid. The visualizations are obtained from the author's numerical simulations.

In the transitional regime, the current exhibits a head followed by a body and propagates similarly to lock-exchange flow. Ungarish [203] demonstrated that this regime can be mathematically treated as equivalent to the finite-volume case.

The stationary regime, by contrast, is characterized by the absence of a head, with only the body of the current persisting. Its properties, such as velocity, become statistically steady. Beyond an initial adjustment zone near the source, the current develops into a self-similar state, in which the normalized velocity profiles remain invariant with distance from the source.

11.3 Influence of the slope

The presence of an inclined boundary significantly alters the dynamics of gravity currents compared to horizontal configurations that have been discussed so far. The slope enhances the component of gravitational acceleration acting along the direction of flow, resulting in increased front velocities and modified internal structures. Understanding the effect that the slope has on gravity currents is one of the main goals of this thesis. The slope angle is defined as the angle between the slope and the horizontal axis and is called θ. This means that $\theta = 0°$ is a horizontal plane and $\theta = 90°$ is a vertical wall (see Figure 33b).

Two pioneering studies on inclined gravity currents are those of Britter and Linden (1979) [26] and Beghin (1981) [18]. Both performed experiments on gravity currents using a wide range of slope angles (from 5° to 90°).

Britter and Linden [26] identified two dominant propagation regimes: an initial inertia-buoyancy phase where the front advances with a nearly constant velocity due to a balance between inertial and gravitational forces, and a later viscous-buoyancy phase where viscous effects become increasingly significant, causing a nonlinear deceleration of the front. The first phase of nearly constant head velocity was found for angles larger than 0.5°. For smaller angles, head velocity decreased with increasing distance from the source.

Britter and Linden [26] also demonstrate that the nondimensional ratio $u/(B_l)^{1/3}$ – where u is the velocity of the head of the current and $B_l = \Delta\rho\, g\, uh/\rho_a$ denotes the buoyancy flux – remains constant regardless of the slope angle. This result was later confirmed by Fernandez et al. [64]. This means that the nondimensional velocity of the head of the current does not depend on the angle. They interpreted it as an equilibrium between the increase in buoyancy force and entrainment (see Sect. 11.5) with angle.

Beghin et al. [18] focused on avalanche-like flows, performing experiments for gravity currents propagating along inclined surfaces over a wide range of slopes ($5° < \theta < 9°$), using mixtures of fresh

water–salt water or, in some cases, suspensions of fresh water and sand. Their experiment confirmed the findings of Britter and Linden regarding the inertial and viscous phases.

To describe the behavior of gravity currents flowing along a slope, Beghin et al. [18] propose the so-called thermal model, inspired by the classical plume model of [134]. This model is based on conservation equations for mass, momentum, and buoyancy. It assumes that the gravity current, treated as a semi-elliptical 'puff', entrains a portion of the surrounding ambient fluid during its propagation.

This framework was extended to other configurations. Dade et al. [48] adapted the model for compositional gravity currents, where density differences arise from concentration gradients. Dai et al.[52] introduced a detrainment coefficient to account for buoyancy loss in the current head, and [51] further refined the model to include the effects of wall friction in sloped channels.

11.4 Gravity currents in stratified environments

Stratification arises when layers of different densities form due to variations in temperature, salinity, or suspended particles, resulting in a stable vertical density gradient. In the ocean, thermal (temperature) and haline (salinity) stratification produce distinct layers, such as the mixed layer (surface layer where the wind homogenizes the water), pycnocline (a layer of higher density), and deep water, which controls heat and nutrient transport [195]. The Southern Ocean, where DSW typically forms and flows down, is strongly stratified. Figure 34 shows some examples of temperature and salinity patterns in the Southern Ocean, resulting in strong density stratification.

Lakes often exhibit seasonal stratification, with warmer, lighter water forming a surface epilimnion above a denser, colder hypolimnion, separated by a sharp thermocline; this structure can inhibit oxygen replenishment at depth during summer months. In cold weather, another type of stratification occurs: when the surface of the lake freezes, the maximum density of fresh water being at around 4°C, the lake exhibits a stratification with the warmest layers (4°C) at the bottom and the coldest (close to 0°C) at the top [54].

When a gravity current propagates into a stratified ambient, its dynamics are strongly influenced by the background density gradient, which can alter buoyancy fluxes, suppress turbulence, and modify entrainment rates. For instance, in oceanic overflows such as the Mediterranean Outflow into the Atlantic, dense saline water flows along the seafloor and intrudes at a depth determined by the ambient stratification, forming interleaving layers in the thermocline [16]. Similarly, river plumes entering stratified coastal zones often spread horizontally at the pycnocline, creating surface- or mid-depth intrusions depending on the density contrast [38]. In fjord systems, stratification induced by freshwater runoff over saline water can trap dense gravity currents near the bottom, limiting vertical mixing and affecting oxygen renewal in deep basins [201].

The formation of AABW is strongly linked to the stratification of the ocean. If the current flowing from the continental plateau is not dense enough, it will form an intrusion at its neutral buoyancy depth. The dense gravity currents coming from polynyas have even been hypothesized to be responsible for the stratification of the deep ocean and the subsequent sequestration of CO_2 [151]. In summary, the stratification influences the dynamics of a gravity current primarily by reducing or suppressing turbulent mixing with the ambient fluid due to the stabilizing density gradient; in addition, when the current reaches a layer of equal density, it no longer propagates vertically but instead intrudes horizontally along that layer.

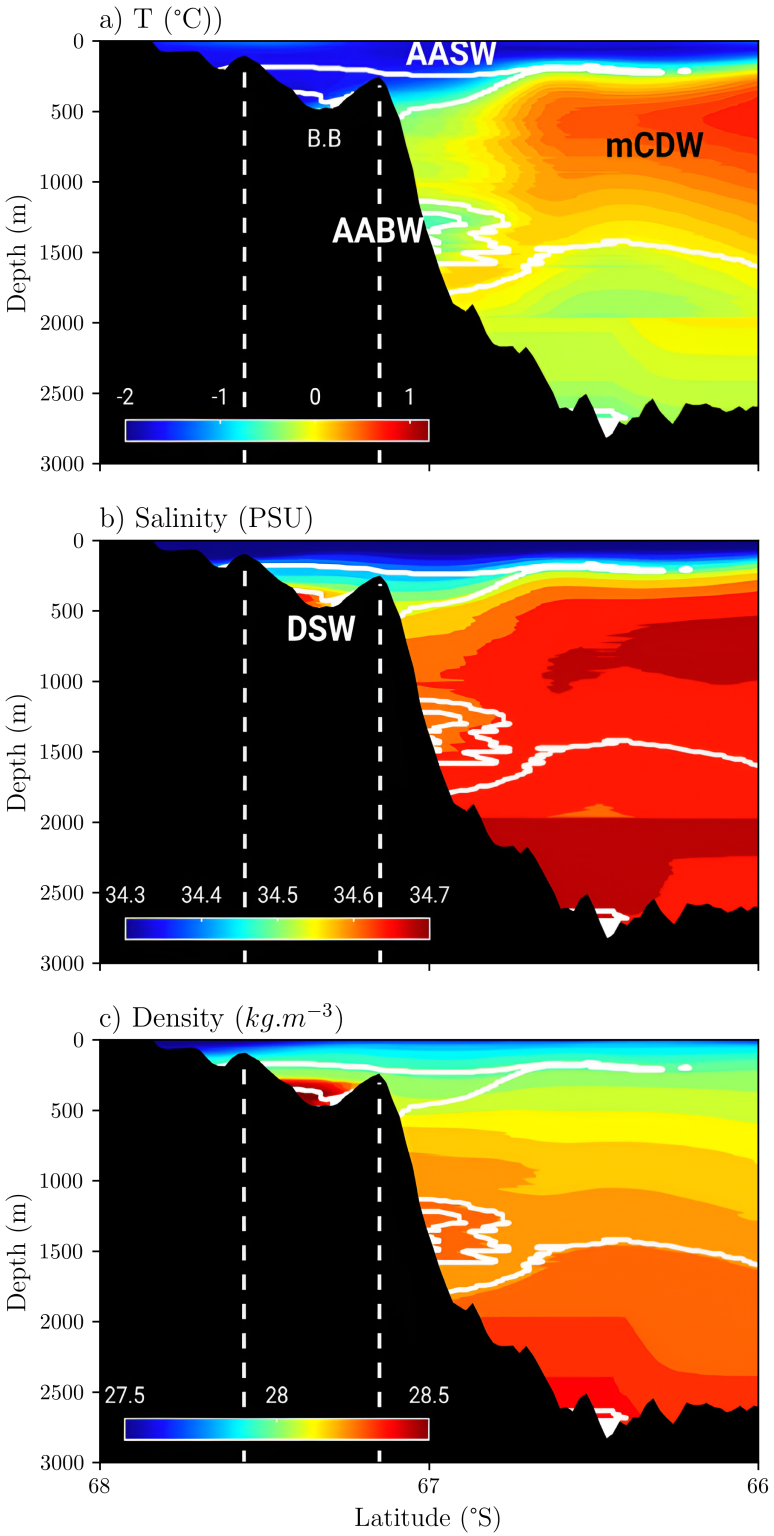

Fig. 34: Cross section of the area of the Burton Basin in eastern Antarctica (68°S, 78°E) showing the stratification of the Southern Ocean in temperature (a), salinity (b), and density (c) averaged over several years of the 20th and 21st century. The white dashed lines represent the limits of the Burton Basin, noted 'B.B' in panels (a). Adapted from [125].

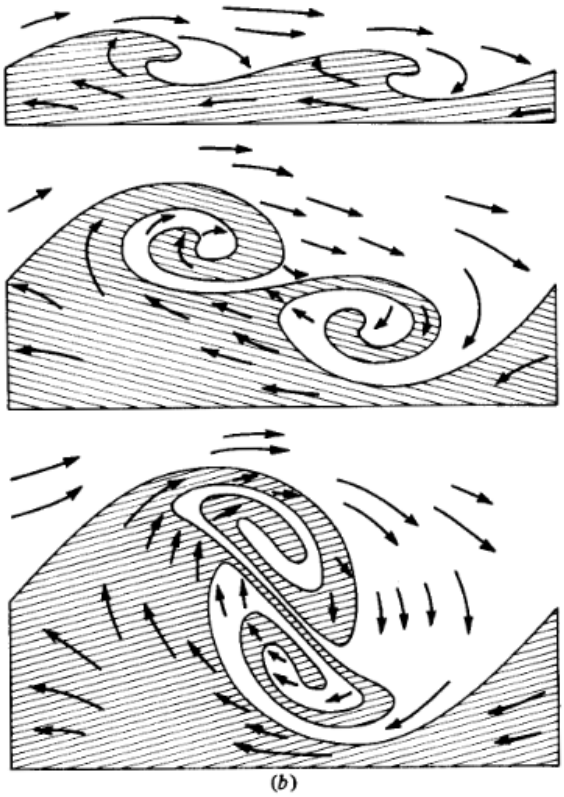

Fig. 35: A visual record of 'engulfing', according to Corcos & Sherman [43].

11.5 Turbulent entrainment

When the gravity current and its environment are miscible, a phenomenon known as entrainment occurs. The gravity current engulfs ambient fluid into itself and, by this process, gains in thickness and gets diluted. This phenomenon occurs at the interface of the two fluids, where the current exerts a shear on the ambient fluid, causing turbulent mixing (see Figure 35). The key parameter that controls the dilution of the current is the entrainment coefficient α.

To give a mathematical description of the entrainment, we place our analysis in a two-dimensional plane (see Figure 29). In this plane, the x-axis is the horizontal direction, the z-axis is the vertical direction, $u(x, z, t)$ is the velocity component along x, and $w(x, z, t)$ is the velocity component along z, $\overline{u}(x, z)$, and $\overline{w}(x, z)$ are the time averaged velocities. We assume a gravity current flowing into an ambient fluid in the x direction. The gravity current is considered to flow along a horizontal boundary; however, the forthcoming analysis also applies to the inclined case, with an appropriate change of coordinates. With this coordinate system defined, the governing equations for the flow can be written, starting with the continuity equation:

$$\frac{\partial \overline{u}}{\partial x} + \frac{\partial \overline{w}}{\partial z} = 0. \tag{6}$$

We define the time-averaged volume flux and specific momentum flux as:

$$Q(x) = \int_0^\infty \overline{u}(x, z)\, \mathrm{d}z\,, \quad M(x) = \int_0^\infty \overline{u}^2(x, z)\, \mathrm{d}z \tag{7}$$

By integrating the equation of continuity 6 along the z axis, and considering that the velocity at the wall is zero, we obtain:

$$\frac{dQ}{dx} = [\overline{w}]_\infty \tag{8}$$

where, $[\overline{w}]_\infty = \overline{w}(x, z = \infty)$ is the value of the vertical velocity component far from the wall.

We use the entrainment hypothesis which states that $-[\overline{w}]_\infty = \alpha \frac{M}{Q}$ and we obtain the formula for the entrainment coefficient α (in the literature one may encounter the notation E or e as well):

$$\alpha = \frac{Q}{M}\frac{dQ}{dx}. \tag{9}$$

This entrainment coefficient is the main tool to quantify the entrainment in plumes and gravity currents. It derives naturally from the entrainment assumption, which states that the mean inflow velocity across the edge of a turbulent flow is proportional to a characteristic velocity, usually the local time-averaged maximum mean velocity or the mean velocity over the cross-section at the level of inflow. This hypothesis was introduced by Sir Geoffrey Taylor in 1949 in a wartime report on the dynamics of hot gases rising in air. The idea was left unpublished and was later rediscovered by Batchelor (1954) and expanded and refined in an article by Morton, Taylor & Turner in 1956 [134].

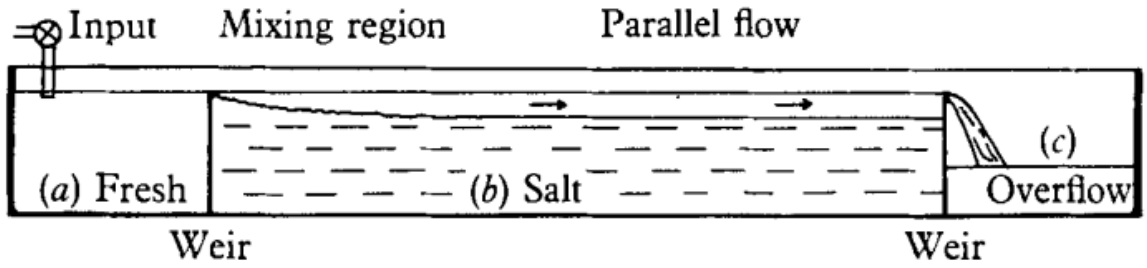

Fig. 36: Experimental setup of Ellison and Turner (1959). Reproduced from [60].

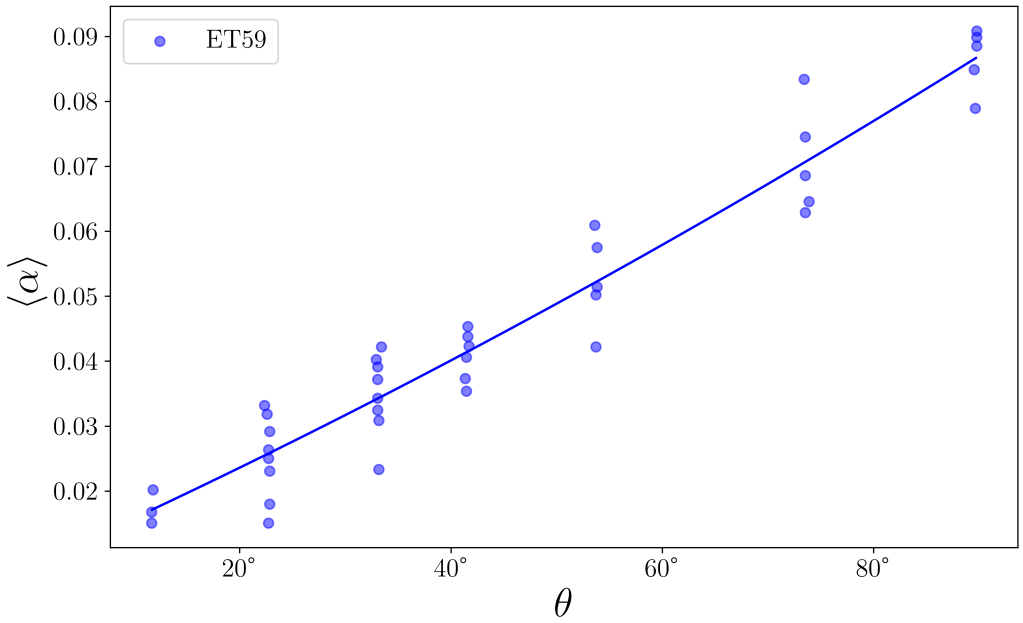

Fig. 37: Measurement of entrainment into an inclined plume as a function of slope. Adapted from Ellison and Turner [60].

The application of the entrainment coefficient to gravity current was presented in a classical article from Ellison and Turner in 1959 [60] (referred here to as **ET59**). In a series of experiments, a dense brine current was released into freshwater (see Figure 36), and the spatially averaged entrainment coefficient $\langle\alpha\rangle$ of the resulting gravity currents was determined by measuring the salinity of the current at the outlet. We define $\langle\cdot\rangle = \frac{1}{L_{x^*}} \int_0^{L_{x^*}} \cdot\, dx^*$, where L_{x^*} is the length of the slope. It represents the spatial average of a quantity along the slope. These measurements were conducted for slope angles ranging from 10° to 90°. They found a linear relationship between the slope angle and the entrainment rate. Specifically, entrainment increases with the slope and reaches a maximum of approximately 0.1 for a vertical plume (90°). Figure 37 reproduces the results of **ET59**. Subsequent research has refined these findings and proposed a variety of empirical laws for the entrainment coefficient, explicitly accounting for the slope angle. Some of these laws are summarized in Table 5. These laws were typically obtained by fitting the observed variation of α as a function of θ using functions that depend solely on the slope angle.

ET59 also observed that entrainment is strongly influenced by the Richardson number, defined in Sect. 11.1, and found that the entrainment coefficient is inversely related to the Richardson number of the gravity current. They proposed an empirical formula for the entrainment coefficient:

$$\alpha = (0.08 - 0.1Ri)/(1 + 5Ri), \tag{10}$$

which applies to all slope angles, as the Richardson number itself varies with the angle. Since then, many other formulations have been proposed. Table 6 summarizes the main formulas relating the entrainment coefficient to the Richardson number, compiled from Chowdhury [40], Fernando [66], and Haddad's PhD dissertation [82].

Table 5: Summary of proposed laws to calculate the entrainment coefficient of a current knowing the angle of the slope. Adapted from [83].

Reference	**Law**	**Remarks**
Pedersen [160]	$0.072\ \sin(\theta)$	-
Briggs [25]	$0.05\ \sin^{2/3}(\theta)$	-
Hopfinger [94]	$9.5 \times 10^{-4}(\theta + 5)$	Law based on **ET59**
	$4 \times 10^{-3}\theta$	Law based on Pedersen [160]
Hughes and Griffiths [96]	$0.1\ \sin(\theta)$	$\theta > 5$
Wells and Wettlaufer [215]	$E_{eq}\ \sin(\theta)$	$\theta > 5$
Sequeiros [179]	$Ri \sin(\theta) - C_D$	No restriction
Haddad [83]	$0.002\ \cos(\theta)\, Ri + 0.09\, sin^{1/2}(\theta)$	-

E_{eq} is the rate of increase of volume flux with depth.
C_D is the drag coefficient.

In summary, the key aspects regarding the entrainment are:

- the mixing between the gravity current and its environment is modeled by the entrainment coefficient α;
- the entrainment coefficient increases with the angle and is maximal in a pure plume, where it is equal to 0.1;

Table 6: Summary of proposed laws to calculate the entrainment coefficient of a current knowing its Richardson number. Adapted from [82].

Reference	Law	Range of validity
Ellison, & Turner [134]	$\frac{0.08-0.1\,Ri}{1+5\,Ri}$	$Ri < 0.8$
Lofquist [112]	$\frac{0.01}{Ri}$	$10 < Ri < 100$
Christdoulou [41]	0.07	$Ri < 0.01$
	$0.007Ri^{-1/2}$	$0.01 < Ri < 0.1$
	$0.002Ri^{-1}$	$0.1 < Ri < 10$
	$0.007Ri^{-3/2}$	$Ri > 10$
G. Parker et al. [155]	$\frac{0.00153}{0.0204+Ri}$	No restriction
G. Parker et al. [156]	$\frac{0.075}{(1+7\,Ri^{2.4})^{0.5}}$	No restriction
Van Kessel & Kranenburg [102]	$\frac{5.5\times10^{-3}}{3.6\,Ri-1+\sqrt{(3.6\,Ri-1)^2+0.15}}$	No restriction
Dallimore et al. [55]	$\frac{C_k\,C_D^{3/2}}{Ri+10(C_k\,C_D^{3/2}+C_s)}$	No restriction
Princevac et al. [165]	$0.05\,Ri^{-0.75}$	$0.15 < Ri < 1.5$
Fernandez & Imberger [65]	$\frac{C_k\,C_D^{3/2}P+C_sT}{RiT+10(C_k\,C_D^{3/2}+C_s)}$	No restriction
Johnson & Hogg [100]	$\frac{0.075}{1+27\,Ri}$	No restriction
Van Reeuwijk et al. [207]	$0.31(Ri_{\max}-Ri)$	$Ri < 0.15$

C_k is a coefficient parameterizing the efficiency of the boundary-introduced turbulent kinetic energy. See [65].

C_s is a coefficient measuring the efficiency of the local shear production. See [65].

C_D is the drag coefficient.

Ri_{max} refers to the maximum Richardson number beyond which entrainment ceases. [207] gives an empirical value of 0.2.

- the value of entrainment is inversely proportional to the Richardson number, which models the stability of the flow. Some authors have argued that past a certain Richardson, the entrainment is negligible;
- the entrainment coefficient is a general concept that can be applied to a variety of conditions: brine/water, dense/light gas, particle-laden/clean water, etc...

Another important step in the understanding of entrainment was the development of the so-called entrainment decomposition. This approach makes it possible to separate entrainment into different physical contributions, allowing a more detailed analysis of the mechanisms at play. The idea was first introduced by Priestley et al. [164], then further developed by Parker, Fukushima, and Pantin [155] in the context of turbidity currents, and later extended to other types of flows by Sequeiros et al. [179] and Paillat and Kaminski [152]. More recent formulations can be found in Salinas [173] and Lanzini [108].

The full derivation of the entrainment decomposition, starting from the mass, momentum, and kinetic energy balance equations, is presented in Appendix A. Here, we only summarize the key concepts needed for interpretation.

We consider a gravity current flowing downslope under the Boussinesq approximation and at high Reynolds number (fully turbulent conditions). Instead of focusing on local pointwise quantities, we describe the flow using integral quantities derived from the velocity and pressure fields. These bulk properties capture the overall structure of the current and provide a convenient framework for analysis. By combining these integral definitions with the Reynolds-averaged Navier–Stokes equations, the entrainment decomposition reads:

$$\alpha_E = \alpha_{prod} + \alpha_{C_D} + \alpha_{Ri} + \alpha_{shape}. \tag{11}$$

These terms can be understood in physical terms as follows:

- α_E is the total entrainment theoretically equal to calculated using eq 9 (see Fig. 60 for a comparison between the two)
- α_{prod} (production term): the main positive contribution, associated with turbulent mixing and the production of turbulent kinetic energy;
- α_{C_D} (drag term): a negative contribution accounting for energy losses due to drag and wall friction;
- α_{Ri} (Richardson term): related to buoyancy effects; its influence increases with slope angle and ambient stratification;
- α_{shape} (shape term): associated with deviations from self-similarity near the source. This term decays to zero as the current evolves downstream and reaches a self-similar state.

Generally, while entrainment associated with turbulence typically provides the main contribution, other effects such as drag, buoyancy, or flow adjustment may become significant in particular regimes.

11.6 Experimental works using a combination of slope and stratification

Several studies, among the earliest of which was Monaghan et al. [131], investigated two-layer stratified environments and highlighted the various outcomes when a gravity current meets a sharp density interface (see Figure 38). Cortes [45] provided a criterion to predict the behavior of the gravity current at the interface between the two densities. We consider a situation with two layers of density ρ_1 and ρ_2 and a gravity current of density ρ_g. If $\rho_1 < \rho_g < \rho_2$, the current intrudes between the two layers (Figure 38a), if $\rho_g > \rho_2$, the current goes to the bottom of the tank (Figure 38b), and if the current has an important internal gradient the current can split, the lighter part intruding and the heavier sinking (Figure 38c). Later studies extended this framework ([170], [175], [215]). These experiments emphasized that the interplay between slope, inflow conditions, and ambient stratification controls whether gravity currents behave as dense bottom-following flows or transform into plumes and intrusions.

Due to its technical difficulties, a limited number of experimental studies were performed for the linearly stratified case. In a linearly stratified ambient, a gravity current flows down until it reaches its layer of neutral density, then it flows horizontally. The point where it stops is called the 'termination point' (see Figure 39), and the distance between the injection and the termination point is called the 'intrusion depth'. The first laboratory experiments were performed by Mitsudera and Baines [130], who first investigated gravity current flowing along a slope into a continuously stratified ambient. Building on this work, Baines [12, 14] systematically explored the influence of slope angle and stratification strength. He conducted a series of constant-inflow laboratory experiments using an experimental setup consisting of a narrow, transparent flume with an adjustable slope, into which dense saline fluid was continuously injected at the top of the slope through a controlled inlet. The ambient fluid was prepared

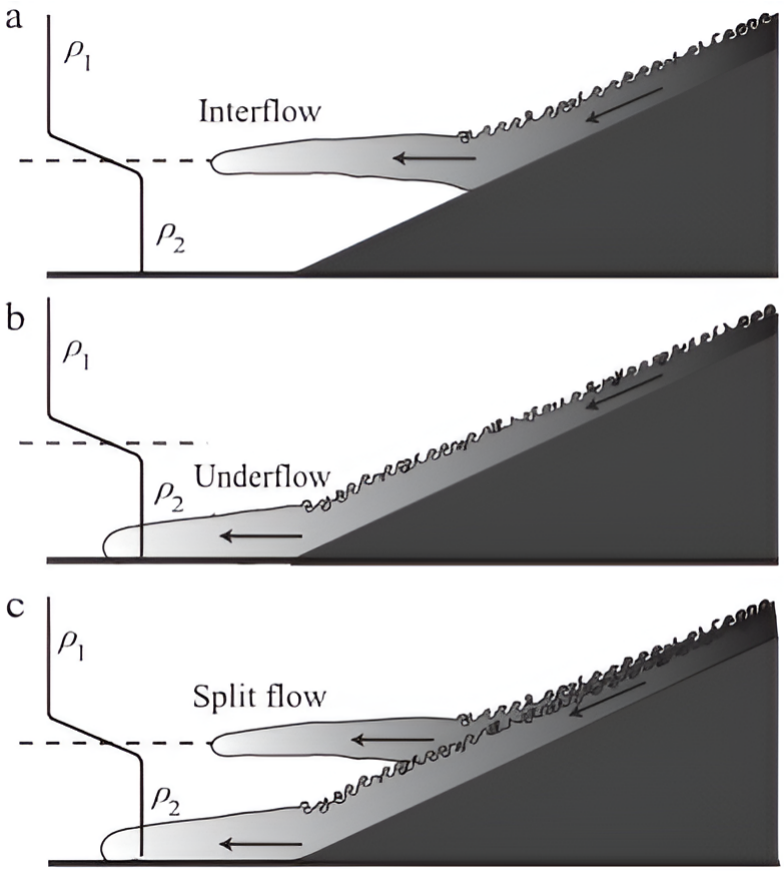

Fig. 38: Behavior of a 2-D gravity current of average density ρ_g in a two-layered stratified environment, ρ_1 and ρ_2. (a) Interflows occur when $\rho_1 < \rho_g < \rho_2$; (b) underflows occur if $\rho_g > \rho_2$, (c) split flows form if the gravity current has significant internal density gradients. Reproduced from [45].

with a stable linear density stratification, generally created using the double-bucket method. In this method, two reservoirs hold fluids of different densities, one light fluid, typically fresh water, and one heavy fluid, typically salty water. These are simultaneously released into a tank through a flow splitter or Y-junction, allowing them to mix gradually and continuously as the tank fills from the bottom up. This controlled co-flux produces a linear vertical density gradient because denser water settles at the bottom and lighter water accumulates near the surface, while mixing occurs along the height. Given the inherent difficulties of the experiments, these currents were more likely to be studied numerically (see Sect. 11.7).

By varying the slope angle and the density difference between the injected current and the stratified ambient, Baines [12] was able to identify two distinct regimes: a detraining gravity current regime at small slopes, characterized by the lateral loss of dense fluid to the ambient, and an entraining plume regime at steeper slopes, where strong turbulent mixing dominated.

Another significant study is the article by Snow and Sutherland [186], who studied turbidity currents flowing into a uniformly stratified environment. They used a configuration similar to that of Baines [12] but extended it to particle-laden flows. They observed fingering, i.e., small intrusions forming as the current goes down because some part of the current reaches their neutral density.

Recently, Zhiguo He and Liang Zhao [88, 89] used a setup similar to that of Baines [12] to perform different experiments. Their equipment uses the lock-exchange method and allows studying small

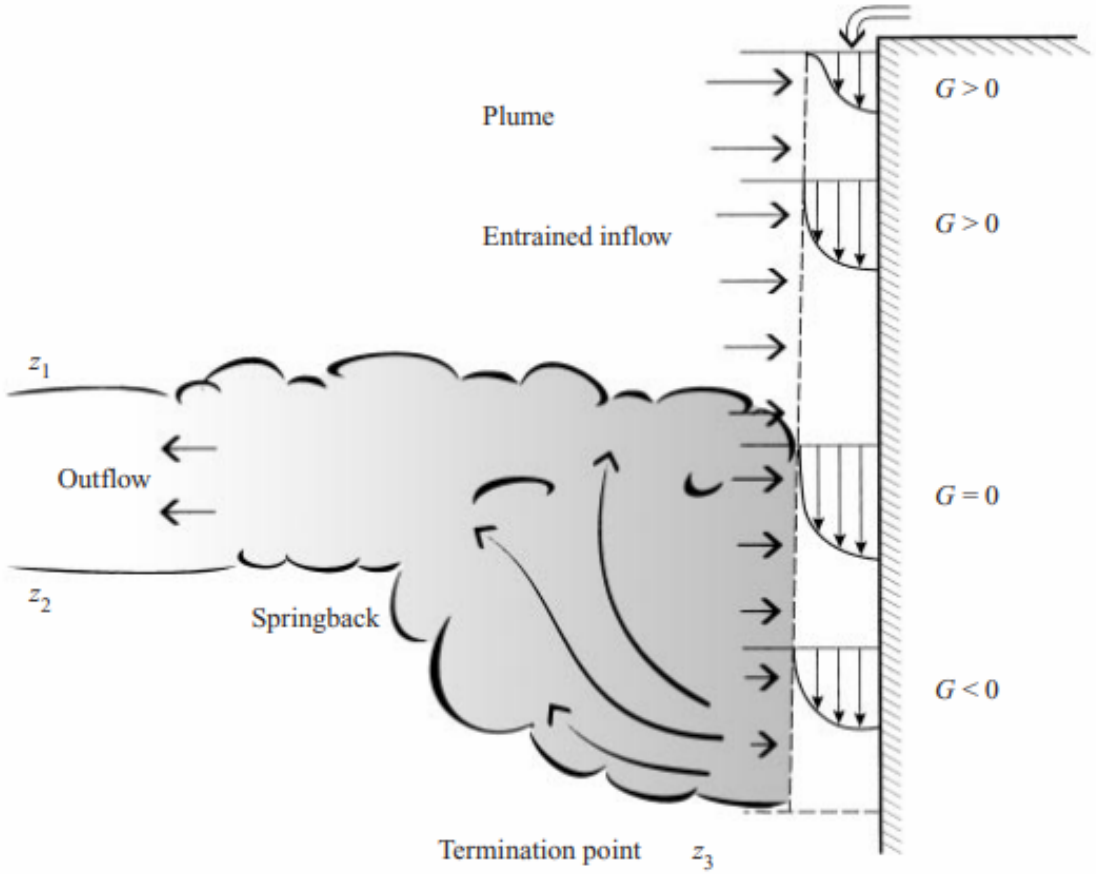

Fig. 39: Schematic diagram showing the typical behavior of a plume (or a gravity current) flowing down into a linearly stratified ambient. G denotes the buoyancy (positive downwards) of the fluid in the downflowing plume relative to the local stratified environment, and the horizontal arrows denote the entrained inflow. z_1 and z_2 denote the upper and lower levels of the net outflow, and z_3 denotes the level of maximum downward extent of the plume. Reproduced from [13].

angles (from 0° to 24°). In one of those articles [89], they improved the model for the front propagation of a gravity current flowing along a slope into a stratified ambient.

11.7 Numerical works studying a combination of slope and stratification

The rapid development of computational science and numerical methods over recent decades has provided a powerful alternative to laboratory experiments for studying gravity current dynamics. Numerical approaches offer several advantages, including scalability, lower cost, flexibility, and a non-intrusive way to explore complex flows across a wide range of conditions. However, they also have limitations: model approximations can introduce errors, numerical implementation requires care to avoid inaccuracies, and experimental validation is always necessary to ensure the results are reliable.

Bournet et al. [22] applied the standard k–ϵ turbulence model to investigate gravity currents plunging into reservoirs, a method later adopted by Choi and Garcia [39] to simulate two-dimensional (2D) dense underflows descending a slope into a homogeneous ambient. Zhang et al. [223] used a multiphase flow model to examine the flushing of trapped saline water from a bar-blocked estuary. In a related study, Birman et al. [21] numerically solved the 2D Navier–Stokes equations in a homogeneous environment to quantify the influence of slope on front velocity, revealing a maximum quasi-steady front speed at a slope angle of approximately 40°. Firoozabadi et al. [67] modeled the three-dimensional

(3D) behavior of dense underflows in straight channels using a low-Reynolds-number k–ϵ model, achieving strong agreement with experimental data.

Large eddy simulation (LES) techniques (the technique employed in the present thesis, for more details see Sect. 12.1) have also been applied to capture detailed flow features. Ooi et al. [146] conducted 2D LES of lock-exchange gravity currents, successfully reproducing key flow characteristics such as front evolution and coherent billow formation at the current head. Mahdinia et al. [115] later extended LES to a curved channel geometry, thus proving the robustness and precision of this technique.

Dai et al. [53] and Dai [49] performed 3D direct numerical simulations (DNS) of gravity currents from instantaneous releases down a slope in a homogeneous ambient, identifying variations in flow structure associated with slope angle. Härtel et al. [86] carried out DNS of lock-exchange flows, both in 3D at low Reynolds numbers (up to 750) and in 2D at higher Reynolds numbers (up to 30,000), demonstrating that 2D simulations were sufficient to reproduce the main features of front propagation.

The combined effects of ambient stratification and bottom slope were tackled by Özgökmen et al. [148], simulating large-scale oceanic gravity currents, showing that when the current detaches from the slope, its transport becomes primarily controlled by the ambient stratification. Later, the experiments of Baines [12] were reproduced in a 2D numerical simulation by Guo et al. [81]. They were able to reproduce very precisely the finding of Baines, except for some overestimation of the mixing near the neutral buoyancy point. They suggested that 3D simulations might solve the issue.

Among the numerous numerical studies, two recent articles exploring the effect of the slope on gravity currents are particularly relevant for the present study. Zúñiga et al. [226] used direct numerical simulations (DNS) to explore planar wall plumes bounded by slopes from 3° to 90°. They found that, as the slope increases, the flow transitions from a subcritical regime to a supercritical one, with entrainment and turbulence intensifying at steeper inclinations. Haddad et al. [83] employed large-eddy simulations (LES) in a non-Boussinesq context to analyze steady gravity currents along inclined planes, identifying three distinct flow regimes based on slope: transition to subcritical at low angles, persistent inertial flows at intermediate angles, and immediate plume-like behavior at steep slopes. Both studies showed that entrainment, current thickness, and momentum flux grow substantially with slope.

11.8 Penetration depth

The penetration depth of a fluid with a density difference entering a stratified ambient has historically been examined in the context of plumes. As a plume develops, entrainment of ambient fluid progressively reduces its density relative to the surroundings. At the same time, the ambient density increases (or decreases) with distance from the source due to stratification. These two effects lead to the existence of a neutral layer, where the plume density matches that of the ambient fluid. The distance from the source to this layer is called the penetration depth, D (see Fig. 40).

In 1956, Morton et al. [134] derived an expression for the penetration depth of a plume based on the conservation of volume, buoyancy, and momentum:

$$D = \frac{C B_l^{1/3}}{N}, \tag{12}$$

where D is the penetration depth, C is a constant, B_l is the buoyancy flux per unit length in the plume, and N is the magnitude of the stratification (eq. 32). The constant C has to be determined empirically and depends on the entrainment dynamics. Morton's experiments led him to: $D = 2.66 B_l^{1/3}/N -$

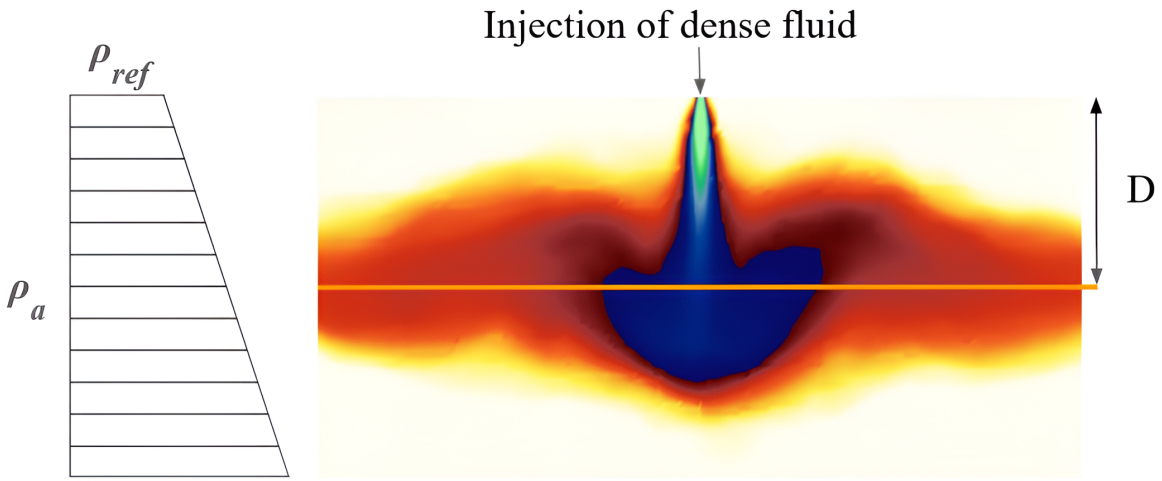

Fig. 40: Schematic of a plume penetrating a stratified ambient realized with our simulations. The stratification is schematically represented on the left. The plume reaches its neutral buoyancy level, shown by the orange line, located at a vertical distance D from the source.

4.51, which was subsequently demonstrated by Briggs [24] to reproduce data from a wide range of experimental and in-situ measurements. Caulfield and Woods [37] extended the model to consider nonlinear stratifications, while Cardoso and Woods [36] included time-dependent effects of entrainment in confined domains, finding excellent agreement with laboratory measurements.

In addition to these studies, a number of other laboratory experiments ([111],[221], [33], [187], [224]) found intrusion depth in the range: $D = 2B_l^{1/3}/N$ to $D = 4B_l^{1/3}/N$. Numerical simulations using LES have also reproduced this scaling [57, 113].

Overall, the consensus in the literature is that the penetration depth of a plume in a stratified ambient can be estimated as:

$$D = \frac{(3 \pm 1)B_l^{1/3}}{N}. \tag{13}$$

The study of the penetration depth in the case of a gravity current flowing into a stratified ambient has been less studied than the plume case. To our knowledge, only a few published papers tackle the issue. The first one is the experimental campaign of Wells and Nadarajah [214], we subsequently refer to it as **WN09**. Their goal was to understand if the scaling obtained for the penetration depth of plumes could be applied to the gravity current case.

In **WN09**, a series of 41 laboratory experiments was conducted to investigate the intrusion depth of dense gravity currents propagating into a linearly stratified ambient. A dense saline solution was continuously injected through a permeable hose onto an adjustable slope ranging from 15° to 90°, within a large Plexiglas tank containing a pre-established linear salinity stratification. The buoyancy flux of the dense current was varied between 0.5 and 350 $\mathrm{cm^3\,s^{-3}}$, while the ambient buoyancy frequency spanned 0.3 to 1.7 $\mathrm{s^{-1}}$. The resulting intrusion depth, defined as the vertical distance from the source to the center of the intrusion layer, was determined from side-view photographs.

The experimental results showed that the intrusion depth follows the scaling law:

$$D = \frac{C E_{eq}^{-1/3} B^{1/3}}{N}, \tag{14}$$

where C is a constant and $E_{eq} = \alpha/\sin(\theta)$ with α the entrainment coefficient (defined eq. 9).

A previous experimental study of the same author [215] found that the value of E_{eq} was almost constant and equal to 0.08. Applying this result, **WN09** showed that the scaling used for plumes (eq. 13) fitted their experimental points, implying that the non-dimensional penetration depth, $DN/B_l^{1/3}$, does not depend on the angle.

WN09 performed experiments with a continuous release setup. In contrast, Snow et al. [186] considered turbidity currents generated by a lock-exchange release, described in Sect. 11.6. For this configuration, the proposed scaling was:

$$D/h_0 = [2s/(\alpha S)^2]^{1/3}, \tag{15}$$

where $s = \tan(\theta)$ is the slope, h_0 is the depth of the lock-exchange source, and $S = (Nh_o/\sqrt{g'h0})^2$.

This scaling was criticized by He et al. [88] for its assumption that the front velocity was constant in the case of a lock-exchange. He et al. [88] performed a series of experiments similar to that of **WN09**, but with a lock-exchange release. He found that the scaling law $D = C(\frac{sin(\theta)}{\alpha})^{1/3}B^{1/3}/N$ fitted their experiment points well when they applied an entrainment law obtained from the experiments of [19], $\alpha = 0.0055\theta + 0.063$. Thus giving the scaling:

$$D \propto \frac{[\sin(\theta)/(0.0055\theta + 0.063)]^{1/3}B_l^{1/3}}{N}. \tag{16}$$

where C is a constant that they experimentally found equal to 1.87. A limitation of this study is that the experiments were performed only for slopes between 9° and 24°, leaving the applicability of the scaling to larger slope angles untested.

11.9 Some open questions

The dependence of the penetration depth on the slope angle for gravity currents propagating into a stratified ambient has been investigated in two key experimental studies: **WN09** [214] and He et al. [88]. **WN09** [214] employed a continuous-release apparatus, while He et al. [88] used a lock-exchange configuration. Although both studies proposed scaling laws for estimating the penetration depth as a function of buoyancy flux and ambient stratification, their formulations differ primarily in how entrainment is modeled: in **WN09**, entrainment is assumed to be independent of slope angle, whereas in He et al. [88], it explicitly depends on slope.

Differences in experimental conditions may also account for these contrasting models for the entrainment coefficients. In the **WN09** experiments, inlet velocities were relatively low due to the limited size of the apparatus, yielding Reynolds numbers below 1000. As a result, the flow may not have been fully turbulent, and mixing could have been suppressed. By contrast, the experiments of He et al. [88] reached higher Reynolds numbers (1000–3000), and turbulence was directly observed in the flow. This distinction is likely to explain the different entrainment behaviors. Both studies, however, exhibit limitations: **WN09** is constrained by the presence of laminar flow, while He et al. [88] investigated only relatively small slope angles (up to 24°).

To date, no systematic investigation has examined the penetration depth of a turbulent gravity current flowing downslope into a stratified ambient across the full range of slope angles. To address this gap, we conducted a series of Large-Eddy Simulations (LES) designed to reproduce fully turbulent gravity currents under continuous release conditions, enabling a consistent comparison across slope configurations. Our goal is to assess whether turbulence significantly affects the penetration depth. Since turbulent mixing is known to play a central role in entrainment and momentum redistribution

within gravity currents, it is reasonable to assume a turbulent regime could lead to deviations from the scaling laws proposed in **WN09**. Our numerical simulations aim to shed light on the role of turbulence in the dynamics of gravity currents in stratified environments and to potentially revise or refine existing theoretical models.

12 Numerical method

12.1 The computation code Calif^3-Isis

Simulations were performed using the Computational Fluid Dynamics (CFD) code Calif^3-Isis [82], developed by the Laboratoire de l'Incendie et des Explosions (LIE) of the Institut de Radioprotection et de Sûreté Nucléaire (IRSN). Although originally designed for fire simulations, Calif^3-Isis can be applied to a wide range of flows. In particular, it is optimized for slightly compressible flows (low Mach numbers) and reactive flows. The code has been validated against experimental data for buoyant plumes with both small [124] and large density differences with respect to the ambient fluid [174, 208], as well as for gravity currents [84].

Before examining the specific features of Calif^3-Isis, we begin with a brief overview of common numerical approaches in Computational Fluid Dynamics (CFD). At its core, CFD consists of numerically solving the Navier–Stokes equations, often using Finite Element Methods (FEM). Originally developed in the 1940s for complex engineering problems, FEM approximates solutions by discretizing the computational domain into a mesh of nodes. The governing equations are then solved iteratively at these nodes, with each time step incorporating results from the previous one. As mesh resolution increases, accuracy improves, but computational cost rises accordingly. While many numerical schemes exist for solving partial differential equations, most share the underlying principle of convergence toward fixed-point solutions.

The Navier–Stokes equations are notoriously challenging to solve; in fact, their analytical solution in the incompressible case is one of the Millennium Prize Problems of mathematics [106]. A central difficulty is the modeling of turbulence, a phenomenon characterized by complex multi-scale dynamics in both space and time (the Kolmogorov cascade). Three main approaches are commonly used to simulate turbulence: Direct Numerical Simulation (DNS), Reynolds-Averaged Navier–Stokes (RANS), and Large-Eddy Simulation (LES). Figure 41 illustrates a comparison of these three approaches for the simulation of a jet.

The Direct Numerical Simulation is conceptually the most straightforward and physically accurate, but also by far the most computationally demanding. It consists of resolving the Navier–Stokes equations across all spatial and temporal scales without any turbulence modeling. Turbulence then emerges naturally if the flow conditions (e.g., Reynolds number) permit it. The DNS is therefore considered a numerical experiment and is highly reliable. However, the prohibitive computational cost makes it infeasible for many practical applications, given the current limits of computer technology.

Reynolds-Averaged Navier–Stokes relies on time-averaged equations. The method consists of decomposing instantaneous flow quantities, such as velocity and pressure, into a mean component and a fluctuating component,

$$u_i = \overline{u_i} + u_i'. \tag{17}$$

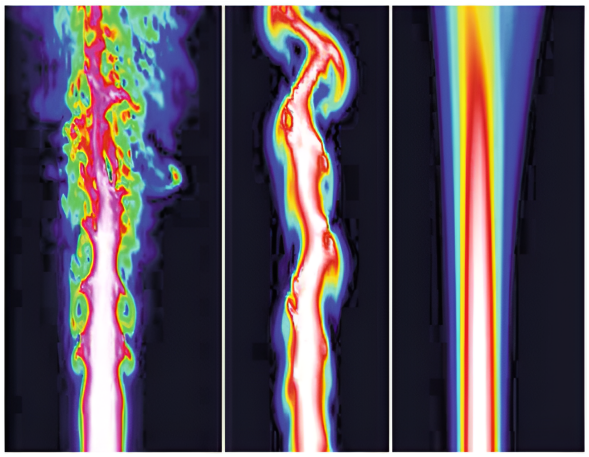

Fig. 41: DNS (left), LES (middle), and RANS (right) predictions of a turbulent jet. LES requires less computational effort than DNS, while delivering more detail than the inexpensive RANS. Reproduced from [117].

When this decomposition is introduced into the Navier–Stokes equations, additional unknown terms appear – specifically, the Reynolds stress tensor,

$$\tau_{ij} = -\overline{u_i' u_j'}. \tag{18}$$

These terms represent the influence of turbulence on the mean flow and require closure models to complete the system of equations. Turbulence models are therefore introduced, with the most widely used being the k–ϵ model. RANS provides access to the main properties of the flow using relatively coarse meshes and reduced computational cost. However, it does not capture instantaneous fluctuations of the velocity field.

Large-Eddy Simulation offers an intermediate approach between DNS and RANS. It is based on the observation that most of the kinetic energy of turbulence resides in the largest flow structures. By directly resolving these large eddies and modeling only the smaller, more universal scales, LES provides a reasonable approximation of DNS while greatly reducing computational requirements. Figure 42 illustrates the portion of the energy cascade resolved or modeled by the different approaches.

The LES framework was first introduced by Smagorinsky in 1963 for the simulation of atmospheric flows and was further developed by Deardorff in 1970. An authoritative reference books on Large-Eddy Simulation (LES) has been written by Pierre Sagaut [172] and can be consulted for further details. In this thesis, all simulations were carried out with the Calif³-Isis code using the LES approach.

Mathematically, the filter applied to separate the large and small scales in the physical space is defined by the convolution:

$$\bar{\phi}(x,t) = \int_{\Lambda} \Delta(r,x)\, \phi(x-r,t)\, dr, \tag{19}$$

where ϕ is the variable to be filtered on the domain Λ, and Δ is the filter kernel that determines the scale of the resolved structures. This operation decomposes the field ϕ into large-scale (filtered) and small-scale (residual) components:

$$\phi(x) = \bar{\phi}(x) + \phi'(x). \tag{20}$$

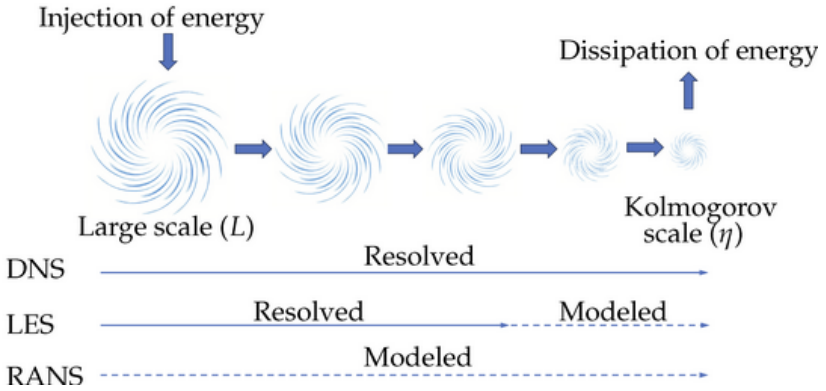

Fig. 42: Overall view of the energy cascade, from injection to dissipation of energy, and associated types of modeling. Reproduced from [168].

This decomposition is formally analogous to the Reynolds decomposition. However, it is important to note that the filtered residual ϕ' is generally non-zero. For variable-density flows, filtered quantities are often defined using Favre filtering, denoted by a tilde over the variable:

$$\tilde{\phi}(x) = \frac{\overline{\rho\phi}(x)}{\bar{\rho}(x)}. \tag{21}$$

The filtering operation is performed numerically using the computational grid. The filter kernel corresponds to a box filter defined as:

$$\Delta(r,x) = \begin{cases} \frac{1}{\Delta}, & \text{if } x - r \in \Delta \\ 0, & \text{otherwise} \end{cases} \tag{22}$$

where Δ is the computational cell volume.

In the rest of the thesis, for the sake of readability, the quantities (e.g., velocity, pressure, etc.) are all assumed Favre filtered (see eq. 21) and noted without the tilde, while the density is assumed filtered (see eq. 19) without the overline. We solve the Navier-Stokes equation in three dimensions (i=1...3) in a Cartesian coordinate system:

$$\frac{\partial \rho}{\partial t} + \frac{\partial(\rho u_i)}{\partial x_i} = 0, \tag{23}$$

$$\frac{\partial(\rho u_i)}{\partial t} + \frac{\partial(\rho u_i u_j)}{\partial x_j} = -\frac{\partial p}{\partial x_i} + \frac{\partial V_{ij}}{\partial x_j} - \frac{\partial \tau_{ij}}{\partial x_j} + \rho g_i, \tag{24}$$

where u_i is the Favre-filtered velocity, p is pressure, g_i is the gravitational acceleration. The density ρ is the filtered density of the fluid and is computed using the ideal gas law and the mass fractions of the different species in the gas mixture.

The term

$$V_{ij} = -(2/3)\frac{\partial u_k}{\partial x_k}\delta_{ij} + \mu\left(\frac{\partial u_i}{\partial x_j} + \frac{\partial u_j}{\partial x_i}\right) \tag{25}$$

is the filtered viscous strain rate tensor, where μ is the molecular dynamic viscosity calculated as a function of the individual viscosities and molar masses, as well as the corresponding mass fractions.

The term $\tau_{ij} = \overline{\rho u_i u_j} - \overline{\rho}\widetilde{u_i u_j}$ represents the sub-grid scale Reynolds stress. The latter is related to the filtered rate of strain tensor S_{ij}, using the Boussinesq approximation, as [98]:

$$\tau_{ij} = 2\mu_s \overline{S}_{ij} - \frac{2}{3}\mu_s \frac{\partial \overline{u}_i}{\partial x_i} \qquad \text{where} \qquad \overline{S}_{ij} = \frac{1}{2}\left(\frac{\partial \overline{u}_i}{\partial x_j} + \frac{\partial \overline{u}_j}{\partial x_i}\right) \tag{26}$$

and μ_s is the sub-grid turbulent viscosity, here modeled using the dynamical Smagorinsky model, as proposed by Germano et al. [73]. The reason why this model was chosen and the comparison with the other models can be found in Appendix C. By analogy to the mixing-length hypothesis, the eddy viscosity is expressed as:

$$\mu_s = \rho(C_s\Delta)^2 \mid \overline{S} \mid, \tag{27}$$

where C_s is a model parameter and not a universal constant (the default value being 0.1) and $\mid \overline{S} \mid = \sqrt{2\overline{S_{ij}} \cdot \overline{S_{ij}}}$.

The simulations involve several species k to obtain different densities, whose mass fraction y_k is calculated through the species transport equation:

$$\frac{\partial(\rho y_k)}{\partial t} + \frac{\partial(\rho y_k u_i)}{\partial x_i} = \frac{\partial}{\partial x_i}\left(\rho D_m \frac{\partial y_k}{\partial x_i} + \frac{\mu_s}{S_c}\frac{\partial y_k}{\partial x_i}\right), \tag{28}$$

where y_k is the mass fraction of the *k-th* component of the mixture, D_m is the molecular diffusivity of the mixture, μ_s is the subgrid turbulent dynamic viscosity, and S_c is the subgrid turbulent Schmidt number considered here equal to 0.7. A passive scalar following eq. 28 was also added to the simulation. Its concentration is normalized to 1 in the inlet flow and allows for easier visualizations.

At the source, to trigger the transition to turbulence, the inlet flow has been perturbed with the method presented by Jarrin et al. [99]. The latter has been conceived to reproduce inflow conditions in wall-bounded flow (even characterized by complex geometries) with prescribed first- and second-order one-point statistics, characteristic length, and time scales. In this approach, turbulence is generated by superimposing a set of synthetic eddies—coherent structures defined by spatial shape functions—onto the mean velocity field at the inlet. These eddies are convected through the inflow plane and continuously regenerated to maintain statistical stationarity, resulting in realistic spatial and temporal correlations. The method effectively provides a physically consistent turbulent signal without requiring a precursor simulation, making it particularly suited for LES of spatially developing flows.

We employ a staggered Cartesian mesh with scalar quantities defined at cell centers and velocity components located on the cell faces, following a marker-and-cell (MAC) type finite-volume formulation. Temporal discretization is based on a fractional-step procedure, enabling pressure correction at each timestep. An implicit Crank–Nicolson scheme is adopted, allowing Courant–Friedrichs–Lewy (CFL) numbers close to unity to be maintained throughout the simulation.

The boundary conditions are of solid wall-type for the inclined wall and the top wall, and the left wall is an outlet. This outlet-type boundary condition is based on the control of kinetic energy. It distinguishes between the flow that leaves the domain and the flow that enters it [28–30]. This is numerically imposed in the form of an outlet condition. The outlet condition is imposed by a momentum conservation:

$$\tau.n - p.n = -p_{ext}.n. \tag{29}$$

The wall-type condition (different from the no-slip condition) was developed by Werner and Wengle [216]. It imposes a boundary layer profile of the form:

$$u^+(z) = \begin{cases} z^+ & \text{if } z^+ \leq 11.8, \\ 8.3(z^+)^{1/7}, & \text{otherwise} \end{cases} \tag{30}$$

where $u^+(z)$ is the velocity profile close to the wall and $z^+ = \frac{\rho}{\mu} u_\tau z$ is the dimensional thickness of the layer with u_τ the friction velocity. The choice of the boundary condition and its effect is discussed in Appendix C.

12.2 Studied configuration

The configuration studied in this work is schematically illustrated in Fig. 43. A gravity current is generated by a localized source of buoyancy per unit length B_l, located at a distance L from the edge of an inclined wall located in $z = 0$. B_l is defined as:

$$B_l = gwl\frac{\Delta\rho}{\rho_{a,0}}, \tag{31}$$

where w is the imposed velocity at the source along the z^* axis (the component along the other axis is equal to zero), l is the width of the source (equal to 0.242 m), and $\frac{\Delta\rho}{\rho_{a,0}}$ is the relative density between the flux at the source and the upper layer of the ambient fluid. In all the simulations, we kept the source velocity constant, $w = 0.5$ m/s.

The flow develops along a planar inclined surface with a slope angle θ, defined as the angle between the horizontal and the slope. This means that 0° refers to a horizontal wall and 90° to a vertical wall.

Two coordinate systems are used to describe the geometry: the system $\{x,y,z\}$, where x is the horizontal axis, y the transverse horizontal axis, and z the vertical axis oriented downward (aligned with gravity), with the origin at the top-left corner of the domain; and a slope-aligned system $\{x^*,y^*,z^*\}$, obtained by rotating the global system by an angle θ about the y-axis, such that x^* is aligned with the slope.

The ambient fluid is linearly stratified, characterized by a constant Brunt-Väisälä frequency:

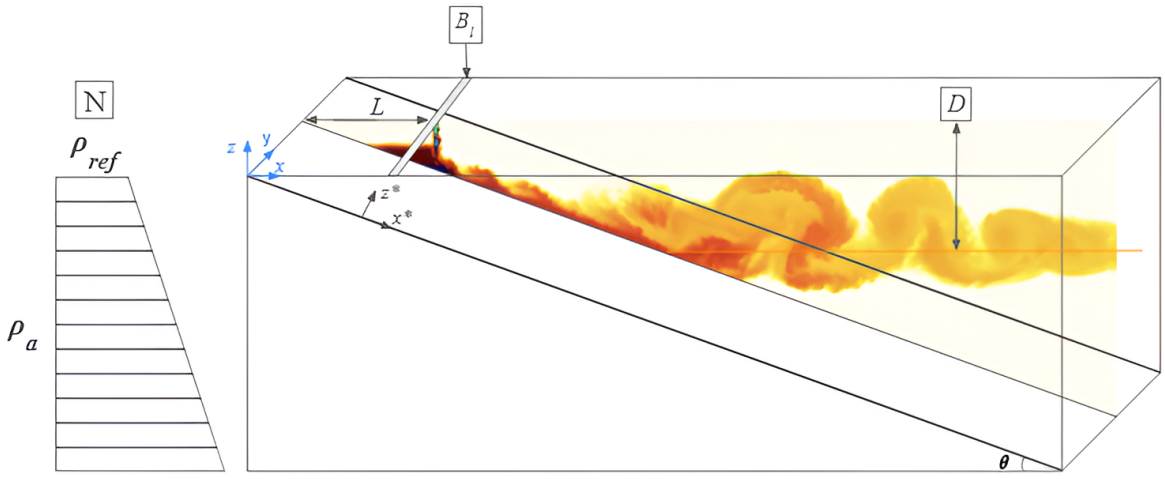

Fig. 43: Schematic of the studied geometry. A dense fluid flows downslope into a stratified ambient fluid along an inclined wall at an angle θ. The stratification is schematically represented on the left. The color scale indicates the concentration of a passive tracer, with darker shades corresponding to higher concentrations. The current eventually reaches its neutral buoyancy level, shown by the red line, located at a vertical distance D from the source. Image obtained using the author's simulations.

$$N = \sqrt{\frac{-g}{\rho_{a,0}} \frac{\partial \rho_a(z)}{\partial z}} \tag{32}$$

and a reference density $\rho_{a,0}$, that is the density of the fluid in the plane $z = 0$. The initial density $\rho_a(z)$ in the fluid follows this equation:

$$\rho_a(z) = \rho_{a,0} - N^2 \cdot \frac{\rho_{a,0}}{g} \cdot z, \tag{33}$$

where g is the acceleration of gravity.

In our configuration, the injected flow starts as a plume before hitting the wall and developing as a gravity current (see Fig. 44). Several types of plumes are distinguished by the flux-balance parameter [206]:

$$\Gamma(z) = \frac{5}{8\alpha_p} Ri(z), \tag{34}$$

where $\alpha_p = 0.12$ is a reference far-field value for the pure plumes entrainment coefficient.

In the far field, any turbulent buoyant release tends toward the so-called pure plume equilibrium, characterized by $Ri_p = 8\alpha_p/5$, regardless of its initial source conditions [206]. By definition, a pure plume corresponds to $\Gamma = 1$. This serves as a reference for distinguishing between different regimes: forced plumes, which possess excess momentum relative to pure plume conditions ($0 < \Gamma < 1$), and lazy plumes, which are momentum-deficient ($\Gamma > 1$). In our simulation, we choose to use a lazy plume. In this condition, the dynamic of the flow depends on the buoyancy forces and not on the initial velocity.

As the fluid is stratified, the gravity current propagates downslope and mixes with the ambient fluid until it reaches a level of neutral buoyancy, where its density matches that of the ambient fluid. The intrusion depth D is defined as the vertical distance between the source and the layer at which the current stops. In practice, it is measured using the vertical intrusion, with its average depth being

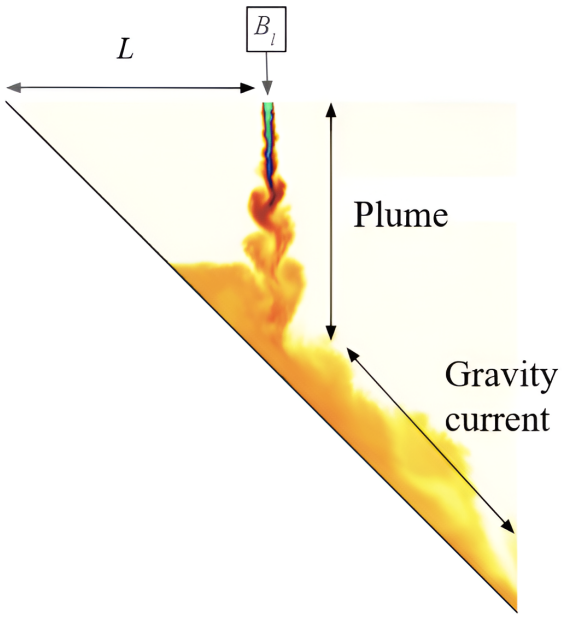

Fig. 44: Schematic of the flow evolution: the dense fluid forms a descending plume before impacting the wall and transitioning into a gravity current.

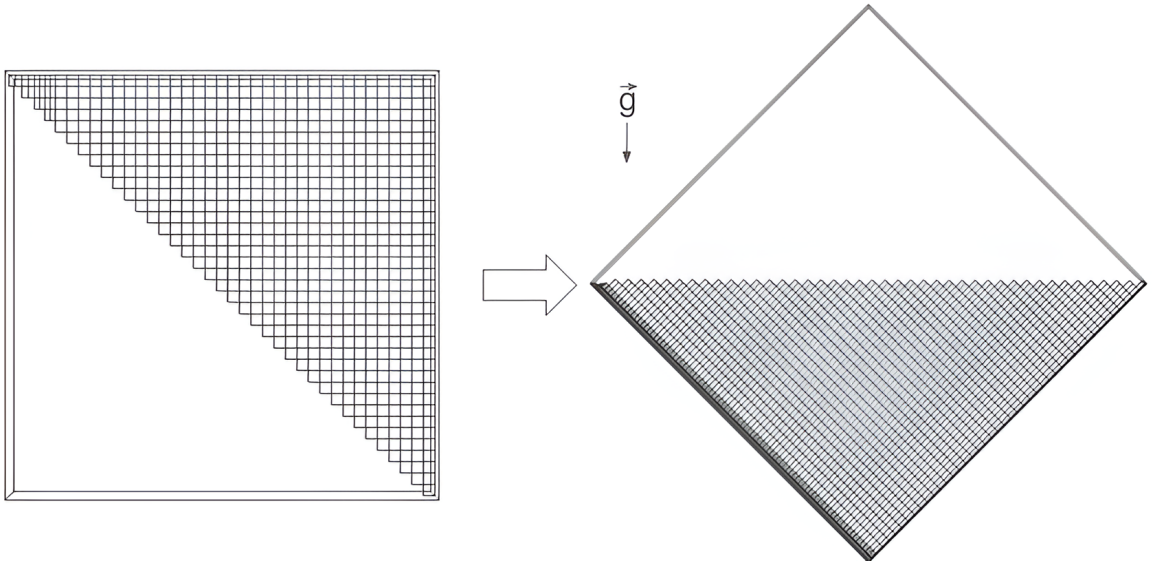

Fig. 45: Transition from the naive mesh with a slope represented as a staircase (left) to the final mesh with a smooth slope (right).

D. This is different from the termination point, which is the deepest point on the wall attained by the current. This point is usually deeper than D due to the inertia of the flow. The current goes a little deeper on the wall but then flows back up to its local neutral layer (see Figure 39).

The dynamics of this problem involve three governing parameters: (i) the depth of intrusion D, (ii) the buoyancy flux at the source B_l, and (iii) the Brunt–Väisälä frequency N of the ambient fluid. The velocity at the source is not important because we are in a lazy plume context. According to the Buckingham-π theorem, since these three variables span two fundamental physical dimensions (length and time), a single nondimensional parameter can be constructed. This dimensionless group, denoted D_a, is defined by [214] and [186] as:

$$D_a = \frac{DN}{B_l^{1/3}}. \tag{35}$$

We checked that this relationship was verified in our simulations in Appendix D.

12.3 Mesh

The computational domain is a triangular prism, with the hypotenuse representing the inclined wall along which the gravity current propagates (see Figure 43). The domain width was fixed at $6r_s$, where r_s is half the source opening ($r_s = 0.121$ m). The streamwise length (L_x see Figure 46) was set to 30 m in most cases and extended to 50 m for the smallest angles (5° and 10°) to allow sufficient downslope propagation. The vertical extent of the domain was fixed at 5 m.

In the Calif^3-Isis code, inclined walls are generated by subtracting a triangular section from a rectangular box. This method, however, produces a staircase-like slope whose step size depends on the grid resolution. To avoid this artifact, the geometry was inverted: the smooth upper wall was used to represent the slope, while the stair-like wall was shifted to the top of the domain (see Figure 45). The gravity vector was then rotated, and the density source was placed along the stair-like wall. This ensured that the lower boundary became a smooth slope, providing a more faithful representation of the flow dynamics.

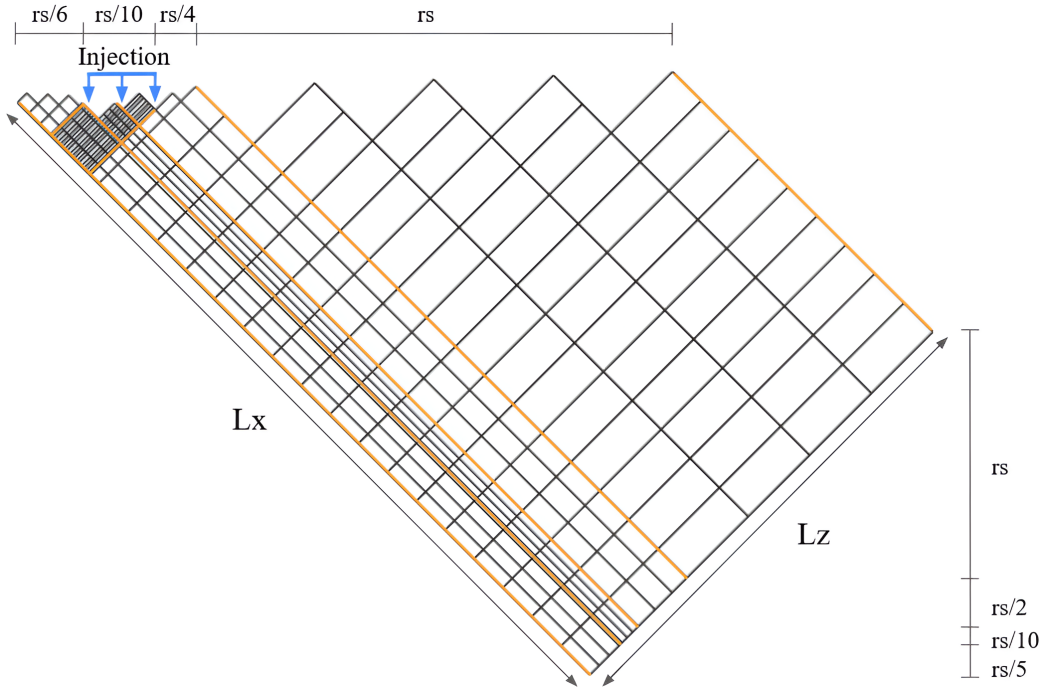

Fig. 46: Schematic of the computational mesh showing the different refinement zones.

The final mesh configuration is shown in Figure 46. The grid is Cartesian, with variable refinement depending on proximity to the slope and the source. Close to the slope, the vertical resolution is fine ($r_s/6$) and gradually stretches to r_s away from the wall. Around the injection region, the mesh is further refined to $r_s/10$ in both the x and z directions, while in the streamwise direction outside this region, the grid spacing is uniform at $r_s/2$. The overall domain dimensions in the streamwise, spanwise, and vertical directions are denoted by L_x, L_y, and L_z, respectively (see figure 46).

A mesh sensitivity analysis was carried out to determine the appropriate grid resolution. For a representative case (θ=20°, B_l=0.063 m^3/s^3, N^2=0.02 Hz^2), simulations were performed with several mesh sizes. The penetration depth of the current and its entrainment coefficient increased as the grid was refined and converged asymptotically to a stable value. The results of this sensitivity study are presented in Appendix B.

12.4 Post processing

The post-treatment and visualization of the data were done with the software Fieldview from Tecplot and Python.

To visualize the gravity current more clearly, a passive tracer was added to the flow at the inlet (Figure 47). This tracer has no mass and does not influence the dynamics of the flow; the evolution of its concentration is governed by eq. 28. Because the tracer is purely advected, it provides a simple and effective way to identify the extent of the current and, in particular, to measure its depth.

Our analysis focuses on time-averaged quantities in the quasi-steady phase of the current. As explained in Sect. 11.1, for a continuous release, the flow at a given location first undergoes a transient stage before reaching a quasi-steady regime. In this regime, the mean quantities vary little in time, although turbulent fluctuations cause fluctuations of up to about 10%. To compute the averages, the velocity and tracer fields were averaged over the time interval from $t_{end}/5$ to t_{end}, where t_{end} denotes the total simulation time. This procedure excludes the initial transient phase and ensures that only the

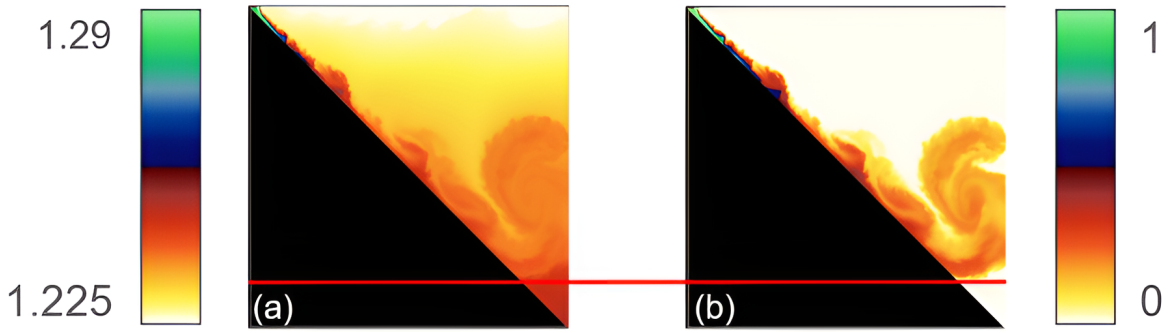

Fig. 47: Comparison for the same simulation of (a) density field ρ (in kg/m^3) and (b) passive tracer field (normalized to 1 at the inlet). The red line indicates the z position of the termination point.

statistically steady portion of the flow is considered. The quasi-steady regime is established once the flow front has ceased advancing and reached its final position. In all cases, this position was attained several seconds before $t_{end}/5$, leaving a sufficiently long time window to compute reliable averages. The choice of this averaging interval was further validated by longer simulations, which confirmed that the flow had already reached a quasi-steady state by $t_{end}/5$.

For the entrainment analysis (see Sect. 11.5), we also need to calculate the flow rate Q and specific momentum flux M of the current. To perform these integrations, we introduce the characteristic thickness of the current, denoted by h (see Figure 29). The thickness $h(x)$ is defined as the height above the boundary where the streamwise velocity decreases to 10% of its maximum value at that location. The 10% threshold is a value we found to work well for our data. A sensitivity analysis confirmed that using smaller thresholds, down to 1%, produced nearly identical results. Using a 10% threshold instead of 1% helps eliminate velocity fluctuations at the interface between the current and the ambient fluid. We then calculate Q and M defined in eq. 7 integrating between 0 and $h(x^*)$.

Figure 49 illustrates the procedure: panel (a) shows the mean velocity field $\overline{u}$, while panel (b) displays the same field after applying the threshold. The black regions correspond to excluded points, leaving only the part of the flow associated with the gravity current. The integrals are then computed at prescribed x^* locations using the CFD software.

12.5 Runs

A series of numerical simulations was conducted to examine how the slope angle influences the penetration depth of a gravity current propagating into a stratified ambient. As introduced in Eq. 35,

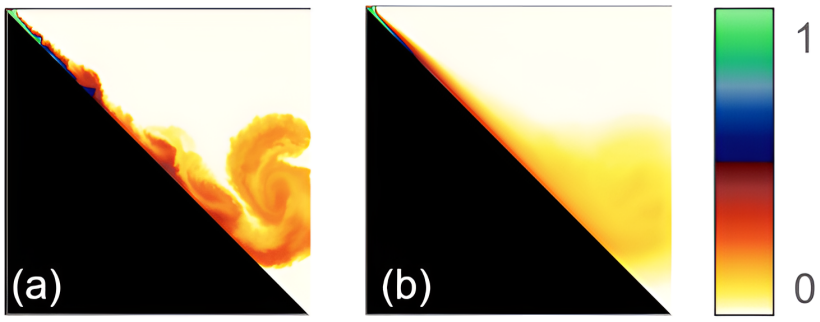

Fig. 48: Comparison for the same simulation of (a) an instantaneous field of concentration of the tracer, (b) the time-averaged field of concentration of the tracer.

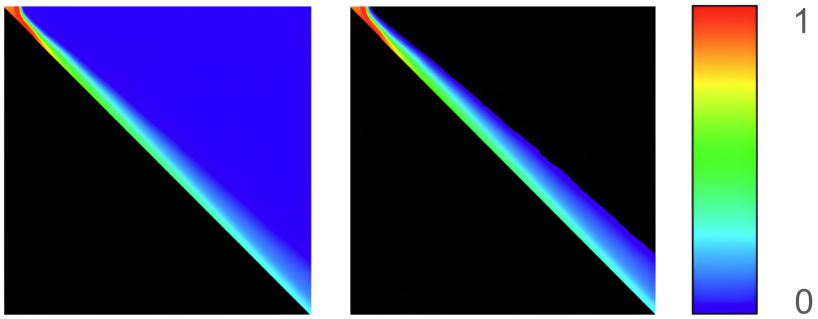

Fig. 49: Application of the threshold function to the flow field. The upper panel shows the entire flow field, while the lower panel highlights only the regions retained by the threshold function (in color). The black areas correspond to the neglected portions of the flow.

the nondimensional penetration depth D_a was defined to be independent of the buoyancy flux B_l and the stratification N, depending only on the slope angle θ. In practice, this means that for a given θ, different combinations of (B_l, N) yield penetration depths D that collapse onto the same value of D_a. Consequently, for each slope angle, B_l and N can be adjusted as convenient to simplify or optimize the simulations without affecting the nondimensional results.

Different source positions were considered (see Table 7), and for each configuration, simulations were performed over a range of slope angles: starting from 5° and then every 10° up to 90°.

All simulations were performed with a constant density difference between the injected fluid and the ambient upper layer (ρ_a), chosen sufficiently small to ensure Boussinesq conditions. Specifically, the injection density was set to $\rho_{inj} = 1.053\rho_{a,0}$. This means that for a specific opening of the source, B_l is a constant. Different stratifications N^2 were used depending on the angle so that the current would flow along the slope for about $100r_s$ to $200r_s$.

Two sets of simulations were carried out: (i) to evaluate the penetration depth (cases 1 to 4) and (ii) to quantify the entrainment coefficient (cases 5 to 8). The entrainment simulations required longer integration times in order to ensure that the flow reached a quasi-stationary regime. The total simulation time (t_{end}) was 300 s for cases 1–4 and 1000 s for cases 5–8.

Table 7: Details of the simulations performed: case name, opening of the source, distance of the source to the wall, stratification intensity, domain size, inlet Richardson number, purpose of the simulation series. Each case is a series of 10 simulations performed over a range of slope angles: starting from 5° and then every 10° up to 90°. For the cases in which the stratification changes with the angle, the stratification used for 5° and 90° is given. The domain size is the one used for angles ranging from 20° to 90°, for 5° and 10°; a longer domain ($L_x = 50$) was used.

Case	Source opening	L	N^2	$L_x \times L_y \times L_z$	Ri	Purpose
1	$2r_s$	$5r_s$	0.1-0.01	$30 \times 0.726 \times 10$	0.41	D_a analysis LES
2	$2r_s$	$25r_s$	0.1-0.01	$30 \times 0.726 \times 10$	0.41	D_a analysis LES
3	$2r_s$	$45r_s$	0.1-0.01	$30 \times 0.726 \times 10$	0.41	D_a analysis LES
4	$2r_s/24$	$r_s/5$	0.5-0.3	$0.3 \times 0.03 \times 0.05$	5	D_a analysis laminar
5	$2r_s$	$5r_s$	0	$30 \times 0.726 \times 5$	0.41	Entrainment analysis LES
6	$2r_s$	$5r_s$	0.001	$30 \times 0.726 \times 5$	0.41	Entrainment analysis LES
7	$2r_s$	$5r_s$	0.01	$30 \times 0.726 \times 5$	0.41	Entrainment analysis LES
8	$2r_s$	$5r_s$	0.02	$30 \times 0.726 \times 5$	0.41	Entrainment analysis LES

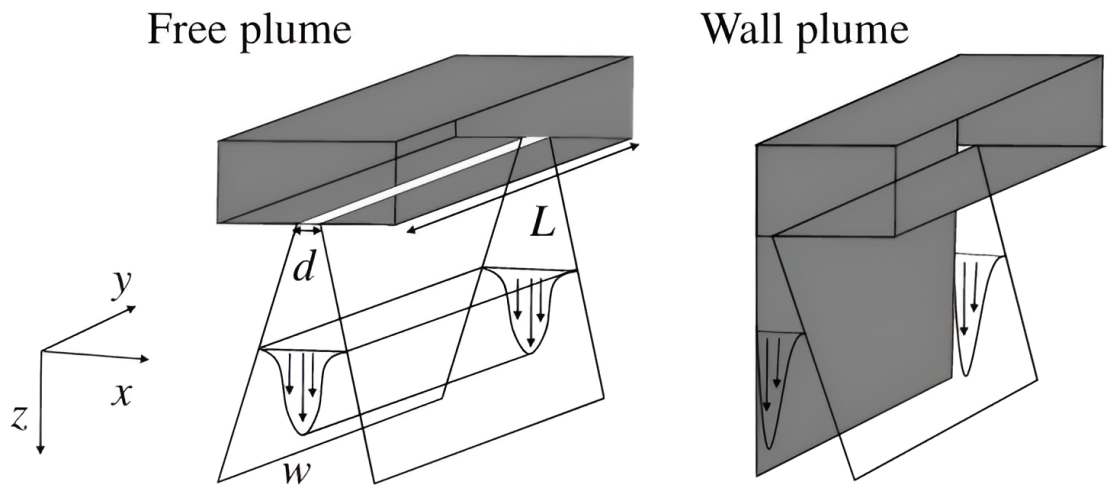

Fig. 50: The experimental setup used by Parker et al. [154].

13 Validation of the simulations

We validated our code by reproducing the experiments of Parker et al. [154], aimed at measuring the entrainment in a plume close to and far from a wall. For this, they used a tank full of a saline solution in which a dense sodium nitrate solution was injected. The dense solution was pumped inside the tank from a line source at its top (see Figure 51), generating a plume whose velocity and buoyancy were simultaneously measured. The velocity measurement was performed with the PIV (Particle Image Velocimetry) technique, and the buoyancy measurement was performed using the Laser-Induced Fluorescence (LIF) technique. From these measurements, the entrainment in the plume was estimated. It was found that the free plume (far from the wall) exhibited an entrainment coefficient of 0.135, and the plume flowing along the wall showed an entrainment coefficient of 0.076.

To assess whether our numerical framework could reproduce the experimental results of Parker et al. [154], we performed two sets of simulations corresponding to their wall plume and free plume configurations. Rather than reproducing Parker's setup exactly – with identical initial conditions and domain dimensions – we adopted configurations consistent with the broader set of simulations presented in this study. Specifically, we employed larger domain sizes and higher inlet velocities than those used in Parker's experiments.

This choice was motivated by two main considerations. First, the quantities of interest for comparison – namely, entrainment rate, velocity field, and buoyancy profiles within the near-self-similar region (sufficiently far from the source) – are known to be largely insensitive to initial conditions [173]. Second, employing the same mesh strategy and inflow conditions as in the rest of our simulations enabled us to validate not only the overall predictive capability of Calif^3-Isis but also the specific implementation developed for this study.

The computational domains consisted of two rectangular parallelepipeds. For the wall plume configuration, the domain dimensions were $L_x = 5$ m, $L_y = 0.6$ m, and $L_z = 20$ m. For the free plume configuration, the dimensions were $L_x = 10$ m, $L_y = 0.6$ m, and $L_z = 20$ m. The source opening had a diameter of $2r_s = 0.121$ m (with $r_s = 0.121$ m), and the inflow velocity was set to 0.5 m/s. For comparison, Parker's experimental setup used much smaller dimensions, 1.2 m x 0.15 m x 0.4 m, and a source opening of only 1 mm.

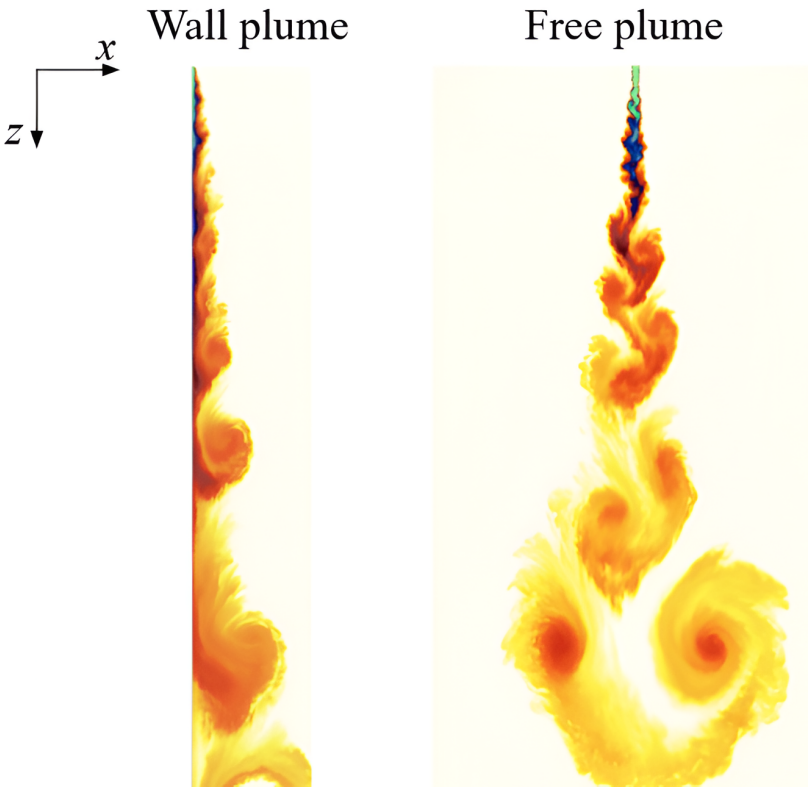

Fig. 51: The simulations reproducing the experiments of Parker et al. [154].

Figure 51 presents a visual overview of the simulated flow, and Figure 52 compares the corresponding nondimensional velocity and buoyancy profiles with the experimental measurements of Parker et al. [154]. The profiles correspond to the time-averaged vertical velocity $\overline{w}$, the time-averaged longitudinal velocity $\overline{u}$, and the time-averaged buoyancy $\overline{b} = g\,\overline{\Delta\rho}/\rho_a$. Each quantity is normalized by its maximum value ($\overline{w}_m$, $\overline{u}_m$, $\overline{b}_m$). The horizontal axis is nondimensionalized by the distance z from the source at which the profiles were extracted. The close agreement between the two demonstrates that the simulations successfully reproduce the key velocity and buoyancy characteristics observed in the experiments.

Another comparison between the experiments and the simulations concerned the values of the entrainment coefficient. In Parker's study, the entrainment coefficient was defined as:

$$\alpha = \frac{dh}{dz}, \tag{36}$$

where h is the thickness of the plume in the wall plume and half the thickness of the plume for the free case. Estimating these quantities from our simulations, we found the same values as Parker. Namely, 0.076 in the wall case and 0.135 in the free case.

We conclude from these results that the code Calif^3-Isis and, in particular, our numerical configuration are capable of simulating plumes with a high degree of accuracy.

14 Results

We present the main findings obtained from our numerical simulations. We begin by describing the typical behavior of a gravity current in our setup and examining how ambient stratification influences

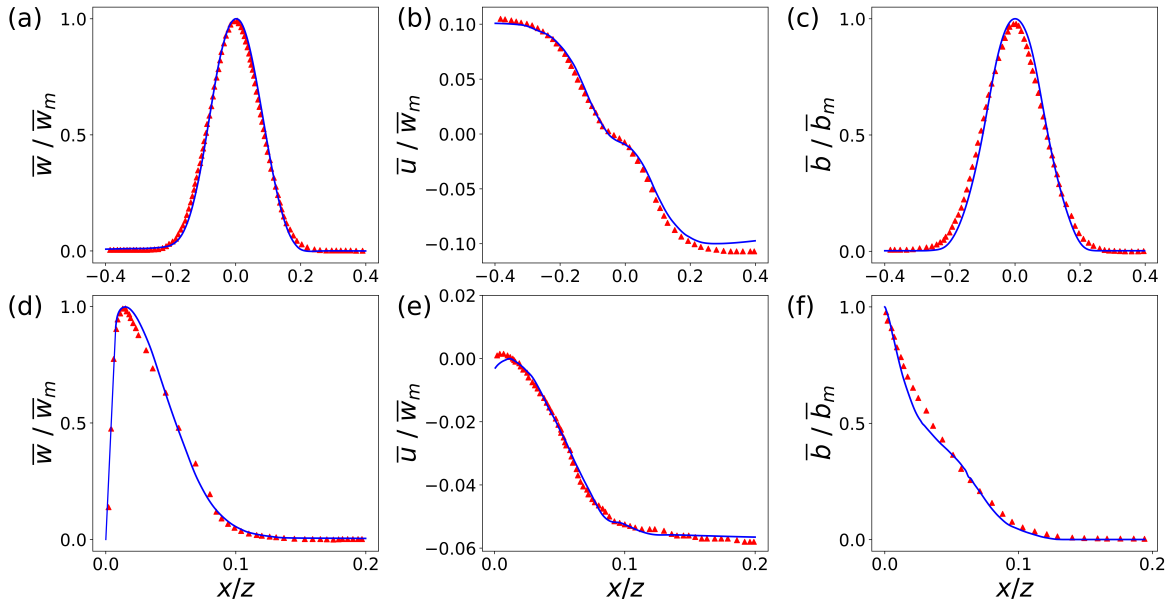

Fig. 52: Comparison between the experiments of Parker et al. [154] (the red triangles) and our numerical simulations of Parker's setup (blue line). Time-averaged vertical and horizontal velocity profiles, together with buoyancy profiles, all normalized by their respective maximum values. Panels (a–c) show results for the free plume, while panels (d–f) correspond to the wall plume.

its evolution. This is followed by an introduction and illustration of the concept of near-self-similarity [173]. We then analyze the entrainment coefficient, focusing on its dependence on slope angle and Richardson number, as well as its connection to self-similar behavior. To gain deeper insight into the entrainment process, we also present a decomposition of the entrainment, which provides a more refined understanding of its dynamics.

The second part of this section addresses the penetration depth, which constitutes the central result of this study. We started by reproducing numerically the experiments of **WN09** in the laminar regime, showing good agreement with their results. Building on this, we present our original contributions: simulations exploring the dependence of penetration depth on slope angle in the turbulent regime. The simulations showed that, unlike in the laminar case, the penetration depth in turbulent flows varies with slope angle, a behavior we analyze in terms of the underlying physical mechanisms. Finally, we propose a new scaling law for the prediction of penetration depth in turbulent flows.

14.1 Near-self-similar regime

The starting point of our analysis is a description of the flows observed in the simulations. For a homogeneous environment, a gravity current flowing along a slope typically has a raised head in the front, followed by a shallower steady current (as seen in Sect. 11.1). This behavior is reproduced in Figure 53, which presents simulation results obtained with the following parameters: θ=45°, B_l=0.063 m^3/s^3, and N^2=0.02 Hz^2 at different times. The gravity current, characterized by its raised head, propagates downslope (panels (a) and (b)) until it reaches the outlet (panel (c)). Beyond this point, only the shallower trailing portion of the current remains visible within the observation window (panel (d)).

In a stratified environment, the evolution of the current differs significantly. Initially, its behavior resembles that of the unstratified case, as illustrated by the similarity between panels (e) and (f) and

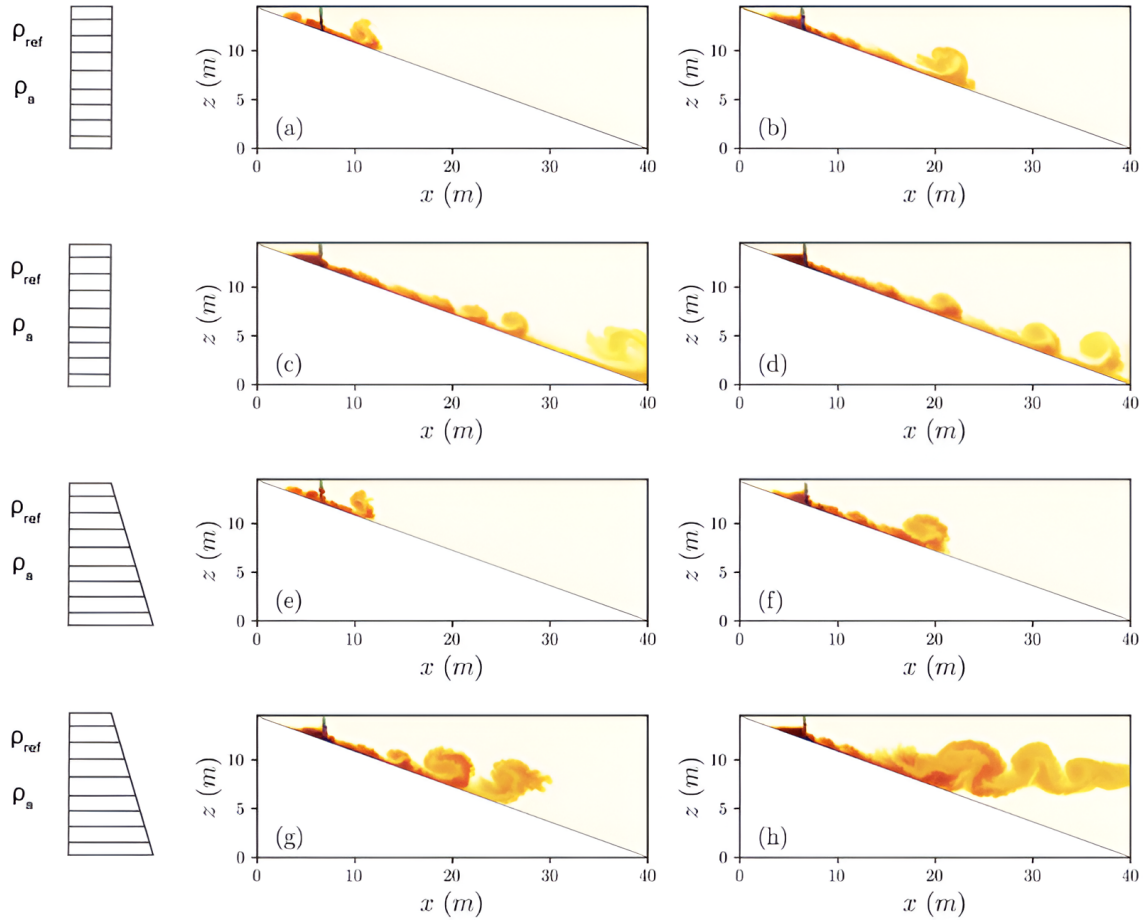

Fig. 53: Evolution over time of a gravity current for θ=20°, B_l=0.063 m^3/s^3, and an opening size of the source of $2 \cdot r_s$. The four upper panels (**(a)** to **(d)**) refer to an unstratified case. The four lower panels (**(e)** to **(h)**) describe the current in a stratified fluid with N^2=0.02 Hz^2. The ambient stratification is schematically symbolized on the left. **(a)** and **(e)** t= 20 s, **(b)** and **(f)** t= 48 s, **(c)** and **(g)** t= 80 s, **(d)** and **(h)** t= 144 s.

panels (a) and (b). However, as the current approaches its neutral-buoyancy level (i.e., the stratified layer with density equal to that of the current), it begins to thicken (panels (f) and (g)). Ultimately, the downslope propagation ceases, and the current transitions to a predominantly horizontal motion, forming an intrusion (panel (h)).

The contrasting behaviors observed in unstratified and stratified environments highlight the role of background density structure in shaping gravity current dynamics. Equally important, however, is the distinction between the near-source adjustment region and the far-field evolution of the flow. Close to the source, the current retains a strong imprint of inlet conditions such as volume and momentum flux, but these effects diminish farther downslope. Beyond this adjustment zone, the current evolves under the combined influences of buoyancy, inertia, and wall-bounded turbulence toward a regime of near-self-similarity. In this regime, the large-scale characteristics are governed primarily by the imposed buoyancy flux and the bed slope, largely independent of the source details. The current thickness continues to increase with distance, while the velocity scale approaches a constant value. As a result, integral parameters such as the Richardson number and entrainment coefficient are nearly constant and depend only on the slope [173].

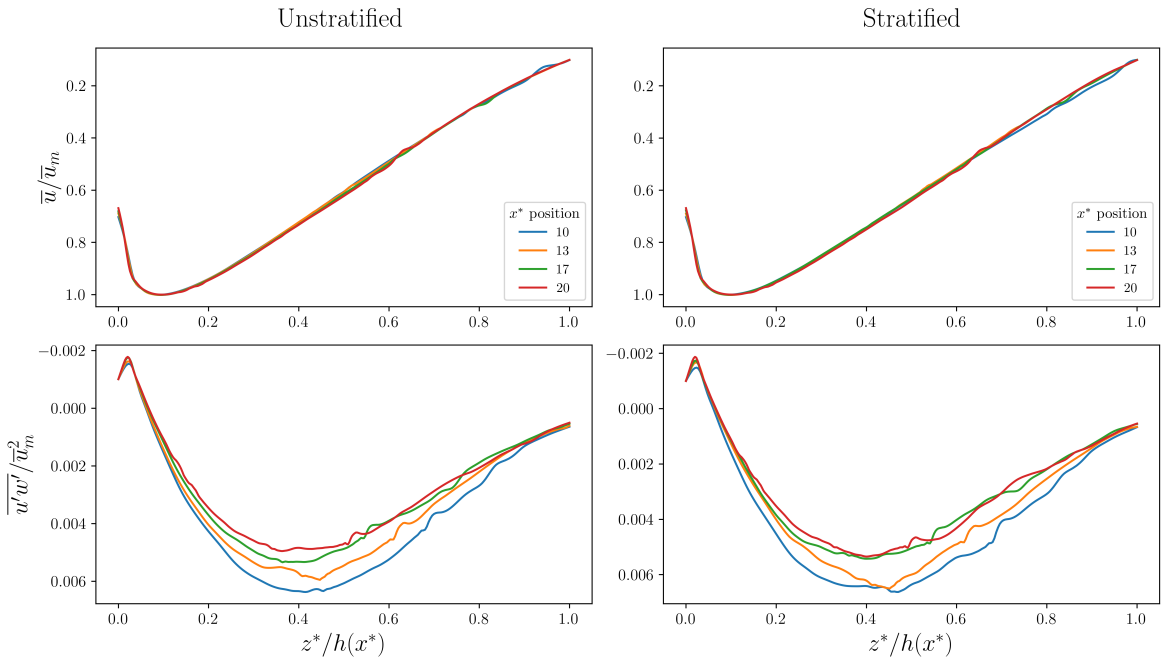

Fig. 54: Time-averaged, scaled velocity and turbulence profiles. The figure is organized in two columns showing the unstratified (left) and stratified (right) cases, with two rows displaying the mean streamwise velocity $\overline{u}$ and Reynolds shear stress $\overline{u'w'}$. Each color corresponds to a streamwise position x^* along the slope. The legend is shown on the $\overline{u}$ plot and applies to all panels.

Unlike unbounded free shear flows – where full self-similarity can emerge with Gaussian-like velocity and buoyancy distributions, together with complete independence from initial conditions [72] – wall-bounded gravity currents exhibit a more complex structure. The presence of the wall introduces a distinction between an inner wall-dominated region and an outer free-shear region. The outer layer grows approximately linearly with distance to the source, whereas the wall-dominated layer grows more slowly and eventually approaches a nearly constant thickness. This multilayer configuration prevents exact self-similarity. Nevertheless, because the influence of the near-wall region diminishes downstream, the current asymptotically approaches a near-self-similar state [207].

This is illustrated in Figure 54, which presents velocity-related profiles from simulation results obtained with the following parameters: θ=40°, B_l=0.063 m^3/s^3. The Figure shows the vertical (as a function of z^*) profiles of time-averaged velocity ($\overline{u}$) and Reynolds stress ($\overline{u'w'}$) at different x^*. Here, u denotes the velocity component along the x^* axis and w the component along the z^* axis. The mean velocity is normalized by its maximum value in the direction normal to the slope z^*, here defined as $\overline{u}_m$. Profiles are displayed from the wall up to the local thickness of the current $h(x^*)$. The vertical coordinate is normalized by $h(x^*)$. Profiles are taken at regular intervals, starting from 10 to 20 m to the point where the current hits the wall. The different profiles are shown for an unstratified ambient (left column) and a stratified ambient with $N^2 = 0.001$ Hz^2 (right column).

All normalized time-averaged velocity profiles, $\overline{u}/\overline{u}_m$, collapse onto a single curve in both stratified and unstratified conditions, clearly demonstrating self-similarity. For the normalized time-averaged Reynolds stress $\overline{u'w'}/\overline{u}_m^2$ the profiles exhibit very similar shapes but do not collapse perfectly, as their peak magnitudes slightly vary. In this study, however, we focus primarily on the mean quantities. For these, the comparison between stratified and unstratified cases shows no significant difference: the

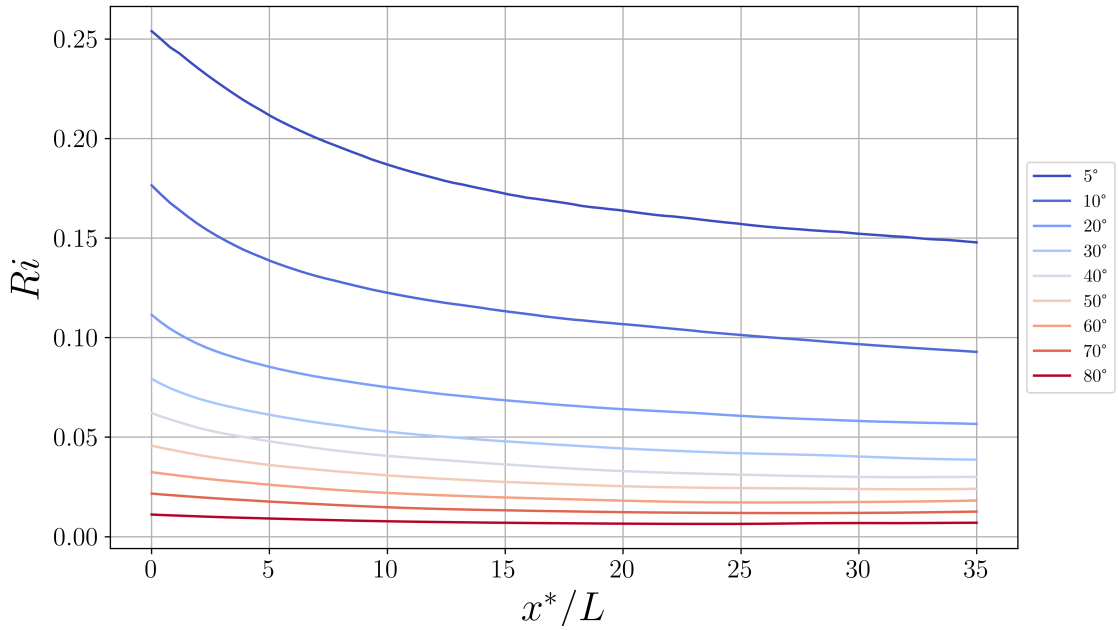

Fig. 55: Evolution of the Richardson number with the distance from the point where the current hits the wall. The Richardson number eventually becomes constant as the current reaches its self-similar state.

near-self-similar state emerges in both scenarios, starting at 10 m from the point where the current hits the wall.

As the velocity scale u_m approaches a constant, other quantities that depend on velocity integrals also asymptotically tend toward constant values. Figure 55 shows the Richardson number as a function of distance from the point where the current reaches the wall, for different slope angles. The Richardson numbers were obtained from simulations with the same buoyancy flux as in Figure 54. The figure illustrates the convergence of the Richardson numbers to constant values as the current develops downstream and attains a near-self-similar state. Their asymptotic values depend on the slope angle and the background stratification, but they remain independent of the source characteristics. Since the entrainment coefficient α depends on the Richardson number, it similarly converges to a constant value, as shown in Figure 56, which presents the entrainment coefficient for the same simulations as Figure 55. This will be further examined in the section on entrainment (Sect. 14.2). Our observation of a near-self-similar regime is consistent with previous experimental studies [154, 176], which likewise identified self-similar regimes in gravity currents.

14.2 Entrainment analysis

To study the entrainment, long simulations (t_{end}=1000 s) were performed to achieve a statistically quasi-stationary regime as explained in Sect. 12.5. This corresponds to cases 5 to 8 on Table 7. The quasi-stationary regime should not be confused with the near-self-similar state described in the previous Sect. 14.1. The quasi-stationary regime is established over time, whereas the near-self-similar state is reached at a certain distance from the source.

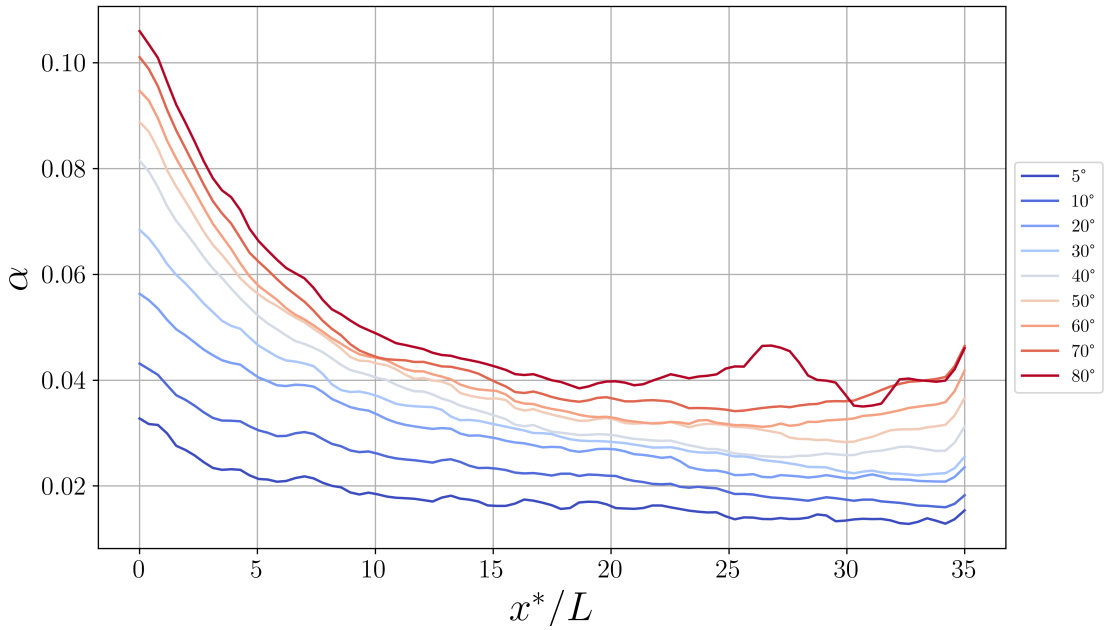

Fig. 56: Evolution of the entrainment coefficient with the distance from the point where the current hits the wall. The entrainment eventually becomes constant as the current reaches its self-similar state.

We start by presenting the results of Case 5, which corresponds to an unstratified configuration. Simulations including stratification will be discussed at the end of this section. In Fig. 54, 55, 59, and 60 x^* is normalized by L, the distance of the source to the wall, here $L = 5r_s = 0.605$.

In Case 5, the current flows for more than x^*/L=35 before reaching the outlet, allowing enough length to analyze the evolution with x^*/L.

In Figure 56, the entrainment coefficient (calculated using eq. 9) along the downslope coordinate x^* is shown. Entrainment is strongest near the source, then gradually decreases and stabilizes to a roughly constant value in the near–self-similar region (Sect. 14.1). This near self-similar region is located in Figure 56 between x^*/L=15 and x^*/L=35. This figure also shows the dependence of the entrainment coefficient on the slope angle: steeper slopes (closer to 90°) produce larger values of α. This effect, first observed by **ET59**, has since been confirmed in numerous experimental studies ([160],[96],[215]) and numerical simulations ([173],[82]).

The first quantitative study of entrainment and its dependence on the Richardson number and slope angle was conducted by **ET59** (see Sect. 11.5). In their experiments, the entrainment coefficient averaged over the time of the experiment and the length of the slope $\langle\alpha\rangle$ was determined by comparing the concentration of the outlet flow to that of the inlet. Due to experimental limitations at the time, no local value of the entrainment coefficient along the slope could be provided.

With recent simulations and measurement tools, it is now clear that the averaging method strongly influences the reported value of $\langle\alpha\rangle$. Averaging over a short distance near the source yields higher values, dominated by the strong entrainment in the adjustment zone. In contrast, averaging over a longer slope, which includes the self-similar region, produces a mean closer to the stable value characteristic of that regime (see Fig. 56).

Figure 57 compares the evolution of the averaged entrainment coefficient α along x^*/L of three studies – **ET59**, Haddad et al. [83], and Van Reeuwijk [207] – with the results of our simulations.

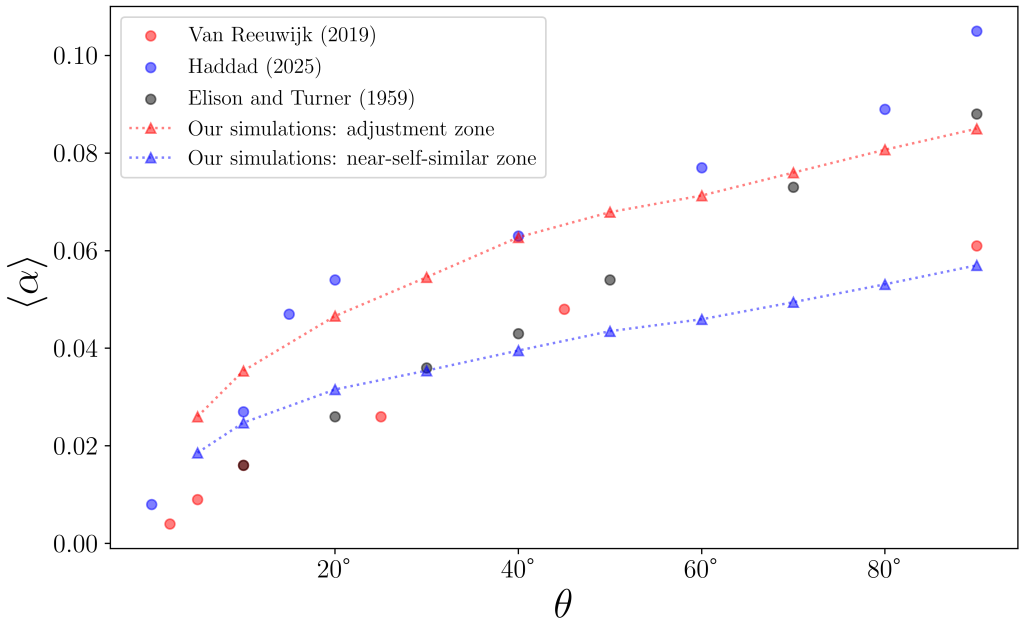

Fig. 57: Comparison of the averaged entrainment coefficient $\langle\alpha\rangle$ as a function of slope angle, based on different sources: DNS simulations by van Reeuwijk et al. [207], LES simulations by Haddad et al. [83], and laboratory experiments by **ET59**. Results from the present study are shown in dashed lines, with averages taken either over the adjustment or over the near-self-similar zone.

The experiments by **ET59** and the LES simulations by Haddad et al. [83] (using the same numerical solver as in the present work) primarily capture the adjustment zone of the gravity current, where entrainment is higher. In contrast, the DNS results of Van Reeuwijk et al. [207] focus on the self-similar region, providing a representative average for that regime. We report two averaged values of α from our simulations: one over the adjustment zone (from x^*/L=0 to x^*/L=15) and one over the near-self-similar zone (from x^*/L=15 to x^*/L=35).

Across all studies, the entrainment coefficient increases with slope angle. However, two distinct groups emerge: those that include the adjustment zone (**ET59**, Haddad et al. [83], and our adjustment-zone averages) and those restricted to the near-self-similar regime (Van Reeuwijk et al. [207] and our corresponding averages). While both groups exhibit the same increasing trend with slope angle, their absolute values differ markedly — particularly for slopes steeper than 45°, where self-similar values are about 30% lower than those including the adjustment region.

Our simulations show good agreement with the experiments of **ET59** and the LES simulations of Haddad et al. [83] for the average over the near-self-similar region and with the DNS simulations of Van Reeuwijk et al. [207] for the average over the near-self-similar zone.

The slope angle is a key parameter controlling entrainment, yet it is not the only one of relevance. An equally important quantity is the Richardson number, which provides a direct measure of the balance between buoyancy and shear. Since the pioneering work of **ET59**, the relationship between α and Ri has been extensively studied, with numerous empirical laws proposed to model it (see Table 4).

Figure 58 presents the averaged entrainment coefficient, $\langle\alpha\rangle$, as a function of the averaged Richardson number, $\langle Ri\rangle$, highlighting that entrainment decreases as the Richardson number increases. The Richardson number quantifies the balance between buoyancy and shear: a high Richardson number

indicates that the available kinetic energy is insufficient to overcome buoyancy forces, resulting in a stable configuration where mixing is strongly suppressed. In stratified environments, this stabilization limits the ability of the current to entrain ambient fluid. This behavior is further illustrated in Figure 59, which shows the entrainment coefficient along the slope for different stratification intensities, with the slope angle fixed at 60° and the buoyancy flux held constant at $B_l = 0.063$ m^3/s^3. Entrainment decreases with increasing stratification, and differences between cases become more pronounced downstream. For the strongest stratification, data are reported only near the source, as the current evolves into an intrusion beyond this point, and its entrainment dynamics are no longer directly comparable to the other cases.

The analysis based on slope angle and Richardson number provides valuable insight into the global dependence of entrainment on external parameters. To gain a deeper understanding of the physical mechanisms driving this behavior, it is useful to decompose the entrainment coefficient into its constituent contributions. The theoretical basis for this decomposition was introduced in Sect. 11.5.

In Figure 60, the different components of the entrainment decomposition are shown for various slope angles in the absence of stratification (Case 5), plotted as a function of x^*/L. The total entrainment from the decomposition, α_E (obtained as the sum of the individual terms), matches almost exactly with the directly calculated entrainment α (from eq. 9), confirming the accuracy of the decomposition.

As expected, α_{prod} emerges as the dominant positive contribution to entrainment, while α_{C_D} provides the main negative contribution. The contribution of α_{Ri} is positive and increases with the angle. α_{shape} is close to zero and very flat at 30°, but as the angle increases, a negative region appears near the source, indicating that the non-self-similar zone extends further with increasing angles.

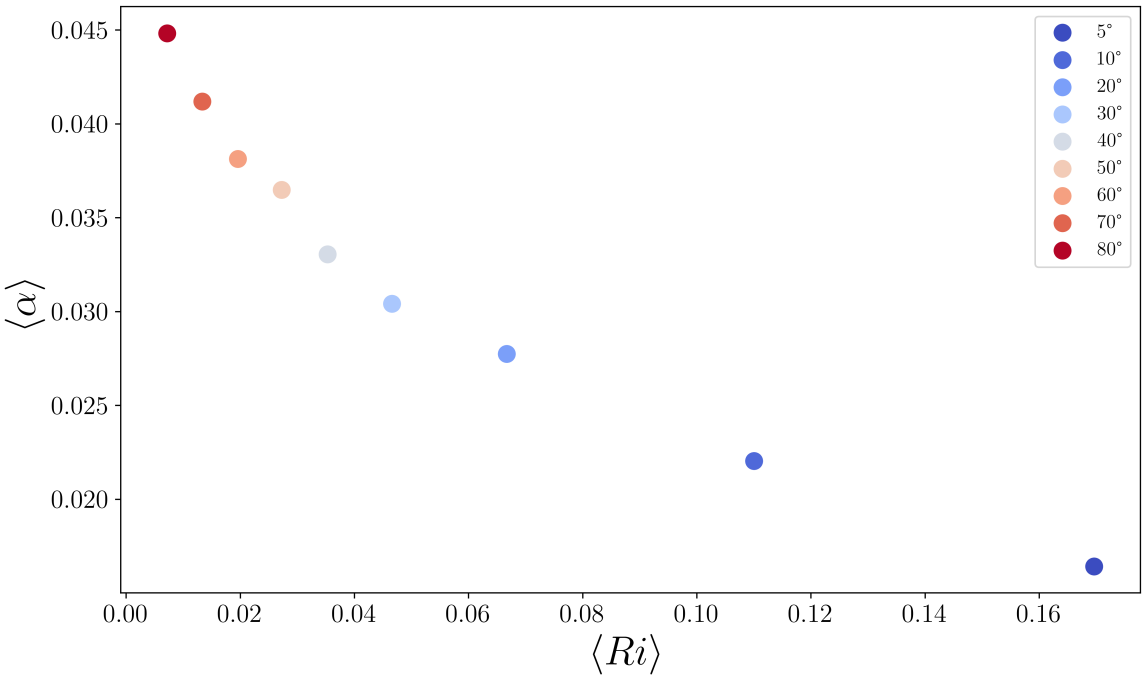

Fig. 58: The mean entrainment coefficient is presented as a function of the mean Richardson number. The averaging was performed along the slope for different slope angles, and the colors indicate the slope angles considered.

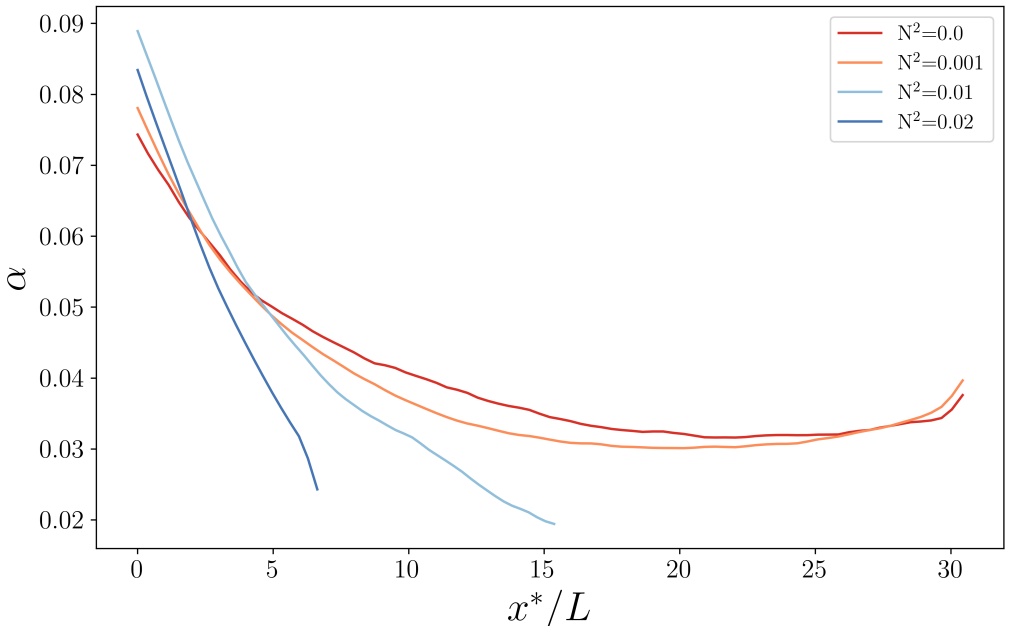

Fig. 59: Comparison of the entrainment coefficient as a function of x^* for different N^2. For the different curves, the slope angle is 60° and B_l=0.063 m^3/s^3.

The influence of slope is also clear: the absolute magnitudes of the components, both near the source and in the near-self-similar region, increase with slope angle. However, despite this increase in strength, the overall structure of the decomposition and the relative importance of the different terms remain largely unchanged across the tested angles.

14.3 Penetration depth of a laminar current

Wells and Nadarajah [214] performed a series of 41 experiments aiming to investigate the penetration depth of a gravity current flowing along a slope into a stratified ambient. They generated a dense plume of saline water and injected it at a controlled flow rate onto a sloping surface, allowing it to descend into a linearly stratified fluid.

They constructed the experimental setup using a Plexiglas tank measuring 280 cm in length, 45 cm in width, and 36 cm in height (see Figure 61). Inside the tank, they placed a movable channel with an internal width of 32 cm, which enabled them to vary the slope angle between 15° and 90°. To produce the dense current, they pumped saline solution through a 32-cm-long porous hose located 3 cm above the inclined surface. This configuration was chosen to enhance the mixing at the onset of the flow without affecting the net buoyancy flux. They varied the flow rate between 0.5 and 30 cm^3/s and adjusted the reduced gravity of the inflow from 30 to 190 cm/s^2. This led to a range of buoyancy fluxes per unit length from 0.5 to 350 cm^3/s^3. To establish the background stratification, they used the standard double-bucket technique, achieving buoyancy frequencies (N) between 0.3 and 1.7 Hz. In each experiment, they independently varied the buoyancy flux B_l and buoyancy frequency N. To visualize the flow, they added dye to the saline solution and placed a matte white background behind the tank to obtain high-contrast images.

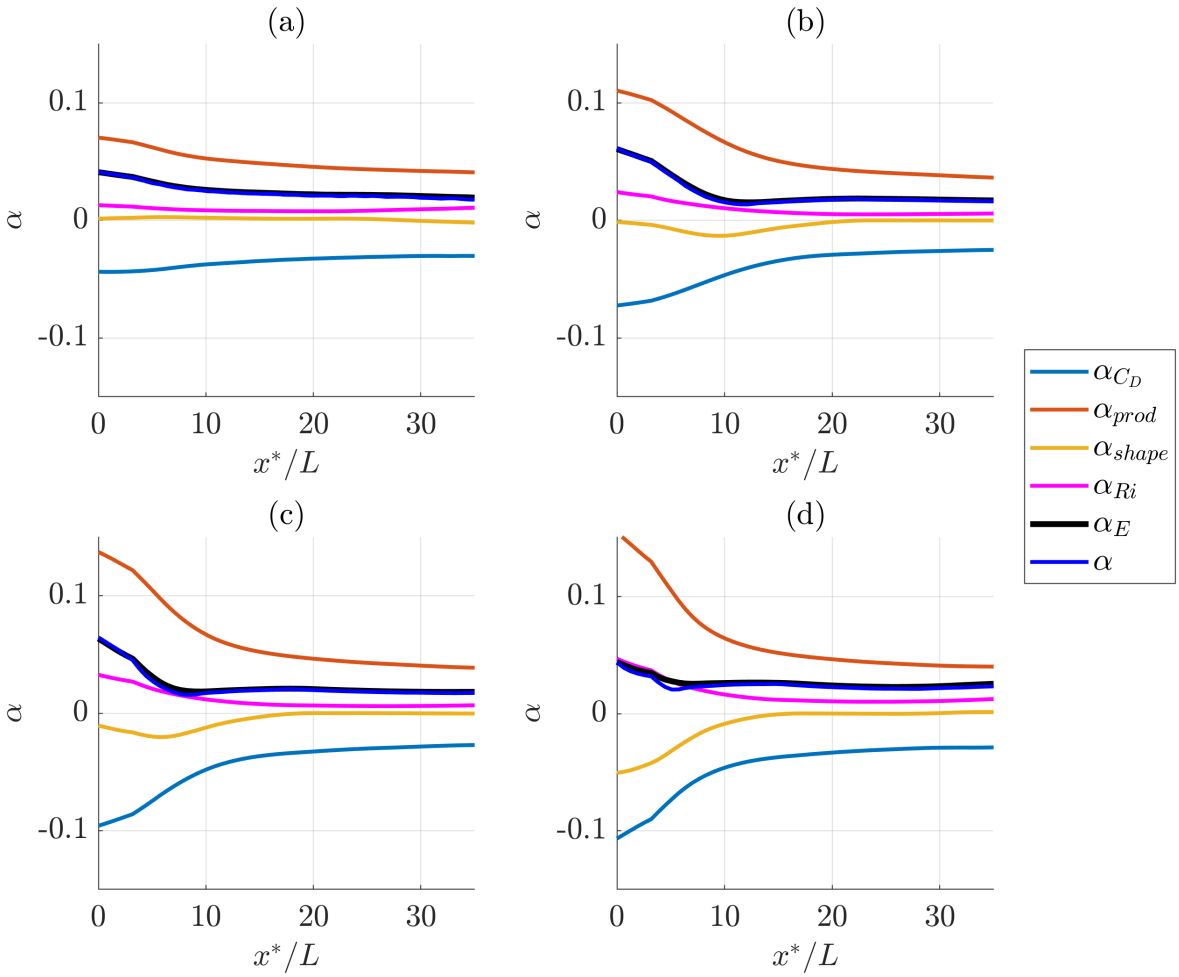

Fig. 60: The different elements of the entrainment decomposition as defined in eq. 11 for the same B_l, no stratification, and different slope angles – (a) 30°, (b) 40°, (c) 50°, and (d) 60° – as a function of x^*.

They defined the intrusion depth as the vertical distance from the source to the center of the initial intrusion. Since the observed thickness of the intrusion was typically 5–8 cm, the depth measurements exhibited relatively large uncertainties.

Each experimental run was limited to about one minute, as the intruding current began to alter the ambient stratification shortly after initiation. To maintain consistent initial conditions, they fully drained the tank and prepared a fresh linear stratification after each run. Due to the small velocities at the inlet (around 0.3 cm/s) and the small size of the setup (the current flows down for about 20 cm), the Reynolds number of the flow was lower than 500, therefore giving rise to non-turbulent flows.

We performed simulations to reproduce the results obtained by **WN09**. To this aim, we used the mesh described in Sect. 12.3 and adapted the sizes and initial conditions to suit the laminar simulations. This simulation corresponds to Case 4 in Table 7. To account for the smaller geometry, we changed the size of r_s to make it 0.005 and changed the size of the geometry to Lx=30 cm, Ly=3 cm, and Lz=5 cm. We used a velocity at the source of 3 cm/s.

We used the laminar solver of the Calif^3-Isis code that solves the Navier-Stokes equation for a laminar flow, resolving the same equations (eq. 23, 24, and 28) as the LES solver described in Sect. 12.1, but without imposing initial perturbations, excluding the turbulence.

The Calif^3-Isis software does not allow for the direct use of water and brine; therefore, we employed the same CO_2–air mixture as in the other simulations (see Sect. 12.1). To ensure consistency between

the CO2–air simulations and the water–brine experiments, we matched the Reynolds, Richardson, and Schmidt numbers. In **WN09**, a range of inlet velocities was explored, resulting in variations of both nondimensional numbers. For our study, we selected $Re = 500$ and $Ri = 5$ as representative values. The Reynolds number was matched by adjusting the inlet velocity to 3 cm/s, since the main difference between air and water lies in viscosity. The Richardson number was reproduced by imposing a density ratio of $\frac{\Delta\rho}{\rho a,0} = 1.053$, one of those used in the experiments, with an identical source size to ensure comparable inlet conditions. Finally, the Schmidt number – which represents the ratio of momentum to mass diffusivity – was also adjusted in Calif to match that of salt in water ($Sc \approx 1000$), by tuning the diffusivity properties of the CO_2–air mixture.

We performed three simulations for one angle every ten degrees, starting from 20°. The simulations had the same velocity at the inlet but different stratifications $N^2 = 2.0, 2.1$, and 2.3 Hz^2. The penetration depth was estimated in the same way as in the experiments of **WN09**, by measuring the vertical distance between the midpoint of the intrusion and the source.

In Figure 62, we present a comparison between the nondimensional penetration D_a depth (defined in equation 61) as a function of the slope angle obtained by **WN09** and in our simulations, showing a good match between the two.

In this laminar configuration, the nondimensional penetration depth D_a does not vary with the slope angle. This was one important result that the experiment of **WN09** showed. They interpreted it as being due to an entrainment coefficient per unit of depth equal for all angles. It should be noted that for 90°, a large variability of penetration depth was found, and no explanation for it is given in the original paper. Generally, we can say that the absence of dependence of the penetration depth on the angle is probably due to the mixing in this experiment being pretty small due to the laminar regime and high Richardson number.

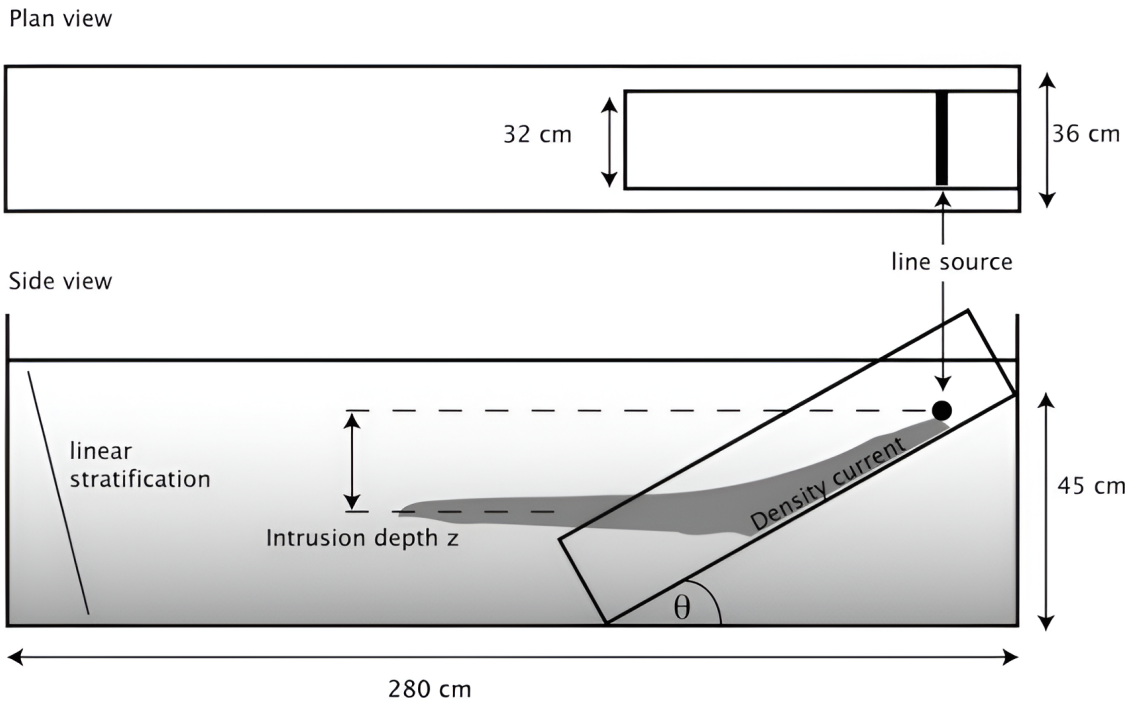

Fig. 61: Plan and side views of the tank used in the experiments of **WN09** [214]. Reproduced from [214].

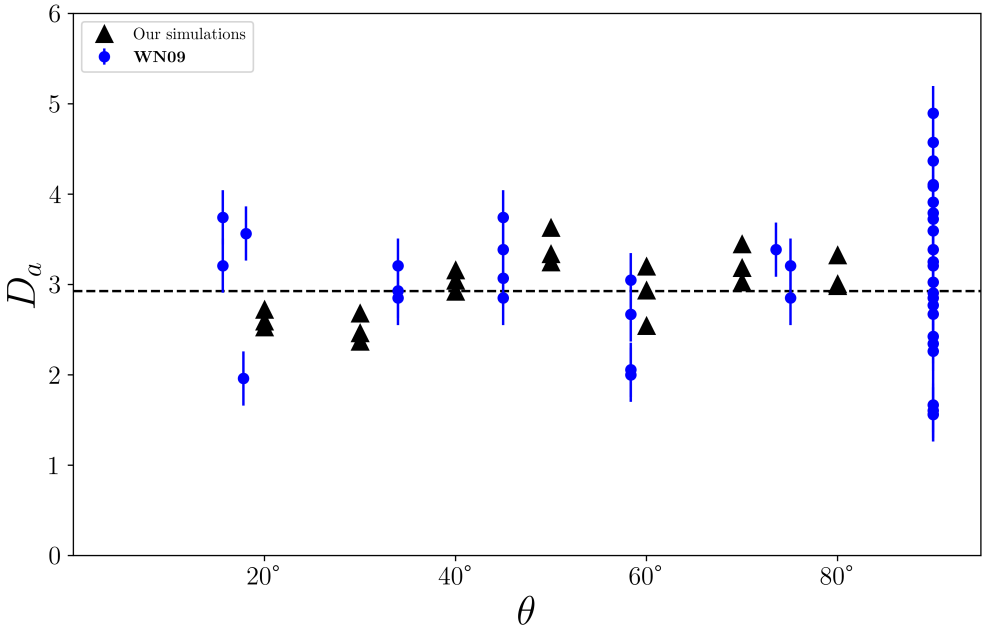

Fig. 62: Nondimensional penetration depth as a function of the slope angle. The blue dots refer to the data of **WN09**, the black dashed line marks the mean value of the experiments, and the black triangles correspond to our own simulations.

14.4 Penetration depth of a turbulent gravity current

We now present the main novel results of this third part of the thesis: an analysis of the effect of the slope angle on the nondimensional penetration depth in turbulent flows. Figure 63 shows the evolution of D_a as a function of slope angle for different configurations. The cases differ by the vertical position L of the source relative to the slope (see Table 7): in Case 1 the source is placed close to the slope at a horizontal distance of $5r_s$, in Case 2 it is farther away at $25r_s$, and in Case 3 it is positioned even farther away, at $45r_s$. A schematic representation of L is provided in Figure 43.

Compared to the laminar case, a major difference emerges: the curves are no longer flat, and the penetration depth varies with the slope angle. This behavior is a novel finding, not reported in previous studies. In Case 1 (where the source is close to the wall), we observe that D_a is smaller for the small angles, rises until it reaches its max at around 60°, then diminishes for the larger angles. For cases 2 and 3, a similar pattern is observed, but the position of the maximum changes. For Case 2, the maximum is attained for an angle of 50°, and for Case 3, for an angle of 40°. We also observe that the curve flattens and resembles the laminar case more, the farther from the wall the source is.

The non-monotonic variation of the penetration depth D_a with slope angle can be interpreted as the result of a competition between two opposing effects. First, for a given vertical depth D, the along-slope distance required to reach that depth increases as the slope angle θ decreases, following the geometric relation $D/\sin(\theta)$. As $\theta \to 0$, $1/\sin(\theta)$ becomes large, leading to significantly longer travel distances along shallower slopes. This extended path allows more time for the current to mix and dilute. Second, the entrainment intensity increases with slope angle. As demonstrated in Sect. 14.2, the entrainment coefficient exhibits an approximately linear increase with θ, leading to enhanced mixing at steeper slopes. Consequently, both shallow and steep slopes tend to produce lower values of D_a: the former due to longer paths and prolonged mixing, the latter due to more vigorous entrainment.

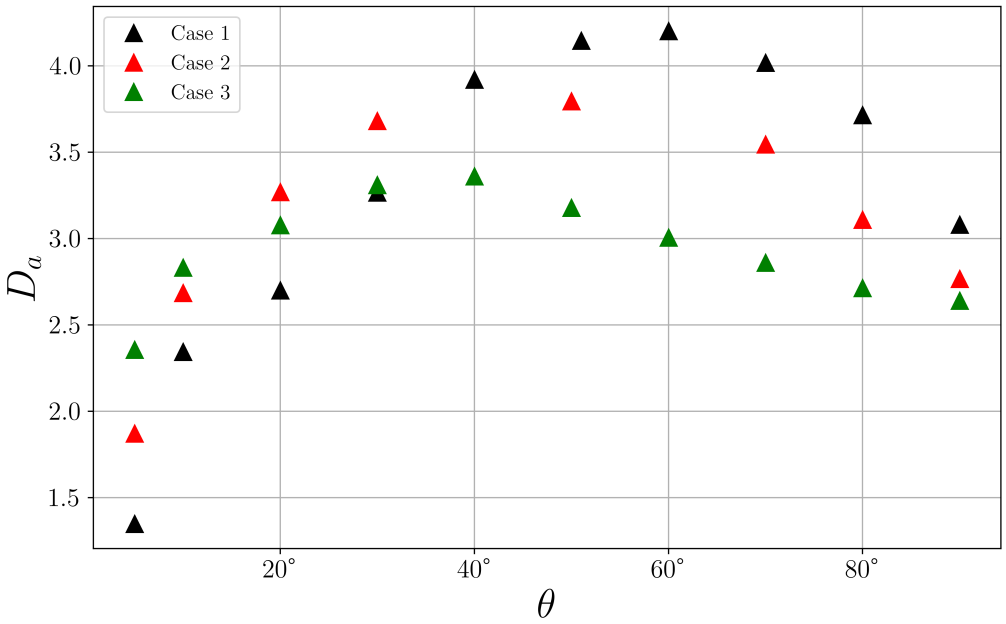

Fig. 63: Nondimensional penetration depth as a function of the slope angle for different positions of the source. The cases represent different positions of the source. In Case 1, the source is placed close to the slope at a horizontal distance of $3r_s$, in Case 2, it is farther away at $25r_s$, and in Case 3, it is positioned even farther away, at $45r_s$.

Intermediate slopes yield larger D_a values, as they combine shorter travel distances with moderate mixing rates.

The differences observed between the cases with different source positions can be attributed to the presence of an initial plume phase prior to the gravity current interacting with the slope. The duration of this phase depends on the distance between the source and the slope: the greater the distance, the longer the plume phase. Entrainment in a plume is significantly higher than in a wall-bounded flow. Specifically, the entrainment coefficient in a plume is approximately twice that of a vertical wall-bounded flow, and even more so when compared to flows along shallower slopes. Since the entrainment coefficient in a plume is universal, a sufficiently long plume phase tends to homogenize the penetration depth across different configurations. This explains the observed flattening of the penetration depth curve as the distance between the source and the slope, and thus the length of the plume phase, increases.

14.5 Scaling of the penetration depth

Given the relationship between D and θ, we aim to formulate an expression that predicts the penetration depth of a gravity current based on the source characteristics (B_l), the ambient stratification (N), and the slope angle (θ).

The penetration depth is governed by a balance between two effects: the buoyancy flux supplied at the source, B_l, which sets the velocity scale $U \sim B_l^{1/3}$, and the stabilizing effect of the ambient stratification, which acts at a rate N. In the absence of entrainment, this balance yields the characteristic length scale $B_l^{1/3}/N$. To incorporate the influence of entrainment and its variation with the

slope angle, it is necessary to account for how entrainment modifies the flow along the current's trajectory. For a gravity current descending a slope, the distance traveled along the slope is related to the vertical depth by $D/\sin(\theta)$. Since entrainment occurs per unit length along the slope, the effective dilution per unit vertical depth is proportional to $\alpha(\theta)/\sin(\theta)$, and because it acts cumulatively on the buoyancy flux along the trajectory, its contribution enters the scaling with the same one-third exponent as B_l. This reasoning leads to the scaling law:

$$D \propto \frac{[\sin(\theta)/\alpha(\theta)]^{1/3} B_l^{1/3}}{N}. \tag{37}$$

This scaling was proposed by Wells et Nadarajah in **WN09** and by He et al. [88] as explained in Sect. 11.8. Both found that this scaling worked well with their experimental data, but the way they modeled the term $\alpha(\theta)/\sin(\theta)$ differed. Wells proposed that $\alpha(\theta)/\sin(\theta)$, which he called E_{eq}, is a constant equal to 0.08; on the other hand, He et al. [88] proposed to describe α as a linear function of θ, according to the formula $\alpha = 0.0055\theta + 0.063$ derived from the experiments of Beghin et al. [19].

The scaling proposed in **WN09** is only valid for their laminar experiments, where mixing is limited and the slope has little influence on entrainment (see Sect. 14.3). The formulation of He et al. [88] incorporates the slope dependence of entrainment, but relies on the parameterization of Beghin et al. [19], which is inconsistent with both **ET59** and our results. In particular, Beghin et al. reported entrainment coefficients nearly an order of magnitude larger than **ET59** and most subsequent studies. Moreover, the scaling of He et al. [88] was only tested for slope angles between 9° and 24°. These limitations underline the need for a new scaling law, based on a physically consistent interpolation of α and validated against data spanning the full range of slope angles.

To derive a new scaling law, we first adopt a suitable expression for α and substitute it into Eq. 37. As discussed in Sect. 11.5, several formulations for the entrainment coefficient exist in the literature, typically expressed either as a function of the Richardson number Ri (Table 6) or of the slope angle θ (Table 5). Among these, the linear relationship derived from the **ET59** data by Hopfinger [94], $\alpha = 9.5 \times 10^{-4}(\theta + 5)$, provides a convenient and physically consistent interpolation.

We then tested whether this scaling holds for our numerical results and identified the corresponding proportionality constant. Figure 64 compares the penetration depth predicted by the proposed scaling with the values measured in our simulations. The agreement is excellent: the predicted and simulated depths collapse onto a single curve, yielding a proportionality constant of 0.696. Based on this result, we propose the following expression for the penetration depth of a gravity current flowing downslope into a stratified ambient:

$$D = 0.696 \left(\frac{\sin(\theta)}{9.5 \times 10^{-4}(\theta + 5)} \right)^{1/3} B_l^{1/3}/N. \tag{38}$$

This formula is valid for all angles but only for a source located close to the wall (Case 1). For the other configurations, an alternative expression would be required to account for the additional mixing that occurs during the plume phase before the current attaches to the slope.

15 Summary and closing remarks

We presented a series of numerical simulations of gravity currents flowing down a slope into a stratified ambient. This configuration corresponds to the cascading of DSW along the continental slope but also has a more general significance. The simulations were conducted using the large-eddy simulation

(LES) code Calif^3-Isis, to quantify the penetration depth of the gravity current across slope angles ranging from 5° to 90°.

We first simulated the laminar experiments performed by **WN09** [214] and were able to reproduce their results. Subsequent novel simulations were performed under fully turbulent flow conditions, revealing significant deviations from the laminar case. In the laminar case, the nondimensional (D_a) penetration depth remained relatively invariant with changes in slope angle. In contrast, turbulent simulations exhibited a strong dependence on slope angle, with D_a attaining a maximum at intermediate angles (∼60°) and decreasing toward both smaller and larger angles when the source was positioned near the wall. We also provided a physical explanation for this behavior.

Furthermore, the distance of the source to the wall was found to have a remarkable impact on the dynamics of the current. When the source was put away from the wall, the wall slope corresponding to maximal penetration shifted to lower values, while the overall variation in penetration depth with slope angle became less pronounced. This behavior can be attributed to a longer initial plume phase, where enhanced mixing with the ambient fluid occurs uniformly across all angles, thereby reducing the sensitivity of penetration depth to slope variations.

Finally, building on previous studies, we proposed a new formula to predict the penetration depth of a gravity current flowing downslope into a stratified ambient, expressed in terms of the source buoyancy flux B_l and the ambient stratification N.

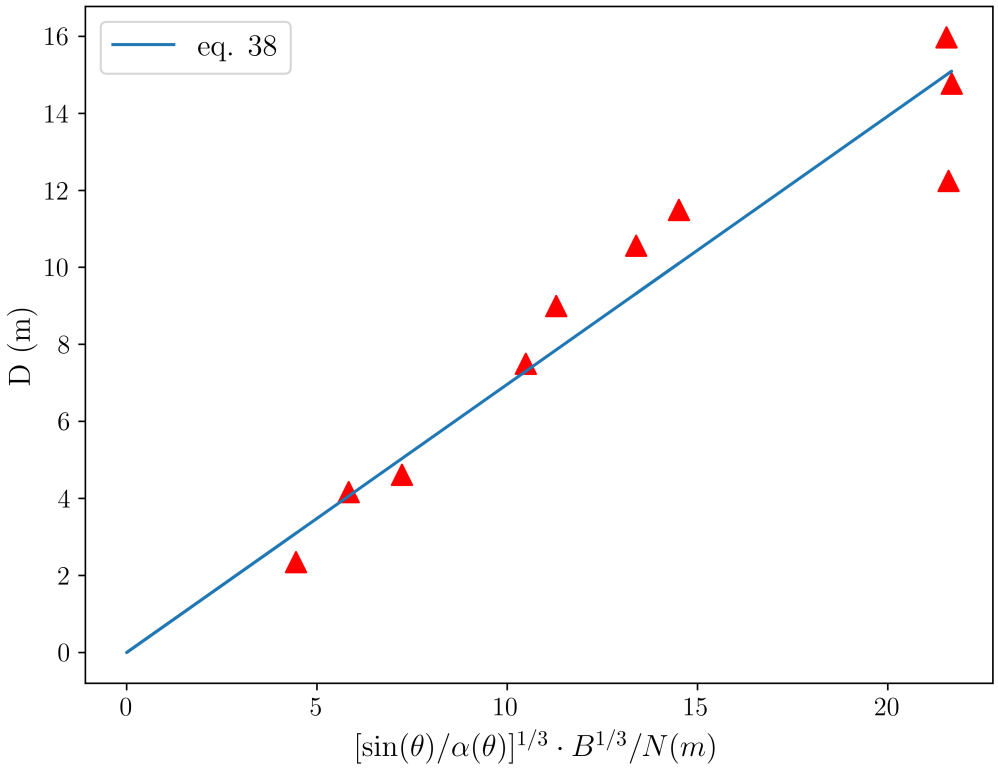

Fig. 64: Separation depth of gravity currents in linear stratifications versus the length scale according to our LES simulations.

IV Conclusions and future works

In this PhD thesis, we studied some aspects of the buoyancy-induced currents in the ocean, more specifically, the cascading of the Dense Shelf Water produced in the coastal polynyas of Antarctica along the continental shelf. These gravity currents are the main source for the Antarctic Bottom Waters and a very important component of the thermohaline circulation that is a major regulator of Earth's climate.

We divided this study into two parts: (i) the experimental investigation of a density current due to the brine rejection, and (ii) the numerical simulation of the dynamics of a density current flowing along a slope resembling the continental shelf.

The first part of the PhD was spent at the Politecnico di Torino and was concerned with the densification of the shelf water due to the brine rejection in polynya and its ability to generate density currents.

Given the lack of experimental studies on gravity current production by polynyas, we addressed this issue experimentally by constructing an experimental apparatus designed for this task. The experimental setting consisted of a cold room and an insulated tank of water, as well as measurement devices. We first tried to open a polynya with a fan blowing wind over the surface to reproduce the way Antarctic polynyas are maintained open by strong katabatic winds. Unfortunately, this approach failed as the wind did not manage to keep the polynya open for long enough and created too much convection in the water to be able to see the creation of any current. We then opted for covering most of the surface of the water with insulation and keeping open just a small part that is our polynya. By keeping the time of the experiments way shorter than the time of formation of the ice, we could study the formation of a gravity current by brine reaction in a polynya.

The laboratory experiments demonstrated that brine rejection alone is capable of generating well-defined gravity currents, with velocities on the order of millimeters per second. The systematic variation of key parameters – polynya size, external air temperature, water salinity, and bottom geometry – revealed their influence on the flow rate and structure of the current. Larger openings led to both thicker currents and higher flow rates, while increased salinity slightly enhanced the flow rate. Bottom geometry played a decisive role: vertical walls promoted a cellular structure reminiscent of Rayleigh–Bénard convection, whereas inclined walls favored the formation of continuous and well-developed currents. Both the thickness of the current and its flow rate were greater in the absence of the inclined wall than in its presence. Surprisingly, within the tested range, variations in external

air temperature did not produce a significant effect on the flow rate or current thickness, and the underlying cause for this insensitivity remains unresolved.

The second part of this PhD focused on the downslope propagation of gravity currents along the continental shelf, examined within the broader framework of gravity currents descending a slope into a stratified ambient. Our objective was to determine how the slope angle influences the penetration depth of a gravity current generated by a continuous release source.

We first performed laminar simulations, which successfully reproduced prior experimental results from the literature. We then conducted large-eddy simulations to investigate a wide range of slope angles and source configurations under turbulent conditions. For the first time, we demonstrated that laminar and turbulent gravity currents exhibit fundamentally different penetration behaviors: while laminar penetration depth (D_a) was largely insensitive to slope angle, turbulent currents showed a pronounced dependence, with maximal penetration occurring at intermediate slopes (around 60°) when the source was close to the wall. Increasing the source–wall distance altered this trend, shifting the optimum penetration angle toward lower values and reducing the overall variation with slope, an effect attributed to a prolonged plume phase with enhanced mixing across all angles. Building on these results and earlier studies, we derived a new predictive expression for the penetration depth of a downslope gravity current in a stratified environment, expressed in terms of the source buoyancy flux B_l and the ambient stratification N.

Future works

Several directions could be pursued to extend the present study. On the experimental side, a more systematic investigation of thermal effects would be highly valuable. In the present experiments, the influence of air temperature remained somewhat unclear; targeted studies – such as isolating the role of temperature in a configuration with a single opening – could help understand its role better. Another promising avenue would be to exploit the current experimental setup to investigate more realistic bathymetries, allowing the replication of specific seabed geometries and their influence on current dynamics.

On the numerical side, future efforts could focus on extending the proposed scaling for the penetration depth. In particular, an important step would be to incorporate the effect of the source–wall distance, which significantly alters the dynamics by introducing an initial plume phase before wall attachment. Developing a modified formulation that accounts for this additional mixing would provide a more general predictive tool for downslope gravity currents in stratified environments.

References

[1] Adolphs U, Wendler G (1995) A pilot study on the interactions between katabatic winds and polynyas at the Adélie Coast, eastern Antarctica. Antarctic Science 7(3):307–314

[2] Adusumilli S, Fricker HA, Medley B, et al (2020) Interannual variations in meltwater input to the Southern Ocean from Antarctic ice shelves. Nature geoscience 13(9):616–620

[3] Al-Achi A (2019) The student's t-test: a brief description. Research & Reviews: Journal of Hospital and Clinical Pharmacy 5(1):1

[4] Allen S, Durrieu de Madron X (2009) A review of the role of submarine canyons in deep-ocean exchange with the shelf. Ocean Science 5(4):607–620

[5] Alley KE, Scambos TA, Siegfried MR, et al (2016) Impacts of warm water on Antarctic ice shelf stability through basal channel formation. Nature Geoscience 9(4):290–293

[6] Amblas D, Dowdeswell J (2018) Physiographic influences on dense shelf-water cascading down the Antarctic continental slope. Earth-Science Reviews 185:887–900

[7] Anderson JB, Brake CF, Myers NC (1984) Sedimentation on the Ross Sea continental shelf, Antarctica. Marine Geology 57(1-4):295–333

[8] Antenucci JP, Brookes JD, Hipsey MR (2005) A simple model for quantifying Cryptosporidium transport, dilution, and potential risk in reservoirs. Journal-American Water Works Association 97(1):86–93

[9] Aoki S, Yamazaki K, Hirano D, et al (2020) Reversal of freshening trend of Antarctic Bottom Water in the Australian-Antarctic Basin during 2010s. Scientific reports 10(1):14415

[10] Arndt JE, Schenke HW, Jakobsson M, et al (2013) The International Bathymetric Chart of the Southern Ocean (IBCSO) Version 1.0—A new bathymetric compilation covering circum-Antarctic waters. Geophysical Research Letters 40(12):3111–3117

[11] Arrigo KR, van Dijken GL (2003) Phytoplankton dynamics within 37 Antarctic coastal polynya systems. Journal of Geophysical Research: Oceans 108(C8)

[12] Baines PG (2001) Mixing in flows down gentle slopes into stratified environments. Journal of Fluid Mechanics 443:237–270

[13] Baines PG (2002) Two-dimensional plumes in stratified environments. Journal of Fluid Mechanics 471:315–337

[14] Baines PG (2005) Mixing regimes for the flow of dense fluid down slopes into stratified environments. Journal of Fluid mechanics 538:245–267

[15] Baines PG, Condie S (1998) Observations and modelling of Antarctic downslope flows: A review. Ocean, Ice, and Atmosphere: Interactions at the Antarctic Continental Margin, Antarct Res Ser 75:29–49

[16] Baringer MO, Price JF (1999) A review of the physical oceanography of the Mediterranean outflow. Marine Geology 155(1-2):63–82

[17] Basak C, Fröllje H, Lamy F, et al (2018) Breakup of last glacial deep stratification in the South Pacific. Science 359(6378):900–904

[18] Beghin P, Hopfinger E, Britter R (1981) Gravitational convection from instantaneous sources on inclined boundaries. Journal of Fluid Mechanics 107:407–422

[19] Beghin P, Hopfinger E, Britter R (1981) Gravitational convection from instantaneous sources on inclined boundaries. Journal of Fluid Mechanics 107:407–422

[20] Benjamin TB (1968) Gravity currents and related phenomena. Journal of fluid mechanics 31(2):209–248

[21] Birman V, Meiburg E, Ungarish M (2007) On gravity currents in stratified ambients. Physics of Fluids 19(8)

[22] Bournet P, Dartus D, Tassin B, et al (1999) Numerical investigation of plunging density current. Journal of Hydraulic Engineering 125(6):584–594

[23] Bouttes N, Paillard D, Roche DM, et al (2012) Impact of oceanic processes on the carbon cycle during the last termination. Climate of the Past 8(1):149–170

[24] Briggs G (1969) Optimum formulas for buoyant plume rise. Philosophical Transactions of the Royal Society of London Series A, Mathematical and Physical Sciences 265(1161):197–203

[25] Briggs G (1981) Ganopy effects on predicted drainage flow characteristics and comparisons with observations. Proc 5th Symp on Turb and Diff, 1981 pp 113–115

[26] Britter R, Linden P (1980) The motion of the front of a gravity current travelling down an incline. Journal of Fluid Mechanics 99(3):531–543

[27] Brown WS (2016) Physical properties of seawater. Springer, pp 101–110

[28] Bruneau CH (2000) Boundary conditions on artificial frontiers for incompressible and compressible Navier-Stokes equations. ESAIM: Mathematical Modelling and Numerical Analysis 34(2):303–314

[29] Bruneau CH, Fabrie P (1994) Effective downstream boundary conditions for incompressible Navier–Stokes equations. International Journal for Numerical Methods in Fluids 19(8):693–705

[30] Bruneau CH, Fabrie P (1996) New efficient boundary conditions for incompressible Navier-Stokes equations: a well-posedness result. ESAIM: Mathematical Modelling and Numerical Analysis 30(7):815–840

[31] Buchart L, Castro de la Guardia L, Xu Y, et al (2022) Future climate scenarios for northern Baffin Bay and the Pikialasorsuaq (North Water Polynya) region. Atmosphere-Ocean 60(2):102–123

[32] Budéus G, Schneider W (1995) On the hydrography of the Northeast Water Polynya. Journal of Geophysical Research: Oceans 100(C3):4287–4299

[33] Bush JW, Woods AW (1999) Vortex generation by line plumes in a rotating stratified fluid. Journal of Fluid Mechanics 388:289–313

[34] Cadot N, Camporeale C, Ridolfi L, et al (2025) Laboratory experiments on Dense Shelf Water formation. Environmental Fluid Mechanics 25(3):25

[35] Campbell EC, Wilson EA, Moore GK, et al (2019) Antarctic offshore polynyas linked to Southern Hemisphere climate anomalies. Nature 570(7761):319–325

[36] Cardoso SS, Woods AW (1993) Mixing by a turbulent plume in a confined stratified region. Journal of Fluid Mechanics 250:277–305

[37] Caulfield C, Woods AW (1998) Turbulent gravitational convection from a point source in a non-uniformly stratified environment. Journal of fluid mechanics 360:229–248

[38] Chen Z, Jiang Y, Wang J, et al (2019) Influence of a river plume on coastal upwelling dynamics: Importance of stratification. Journal of Physical Oceanography 49(9):2345–2363

[39] Choi SU, Garc ı´ a MH (2002) k-ε turbulence modeling of density currents developing two dimensionally on a slope. Journal of Hydraulic Engineering 128(1):55–63

[40] Chowdhury MR, Testik FY (2014) A review of gravity currents formed by submerged single-port discharges in inland and coastal waters. Environmental fluid mechanics 14:265–293

[41] Christodoulou GC (1986) Interfacial mixing in stratified flows. Journal of hydraulic research 24(2):77–92

[42] Comiso J, Gordon A (1997) Cosmonaut polynya in the Southern Ocean: structure and variability. Oceanographic Literature Review 3(44):183

[43] Corcos G, Sherman F (1984) The mixing layer: deterministic models of a turbulent flow. Part 1. Introduction and the two-dimensional flow. Journal of Fluid Mechanics 139:29–65

[44] Cornish S, Johnson H, Mallett R, et al (2022) Rise and fall of sea ice production in the Arctic Ocean's ice factories. Nature Communications 13(1):7800

[45] Cortés A, Rueda F, Wells M (2014) Experimental observations of the splitting of a gravity current at a density step in a stratified water body. Journal of Geophysical Research: Oceans 119(2):1038–1053

[46] Cox GF, Weeks WF (1974) Salinity variations in sea ice. Journal of Glaciology 13(67):109–120

[47] Craske J, van Reeuwijk M (2015) Energy dispersion in turbulent jets. Part 1. Direct simulation of steady and unsteady jets. Journal of Fluid Mechanics 763:500–537

[48] Dade WB, Huppert HE (1994) Scaling of compositional gravity currents in porous media. Physics of Fluids 6(2):395–401

[49] Dai A (2013) Gravity currents propagating on sloping boundaries. Journal of Hydraulic Engineering 139(6):593–601

[50] Dai A (2014) Non-Boussinesq gravity currents propagating on different bottom slopes. Journal of Fluid Mechanics 741:658–680

[51] Dai A, Garcia MH (2013) Frictional effects in density currents propagating on slopes. Environmental Fluid Mechanics 13(1):59–80

[52] Dai A, Krotov A, Garcia MH (2010) Entrainment and detrainment in gravity currents propagating on slopes. Journal of Hydraulic Research 48(6):765–773

[53] Dai A, Ozdemir C, Cantero M, et al (2012) Gravity currents from instantaneous sources down a slope. Journal of Hydraulic Engineering 138(3):237–246

[54] Dake JM, Harleman DR (1969) Thermal stratification in lakes: analytical and laboratory studies. Water resources research 5(2):484–495

[55] Dallimore CJ, Imberger J, Ishikawa T (2001) Entrainment and turbulence in saline underflow in Lake Ogawara. Journal of Hydraulic Engineering 127(11):937–948

[56] De Steur L, Holland D, Muench R, et al (2007) The warm-water "Halo" around Maud Rise: Properties, dynamics and impact. Deep Sea Research Part I: Oceanographic Research Papers 54(6):871–896

[57] Devenish B, Rooney G, Thomson D (2010) Large-eddy simulation of a buoyant plume in uniform and stably stratified environments. Journal of Fluid Mechanics 652:75–103

[58] DuVivier AK, Molina MJ, Deppenmeier AL, et al (2024) Projections of winter polynyas and their biophysical impacts in the Ross Sea Antarctica. Climate Dynamics 62(2):989–1012

[59] Ebner L, Heinemann G, Haid V, et al (2014) Katabatic winds and polynya dynamics at Coats Land, Antarctica. Antarctic Science 26(3):309–326

[60] Ellison T, Turner J (1959) Turbulent entrainment in stratified flows. Journal of Fluid Mechanics 6(3):423–448

[61] Emery KO (1969) The continental shelves. Scientific American 221(3):106–125

[62] of the EPICA members C (2004) Eight glacial cycles from an Antarctic ice core. Nature 429(6992):623–628

[63] Fay JA (1969) The spread of oil slicks on a calm sea. Springer, pp 53–63

[64] Fernandez D, Imberger J (2008) The influence of slope and initial density distribution on gravity currents in a rotating system. Journal of Fluid Mechanics 600:339–363

[65] Fernandez RL, Imberger J (2006) Bed roughness induced entrainment in a high Richardson number underflow. Journal of Hydraulic Research 44(6):725–738

[66] Fernando HJ (1991) Turbulent mixing in stratified fluids. Annual review of fluid mechanics 23:455–493

[67] Firoozabadi B, Afshin H, Aram E (2009) Three-dimensional modeling of density current in a straight channel. Journal of Hydraulic Engineering 135(5):393–402

[68] Foster TD (1969) Experiments on haline convection induced by the freezing of sea water. Journal of Geophysical Research 74(28):6967–6974

[69] Foster TD, Carmack EC (1976) Frontal zone mixing and Antarctic Bottom Water formation in the southern Weddell Sea. Deep Sea Research and Oceanographic Abstracts 23(4):301–317

[70] Fretwell P, Pritchard HD, Vaughan DG, et al (2013) Bedmap2: improved ice bed, surface and thickness datasets for Antarctica. The cryosphere 7(1):375–393

[71] Ganopolski A (2024) Toward generalized Milankovitch theory (GMT). Climate of the Past 20(1):151–185

[72] George WK (1992) Self-preservation of temperature fluctuations in isotropic turbulence. Studies in turbulence pp 514–528

[73] Germano M, Piomelli U, Moin P, et al (1991) A dynamic subgrid-scale eddy viscosity model. Physics of Fluids A: Fluid Dynamics 3(7):1760–1765

[74] Gilbert E, Holmes C (2024) 2023's Antarctic sea ice extent is the lowest on record. Weather 79(2):46–51

[75] Gillie ER, Bryndum-Buchholz A, Willis SG, et al (2024) Exploring novel North Water Polynya ecosystems under climate change. PLOS Climate 3(10):e0000490

[76] Gillie ER, Bryndum-Buchholz A, Willis SG, et al (2024) Exploring novel North Water Polynya ecosystems under climate change. PLOS Climate 3(6):e0000490

[77] Golledge NR, Keller ED, Gossart A, et al (2025) Antarctic coastal polynyas in the global climate system. Nature Reviews Earth & Environment 6

[78] Gordon AL (1991) Two stable modes of Southern Ocean winter stratification. Elsevier Oceanography Series 57:17–35

[79] Gordon AL, Comiso JC (1988) Polynyas in the southern ocean. Scientific American 258(6):90–97

[80] Gordon AL, Orsi AH, Muench R, et al (2009) Western Ross Sea continental slope gravity currents. Deep Sea Research Part II: Topical Studies in Oceanography 56(13-14):796–817

[81] Guo Y, Zhang Z, Shi B (2014) Numerical simulation of gravity current descending a slope into a linearly stratified environment. Journal of Hydraulic Engineering 140(12):04014061

[82] Haddad S (2023) Contribution à la modélisation des courants de gravité en régime stationnaire pour des fluides miscibles. PhD thesis, Aix-Marseile Université

[83] Haddad S, Vaux S, Varrall K, et al (2025) Turbulent entrainment in buoyant releases from horizontal gravity current to vertical planar wall plume

[84] Hanouzet R (2019) Propagation et mélange d'un fluide léger issu d'une source de flottabilité: application aux incendies dans les galeries souterraines à forte pente. PhD thesis, Aix-Marseille

[85] Hansen B, Østerhus S (2007) Faroe bank channel overflow 1995–2005. Progress in Oceanography 75(4):817–856

[86] Härtel C, Meiburg E, Necker F (2000) Analysis and direct numerical simulation of the flow at a gravity-current head. Part 1. Flow topology and front speed for slip and no-slip boundaries. Journal of Fluid Mechanics 418:189–212

[87] Haumann FA, Moorman R, Riser SC, et al (2020) Supercooled southern ocean waters. Geophysical Research Letters 47(20):e2020GL090242

[88] He Z, Zhao L, Lin T, et al (2017) Hydrodynamics of gravity currents down a ramp in linearly stratified environments. Journal of Hydraulic Engineering 143(3):04016085

[89] He Z, Lv Y, Yuan Y, et al (2019) Front propagation of gravity currents on inclined bottoms in linearly stratified fluids. Environmental Fluid Mechanics 19:279–296

[90] Hebbert B, Patterson J, Loh I, et al (1979) Collie river underflow into the Wellington reservoir. Journal of the Hydraulics Division 105(5):533–545

[91] Herbert TD (2023) The mid-Pleistocene climate transition. Annual Review of Earth and Planetary Sciences 51(1):389–418

[92] Heywood KJ, King BA (2002) Water masses and baroclinic transports in the South Atlantic and Southern oceans

[93] Holland DM (2000) Transient sea-ice polynya forced by oceanic flow variability. Progress in Oceanography 48(4):403–460

[94] Hopfinger E (1983) Snow avalanche motion and related phenomena. Annual review of fluid mechanics 15(1):47–76

[95] Huang H, Gutjahr M, Eisenhauer A, et al (2020) No detectable Weddell Sea Antarctic bottom water export during the last and penultimate glacial maximum. Nature communications 11(1):424

[96] Hughes G, Griffiths R (2006) A simple convective model of the global overturning circulation, including effects of entrainment into sinking regions. Ocean Modelling 12(1-2):46–79

[97] Huppert HE, Simpson JE (1980) The slumping of gravity currents. Journal of Fluid Mechanics 99(4):785–799

[98] IRSN (2021) CALIF3S-ISIS V6 : Physical Modelling. Tech. rep., Institut de Radioprotection et de Sûreté Nucléaire

[99] Jarrin N, Benhamadouche S, Laurence D, et al (2006) A synthetic-eddy-method for generating inflow conditions for large-eddy simulations. International Journal of Heat and Fluid Flow 27(4):585–593

[100] Johnson CG, Hogg AJ (2013) Entraining gravity currents. Journal of Fluid Mechanics 731:477–508

[101] Kämpf J (2005) Cascading-driven upwelling in submarine canyons at high latitudes. Journal of Geophysical Research: Oceans 110(C2)

[102] Kessel Tv, Kranenburg C (1996) Gravity current of fluid mud on sloping bed. Journal of Hydraulic Engineering 122(12):710–717

[103] Knorr G, Barker S, Zhang X, et al (2021) A salty deep ocean as a prerequisite for glacial termination. Nature Geoscience 14(12):930–936

[104] Kobayashi H, Abe-Ouchi A, Oka A (2015) Role of Southern Ocean stratification in glacial atmospheric CO2 reduction evaluated by a three-dimensional ocean general circulation model. Paleoceanography 30(9):1202–1216

[105] Krumpen T, Hölemann JA, Willmes S, et al (2011) Sea ice production and water mass modification in the eastern Laptev Sea. Journal of Geophysical Research: Oceans 116(C5)

[106] Ladyzhenskaya OA (2003) Sixth problem of the millennium: Navier-Stokes equations, existence and smoothness. Russian Mathematical Surveys 58(2):251

[107] Lake R, Lewis E (1970) Salt rejection by sea ice during growth. Journal of Geophysical Research 75(3):583–597

[108] Lanzini S, Marro M, Creyssels M, et al (2024) Helium plumes at moderate Reynolds number. Physical Review Fluids 9(6):064501

[109] Libbrecht KG (2005) The physics of snow crystals. Reports on progress in physics 68(4):855

[110] Libbrecht KG (2017) Physical dynamics of ice crystal growth. Annual Review of Materials Research 47(1):271–295

[111] List E, Koh RC, et al (1979) Mixing in inland and coastal waters

[112] Lofquist K (1960) Flow and stress near an interface between stratified liquids. The Physics of Fluids 3(2):158–175

[113] Lou Y, He Z, Jiang H, et al (2019) Numerical simulation of two coalescing turbulent forced plumes in linearly stratified fluids. Physics of Fluids 31(3)

[114] MacIntyre S, Sickman JO, Goldthwait SA, et al (2006) Physical pathways of nutrient supply in a small, ultraoligotrophic arctic lake during summer stratification. Limnology and Oceanography 51(2):1107–1124

[115] Mahdinia M, Firoozabadi B, Farshchi M, et al (2012) Large eddy simulation of Lock-Exchange flow in a curved channel. Journal of Hydraulic Engineering 138(1):57–70

[116] Marchese C, Albouy C, Tremblay JÉ, et al (2017) Changes in phytoplankton bloom phenology over the North Water (NOW) polynya: a response to changing environmental conditions. Polar Biology 40(9):1721–1737

[117] Maries A, Haque A, Yilmaz SL, et al (2012) Interactive exploration of stress tensors used in computational turbulent combustion. Springer

[118] Markus T, Burns BA (1995) A method to estimate subpixel-scale coastal polynyas with satellite passive microwave data. Journal of Geophysical Research: Oceans 100(C3):4473–4487

[119] Marsland SJ, Church JA, Bindoff NL, et al (2007) Antarctic coastal polynya response to climate change. Journal of Geophysical Research: Oceans 112(C4)

[120] Maslanik J, Fowler C, Stroeve J, et al (2007) A younger, thinner Arctic ice cover: Increased potential for rapid, extensive sea-ice loss. Geophysical Research Letters 34(24)

[121] Mason OK, Gerlach SC (1995) Chukchi hot spots, paleo-polynyas, and caribou crashes: Climatic and ecological dimensions of North Alaska prehistory. Arctic Anthropology 32(1):101–130

[122] Massom RA, Stammerjohn SE (2010) Antarctic sea ice change and variability: Physical and ecological implications. Polar Science 4(2):149–186

[123] McCullough GK, Barber D, Cooley PM (2007) The vertical distribution of runoff and its suspended load in Lake Malawi. Journal of Great Lakes Research 33(2):449–465

[124] Mehaddi R, Vaux S, Candelier F, et al (2015) On the modelling of steady turbulent fountains. Environmental Fluid Mechanics 15:1115–1134

[125] Mensah V, Nakayama Y, Fujii M, et al (2021) Dense water downslope flow and AABW production in a numerical model: Sensitivity to horizontal and vertical resolution in the region off Cape Darnley polynya. Ocean Modelling 165:101843

[126] Middleton C, Thomas C, De Wit A, et al (2016) Visualizing brine channel development and convective processes during artificial sea-ice growth using Schlieren optical methods. Journal of Glaciology 62(231):1–17

[127] Milankovitch M (1941) Kanon der Erdbestrahlung und seine Anwendung auf das Eiszeitenproblem. Royal Serbian Academy Special Publication 133:1–633

[128] Miller UK, Zappa CJ, Gordon AL, et al (2024) The coupling of winds, ocean turbulence, and High Salinity Shelf Water in the Terra Nova Bay Polynya. Deep Sea Research Part II: Topical Studies in Oceanography 218:105412

[129] Milward J, Beadling R, Krasting JP, et al (2024) Steric Sea Level Response to Antarctic Meltwater Addition. AGU Fall Meeting Abstracts 2024(608):OS21C–0608

[130] MITSUDERA H (1992) Downslope boundaty currents in a continuously-stratified environment: a model of the Bass Strait outflow. Proc 11th Australasian Fluid Mechanics Conf pp 1017–1028

[131] Monaghan JJ, Cas RA, Kos A, et al (1999) Gravity currents descending a ramp in a stratified tank. Journal of Fluid Mechanics 379:39–69

[132] Moore D, Weiss N (1973) Two-dimensional Rayleigh-Bénard convection. Journal of Fluid Mechanics 58(2):289–312

[133] Morales Maqueda MA, Willmott AJ, Biggs N (2004) Polynya dynamics: A review of observations and modeling. Reviews of Geophysics 42(1)

[134] Morton BR, Taylor GI, Turner JS (1956) Turbulent gravitational convection from maintained and instantaneous sources. Proceedings of the Royal Society of London Series A Mathematical and Physical Sciences 234(1196):1–23

[135] Mu L, Stammerjohn S, Lowry K, et al (2014) Spatial variability of surface p CO2 and air-sea CO2 flux in the Amundsen Sea Polynya, Antarctica. Elementa 3:000036

[136] Muench RD, Gordon AL (1995) Circulation and transport of water along the western Weddell Sea margin. Journal of Geophysical Research: Oceans 100(C9):18503–18515

[137] Mustafa J, Ghasem N, El-Naas MH, et al (2024) CFD modeling for optimal electrodialysis: Valorizing reject brine and carbon dioxide for sustainable solutions. Separation and Purification Technology 328:125083

[138] Negretti ME, Flor JB, Hopfinger EJ (2017) Development of gravity currents on rapidly changing slopes. Journal of Fluid Mechanics 833:70–97

[139] Negretti ME, Tucciarone FL, Wirth A (2021) Intruding gravity currents and re-circulation in a rotating frame: Laboratory experiments. Physics of Fluids 33(9)

[140] Nicoud F, Ducros F (1999) Subgrid-scale stress modelling based on the square of the velocity gradient tensor. Flow, turbulence and Combustion 62(3):183–200

[141] Niedrauer TM, Martin S (1979) An experimental study of brine drainage and convection in young sea ice. Journal of Geophysical Research: Oceans 84(C3):1176–1186

[142] Nihashi S, Ohshima KI (2015) Circumpolar mapping of Antarctic coastal polynyas and landfast sea ice: Relationship and variability. Journal of climate 28(9):3650–3670

[143] Nissen C, Timmermann R, Hoppema M, et al (2022) Abruptly attenuated carbon sequestration with Weddell Sea dense waters by 2100. Nature Communications, 13, 3402

[144] O'hern T, Weckman E, Gerhart A, et al (2005) Experimental study of a turbulent buoyant helium plume. Journal of Fluid Mechanics 544:143–171

[145] Ohshima KI, Fukamachi Y, Williams GD, et al (2013) Antarctic Bottom Water production by intense sea-ice formation in the Cape Darnley polynya. Nature Geoscience 6(3):235–240

[146] Ooi SK, Constantinescu G, Weber LJ (2007) 2D large-eddy simulation of lock-exchange gravity current flows at high Grashof numbers. Journal of Hydraulic Engineering 133(9):1037–1047

[147] Orsi AH, Smethie Jr WM, Bullister JL (2002) On the total input of Antarctic waters to the deep ocean: A preliminary estimate from chlorofluorocarbon measurements. Journal of Geophysical Research: Oceans 107(C8):31–1

[148] Özgökmen TM, Fischer PF, Johns WE (2006) Product water mass formation by turbulent density currents from a high-order nonhydrostatic spectral element model. Ocean Modelling 12(3-4):237–267

[149] Paillard D (1998) The timing of Pleistocene glaciations from a simple multiple-state climate model. Nature 391(6665):378–381

[150] Paillard D (2009) Last Glacial Termination. Encyclopedia of Paleoclimatology and Ancient Environments pp 495–498

[151] Paillard D (2020) Climate and astronomical cycles. Paleoclimatology pp 385–404

[152] Paillat S, Kaminski E (2014) Entrainment in plane turbulent pure plumes. Journal of Fluid Mechanics 755:R2

[153] Park YH, Charriaud E, Fieux M (1998) Thermohaline structure of the Antarctic surface water/winter water in the Indian sector of the Southern Ocean. Journal of Marine Systems 17(1-4):5–23

[154] Parker D, Burridge HC, Partridge J, et al (2020) A comparison of entrainment in turbulent line plumes adjacent to and distant from a vertical wall. Journal of Fluid Mechanics 882:A4

[155] Parker G, Fukushima Y, Pantin HM (1986) Self-accelerating turbidity currents. Journal of Fluid Mechanics 171:145–181

[156] Parker G, Garcia M, Fukushima Y, et al (1987) Experiments on turbidity currents over an erodible bed. Journal of Hydraulic Research 25(1):123–147

[157] Parkinson CL (2022) Arctic sea ice coverage from 43 years of satellite passive-microwave observations. Frontiers in Remote Sensing 3:1021781

[158] Pawłowski B (2019) Ice jams: Causes and effects. Encyclopedia of Water, 1st ed; Maurice, P, Ed pp 1–9

[159] Pease CH (1987) The size of wind-driven coastal polynyas. Journal of Geophysical Research: Oceans 92(C7):7049–7059

[160] Pedersen FB (1980) A monograph on turbulent entrainment and friction in two-layer stratified flow. Institute of Hydrodynamics and Hydraulic Engineering, Technical University

[161] Petit JR, Jouzel J, Raynaud D, et al (1999) Climate and atmospheric history of the past 420,000 years from the Vostok ice core, Antarctica. Nature 399(6735):429–436

[162] Piola AR, Georgi DT (1982) Circumpolar properties of Antarctic intermediate water and Subantarctic Mode Water. Deep Sea Research Part A Oceanographic Research Papers 29(6):687–711

[163] Price JF, Baringer MO (1994) Outflows and deep water production by marginal seas. Progress in Oceanography 33(3):161–200

[164] Priestley C, Ball F (1955) Continuous convection from an isolated source of heat. Quarterly Journal of the Royal Meteorological Society 81(348):144–157

[165] Princevac M, Fernando H, Whiteman CD (2005) Turbulent entrainment into natural gravity-driven flows. Journal of Fluid Mechanics 533:259–268

[166] Pritchard H, Ligtenberg SR, Fricker HA, et al (2012) Antarctic ice-sheet loss driven by basal melting of ice shelves. Nature 484(7395):502–505

[167] Purkey SG, Johnson GC (2013) Antarctic Bottom Water warming and freshening: Contributions to sea level rise, ocean freshwater budgets, and global heat gain. Journal of Climate 26(16):6105–6122

[168] Quaini A, San O, Veneziani A, et al (2024) Bridging Large Eddy Simulation and Reduced Order Modeling of Convection-Dominated Flows through Spatial Filtering: Review and Perspectives. arXiv preprint arXiv:240700231

[169] Rhee T, Zappa C, Kwon Y (2022) Significant Atmospheric CO2 Uptake by Antarctic Polynyas. Under Review

[170] Rimoldi B, Alexander J, Morris S (1996) Experimental turbidity currents entering density-stratified water: analogues for turbidites in Mediterranean hypersaline basins. Sedimentology 43(3):527–540

[171] Rogachev KA, Carmack EC, Salomatin AS (2000) Strong tidal mixing and ventilation of cold intermediate water at Kashevarov Bank, Sea of Okhotsk. Journal of oceanography 56(4):439–447

[172] Sagaut P (2005) Large eddy simulation for incompressible flows: an introduction. Springer

[173] Salinas JS, Zúñiga S, Cantero MI, et al (2022) Slope dependence of self-similar structure and entrainment in gravity currents. Journal of Fluid Mechanics 934:R4

[174] Salizzoni P, Vaux S, Creyssels M, et al (2023) Turbulent transfer and entrainment in a low-density jet. Journal of Fluid Mechanics 968:A27

[175] Samothrakis P, Cotel A (2006) Finite volume gravity currents impinging on a stratified interface. Experiments in Fluids 41:991–1003

[176] Sangras R, Dai Z, Faeth G (2000) Velocity statistics of plane self-preserving buoyant turbulent adiabatic wall plumes. J Heat Transfer 122(4):693–700

[177] Schauer U, Loeng H, Rudels B, et al (2002) Atlantic water flow through the Barents and Kara Seas. Deep Sea Research Part I: Oceanographic Research Papers 49(12):2281–2298

[178] Schneider W, Budéus G (1995) On the generation of the Northeast Water Polynya. Journal of Geophysical Research: Oceans 100(C3):4269–4286

[179] Sequeiros OE, Naruse H, Endo N, et al (2009) Experimental study on self-accelerating turbidity currents. Journal of Geophysical Research: Oceans 114(C5)

[180] Silvano A, Rintoul SR, Peña-Molino B, et al (2018) Freshening by glacial meltwater enhances melting of ice shelves and reduces formation of Antarctic Bottom Water. Science advances 4(4):eaap9467

[181] Silvano A, Foppert A, Rintoul S, et al (2020) Recent recovery of Antarctic Bottom Water formation in the Ross Sea driven by climate anomalies. Nature Geoscience, 13, 780–786

[182] Silvano A, Purkey S, Gordon AL, et al (2023) Observing Antarctic bottom water in the Southern Ocean. Frontiers in Marine Science 10:1221701

[183] Simpson JE (1982) Gravity currents in the laboratory, atmosphere, and ocean. Annual Review of Fluid Mechanics 14:213–234

[184] Smith SD, Muench RD, Pease CH (1990) Polynyas and leads: An overview of physical processes and environment. Journal of Geophysical Research: Oceans 95(C6):9461–9479

[185] Smith Jr WO, Barber D (2007) Polynyas: Windows to the world, vol 74. Elsevier

[186] Snow K, Sutherland BR (2014) Particle-laden flow down a slope in uniform stratification. Journal of Fluid Mechanics 755:251–273

[187] Socolofsky SA (2001) Laboratory experiments of multi-phase plumes in stratification and crossflow. PhD thesis, Massachusetts Institute of Technology

[188] Stirling I (1997) The importance of polynyas to marine mammals and birds. Journal of Marine Systems 10(1–4):9–21

[189] Stuecker MF, Bitz CM, Armour KC, et al (2018) Polar amplification dominated by local forcing and feedbacks. Nature Climate Change 8(12):1076–1081

[190] Sutherland DA, Pickart RS (2008) The East Greenland coastal current: Structure, variability, and forcing. Progress in Oceanography 78(1):58–77

[191] Swift JH, Aagaard K, Malmberg SA (1980) The contribution of the Denmark Strait overflow to the deep North Atlantic. Deep Sea Research Part A Oceanographic Research Papers 27(1):29–42

[192] Talley LD (2002) Salinity patterns in the ocean. The Earth system: physical and chemical dimensions of global environmental change 1:629–640

[193] Talley LD (2013) Closure of the global overturning circulation through the Indian, Pacific, and Southern Oceans: Schematics and transports. Oceanography 26(1):80–97

[194] Tamura T, Ohshima KI, Nihashi S (2008) Mapping of sea ice production for Antarctic coastal polynyas. Geophysical Research Letters 35(7)

[195] Tanimoto Y, Ouellette NT, Koseff JR (2020) Interaction between an inclined gravity current and a pycnocline in a two-layer stratification. Journal of Fluid Mechanics 887:A8

[196] Tarasov L, Peltier W (1997) A high-resolution model of the 100 ka ice-age cycle. Annals of Glaciology 25:58–65

[197] Thielicke W, Sonntag R (2021) Particle Image Velocimetry for MATLAB: Accuracy and enhanced algorithms in PIVlab. Journal of Open Research Software 9(1):12

[198] Thoma M, Jenkins A, Holland D, et al (2008) Modelling circumpolar deep water intrusions on the Amundsen Sea continental shelf, Antarctica. Geophysical Research Letters 35(18)

[199] Thompson AF, Heywood KJ (2008) Frontal structure and transport in the northwestern Weddell Sea. Deep Sea Research Part I: Oceanographic Research Papers 55(10):1229–1251

[200] Thompson AF, Stewart AL, Spence P, et al (2018) The Antarctic Slope Current in a changing climate. Reviews of Geophysics 56(4):741–770

[201] Thomson RE, Spear DJ, Krassovski MV, et al (2017) Buoyancy-driven coastal current blocks ventilation of an anoxic fjord on the P acific coast of C anada. Journal of Geophysical Research: Oceans 122(4):2976–2998

[202] Tsironi I, Schlesinger D, Späh A, et al (2020) Brine rejection and hydrate formation upon freezing of NaCl aqueous solutions. Physical Chemistry Chemical Physics 22(14):7625–7632

[203] Ungarish M (2009) An introduction to gravity currents and intrusions. Chapman and Hall/CRC

[204] Ushio S, Wakatsuchi M (1993) A laboratory study on supercooling and frazil ice production processes in winter coastal polynyas. Journal of Geophysical Research: Oceans 98(C11):20321–20328

[205] Vallis GK (2017) Atmospheric and oceanic fluid dynamics. Cambridge University Press, pp 13–14

[206] Van Reeuwijk M, Craske J (2015) Energy-consistent entrainment relations for jets and plumes. Journal of Fluid Mechanics 782:333–355

[207] Van Reeuwijk M, Holzner M, Caulfield C (2019) Mixing and entrainment are suppressed in inclined gravity currents. Journal of Fluid Mechanics 873:786–815

[208] Vaux S, Mehaddi R, Vauquelin O, et al (2019) Upward versus downward non-Boussinesq turbulent fountains. Journal of Fluid Mechanics 867:374–391

[209] Von Karman T (1940) The engineer grapples with nonlinear problems

[210] Vrbka L, Jungwirth P (2005) Brine rejection from freezing salt solutions: A molecular dynamics study. Physical Review Letters 95(14):148501

[211] Vreman A (2004) An eddy-viscosity subgrid-scale model for turbulent shear flow: Algebraic theory and applications. Physics of fluids 16(10):3670–3681

[212] Weijer W, Veneziani M, Stössel A, et al (2017) Local atmospheric response to an open-ocean polynya in a high-resolution climate model. Journal of Climate 30(5):1631–1647

[213] Wells AJ, Hitchen JR, Parkinson JR (2019) Mushy-layer growth and convection, with application to sea ice. Philosophical Transactions of the Royal Society A 377(2146):20180165

[214] Wells M, Nadarajah P (2009) The intrusion depth of density currents flowing into stratified water bodies. Journal of Physical Oceanography 39(8):1935–1947

[215] Wells M, Wettlaufer J (2005) Two-dimensional density currents in a confined basin. Geophysical & Astrophysical Fluid Dynamics 99(3):199–218

[216] Werner H, Wengle H (1993) Large-eddy simulation of turbulent flow over and around a cube in a plate channel. Turbulent Shear Flows 8: Selected Papers from the Eighth International Symposium on Turbulent Shear Flows, Munich, Germany, September 9–11, 1991 pp 155–168

[217] Whitworth III T, Orsi A (2006) Antarctic Bottom Water production and export by tides in the Ross Sea. Geophysical Research Letters 33(12)

[218] Williams G, Bindoff N, Marsland S, et al (2008) Formation and export of dense shelf water from the Adélie Depression, East Antarctica. Journal of Geophysical Research: Oceans 113(C4)

[219] Williams RG, Ceppi P, Roussenov V, et al (2023) The role of the Southern Ocean in the global climate response to carbon emissions. Philosophical Transactions of the Royal Society A 381(2249):20220062

[220] Worster G, Moffatt K, Batchelor G (2000) Perspectives in Fluid Dynamics: A Collective Introduction to Current Research. Cambridge University Press, pp 1–631

[221] Wright SJ, Wallace RB (1979) Two-dimensional buoyant jets in stratified fluid. Journal of the Hydraulics Division 105(11):1393–1406

[222] Yi L, Medina-Elizalde M, Tan L, et al (2023) Plio-Pleistocene deep-sea ventilation in the eastern Pacific and potential linkages with Northern Hemisphere glaciation. Science Advances 9(8):eadd1467

[223] Zhang J, Guo Y, Shen Y, et al (2008) Numerical simulation of flushing of trapped salt water from a bar-blocked estuary. Journal of Hydraulic Engineering 134(11):1671–1676

[224] Zhang W, He Z, Jiang H (2017) Scaling for turbulent viscosity of buoyant plumes in stratified fluids: PIV measurement with implications for submarine hydrothermal plume turbulence. Deep Sea Research Part I: Oceanographic Research Papers 129:89–98

[225] Zhou S, Meijers AJ, Meredith MP, et al (2023) Slowdown of Antarctic Bottom Water export driven by climatic wind and sea-ice changes. Nature Climate Change 13(7):701–709

[226] Zúñiga SL, Balachandar S, Yang Y, et al (2024) Planar wall plumes bounded by vertical and inclined surfaces. Physics of Fluids 36(3)

[227] Zwally HJ (1983) Antarctic sea ice, 1973-1976: Satellite passive-microwave observations, vol 459. Scientific and Technical Information Branch, National Aeronautics and Space

A Entrainment decomposition theory

We consider Reynolds-averaged conservation equations for volume, streamwise momentum, and buoyancy. Adopting the Boussinesq approximation and assuming high-Reynolds-number flow moving on a surface with a slope θ, the governing equations are:

$$\frac{\partial \overline{u}}{\partial x} + \frac{\partial \overline{w}}{\partial z} = 0, \tag{39}$$

$$\frac{\partial}{\partial x}(\overline{u}^2 + \overline{u'^2}) + \frac{\partial}{\partial z}(\overline{w}\,\overline{u} + \overline{w'u'}) = -\frac{1}{\rho_0}\frac{\partial \overline{p}}{\partial x} + \overline{b}\sin(\theta) + \nu\left(\frac{\partial^2 \overline{u}}{\partial^2 x} + \frac{\partial^2 \overline{u}}{\partial^2 z}\right), \tag{40}$$

$$\frac{\partial}{\partial x}(\overline{u}\,\overline{b} + \overline{u'b'}) + \frac{\partial}{\partial z}(\overline{w}\,\overline{b} + \overline{w'b'}) = D\left(\frac{\partial^2 \overline{b}}{\partial^2 x} + \frac{\partial^2 \overline{b}}{\partial^2 z}\right). \tag{41}$$

Here, the mean velocity components ($\overline{u}$, $\overline{w}$) correspond to the directions (x, z) respectively, ν and D are the molecular viscosity and diffusivity, ρ_0 is the density of the surrounding fluid , and $b = g(\rho/\rho_0 - 1)$ is the buoyancy. Multiplying (40) by $2\overline{u}$ and using (39) yields:

$$\begin{aligned} &\frac{\partial}{\partial x}\left(\overline{u}^3 + 2\overline{u'^2}\,\overline{u} + 2\overline{p}\,\overline{u} - 2\nu\frac{\partial \overline{u}}{\partial x}\overline{u}\right) + \frac{\partial}{\partial z}\left(\overline{w}\,\overline{u}^2 + 2\overline{w'u'}\overline{u} - 2\nu\frac{\overline{\partial u}}{\partial z}\overline{u}\right) \\ &= 2\overline{w'u'}\frac{\overline{\partial u}}{\partial z} + 2\overline{u'^2}\frac{\overline{\partial u}}{\partial x} + 2\overline{p}\,\frac{\overline{\partial u}}{\partial x} + 2\sin(\theta)\,\overline{b}\,\overline{u} - 2\nu\left[\left(\frac{\partial \overline{u}}{\partial x}\right)^2 + \left(\frac{\partial \overline{u}}{\partial z}\right)^2\right]. \end{aligned} \tag{42}$$

Integration of (39), (40), (42) and (41) over z between the floor ($z = 0$) and infinity result in

$$\frac{dQ}{dx} = -\lim_{z\to\infty}(\overline{w}), \tag{43}$$

$$\frac{d}{dx}\left(\beta_g M\right) = (\sin(\theta)Ri - C_D)\,\frac{M^2}{Q^2}, \tag{44}$$

$$\frac{d}{dx}\left(\gamma_g \frac{M^2}{Q}\right) = (\delta_g + 2\sin(\theta)Ri\Theta_m)\left(\frac{M}{Q}\right)^3, \tag{45}$$

$$\frac{d}{dx}\left[\Theta_g Ri\left(\frac{M}{Q}\right)^3\right] = 0, \tag{46}$$

where the volume flux, Q, momentum flux M, integral buoyancy B and Richardson number Ri are defined as, respectively

$$Q = \int_0^\infty \overline{u}dz, \quad M = \int_0^\infty \overline{u}^2 dz, \quad B = \int_0^\infty \overline{b}dz, \quad Ri = \frac{BQ^2}{M^2} \quad . \tag{47}$$

The characteristic current width, velocity, and buoyancy are defined as, respectively

$$r_m = \frac{Q^2}{M}, \quad u_m = \frac{M}{Q}, \quad b_m = \frac{BM}{Q^2}. \tag{48}$$

In the momentum equation (44), the drag coefficient is defined as

$$C_D = \left(\frac{u_*}{u_m}\right)^2 = \frac{\nu}{u_m^2}\left(\frac{\partial \overline{u}}{\partial z}\right)_{z=0}. \tag{49}$$

In (44) and (45), $\beta_g = \beta_m + \beta_f + \beta_p + \beta_\nu$, $\gamma_g = \gamma_m + \gamma_f + \gamma_p + \gamma_\nu$, $\delta_g = \delta_m + \delta_f + \delta_p + \delta_\nu$ are profile coefficients, associated with the radial variations of the mean flow (denoted with subscript 'm'), velocity fluctuations (denoted with subscript 'f'), and pressure (denoted with subscript 'p'):

$$\begin{aligned}
&\beta_m \equiv \frac{M}{u_m^2 r_m} \equiv 1, && \beta_f \equiv \frac{1}{u_m^2 r_m}\int_0^\infty \overline{u'^2}dz, && \beta_p \equiv \frac{1}{u_m^2 r_m}\int_0^\infty \overline{p}dz,\\
&\gamma_m \equiv \frac{1}{u_m^3 r_m}\int_0^\infty \overline{u}^3 dz, && \gamma_f \equiv \frac{2}{u_m^3 r_m}\int_0^\infty \overline{u}\,\overline{u'^2}dz, && \gamma_p \equiv \frac{2}{u_m^3 r_m}\int_0^\infty \overline{u}\,\overline{p}dz,\\
&\delta_m \equiv \frac{2}{u_m^3}\int_0^\infty \overline{u'w'}\frac{\partial \overline{u}}{\partial z}dz, && \delta_f \equiv \frac{2}{u_m^3}\int_0^\infty \overline{u'^2}\frac{\partial \overline{u}}{\partial x}dz, && \delta_p \equiv \frac{2}{u_m^3}\int_0^\infty \overline{p}\frac{\partial \overline{u}}{\partial x}dz,
\end{aligned} \tag{50}$$

and those coming from a finite value for viscosity (denoted with subscript 'ν'):

$$\beta_\nu \equiv -\frac{1}{Re}\frac{(\ln Q)}{\xi}, \qquad \gamma_\nu \equiv -\frac{1}{Re}\frac{(\ln M)}{\xi}, \qquad \delta_\nu \equiv -\frac{4\,\epsilon}{Re}, \tag{51}$$

with $dx = r_m d\xi$, $Re = u_m r_m/\nu$ and ϵ defined as

$$\epsilon = \frac{r_m}{2u_m^2}\int_0^\infty \left[\left(\frac{\partial \overline{u}}{\partial x}\right)^2 + \left(\frac{\partial \overline{u}}{\partial z}\right)^2\right] dz. \tag{52}$$

In (46), $\Theta_g = \theta_m + \theta_f + \Theta_D$ with:

$$\theta_m \equiv \frac{1}{u_m b_m r_m}\int_0^\infty \overline{u}\,\overline{b}\,dz, \quad \theta_f \equiv \frac{1}{u_m b_m r_m}\int_0^\infty \overline{w'b'}\,dz, \quad \theta_D \equiv -\frac{1}{Pe}\frac{d(\ln B)}{d\xi}, \tag{53}$$

with $Pe = u_m r_m/D = Re\,Sc$ and $Sc = \nu/D$. Besides, to obtain (46), the following boundary condition: $\partial\overline{b}/\partial z = 0$ is used at the floor ($z = 0$).

By definition of the entrainment coefficient, the radial volume flux of the entrained ambient fluid in (43) is assumed to be proportional to the longitudinal velocity of the current and using (43), it yields

$$\alpha = \frac{-\lim_{z\to\infty}(\overline{w})}{u_m} = r_m\frac{d(\ln Q)}{dx} = \frac{d(\ln Q)}{d\xi}. \tag{54}$$

Combining the equations (54), (44), (45), following the steps of [47], the entrainment coefficient can be written as:

$$\alpha = \alpha_{prod} + \alpha_{C_D} + \alpha_{Ri} + \alpha_{shape}, \tag{55}$$

where

$$\alpha_{prod} = -\frac{\delta_g}{\gamma_g}, \quad \alpha_{C_D} = -\frac{2C_D}{\beta_g}, \quad \alpha_{Ri} = 2\left(\frac{1}{\beta_g} - \frac{\Theta_m}{\gamma_g}\right)\sin(\theta)Ri, \quad \alpha_{shape} = \frac{d}{d\xi}\left(\log\left(\frac{\gamma_g}{\beta_g^2}\right)\right). \tag{56}$$

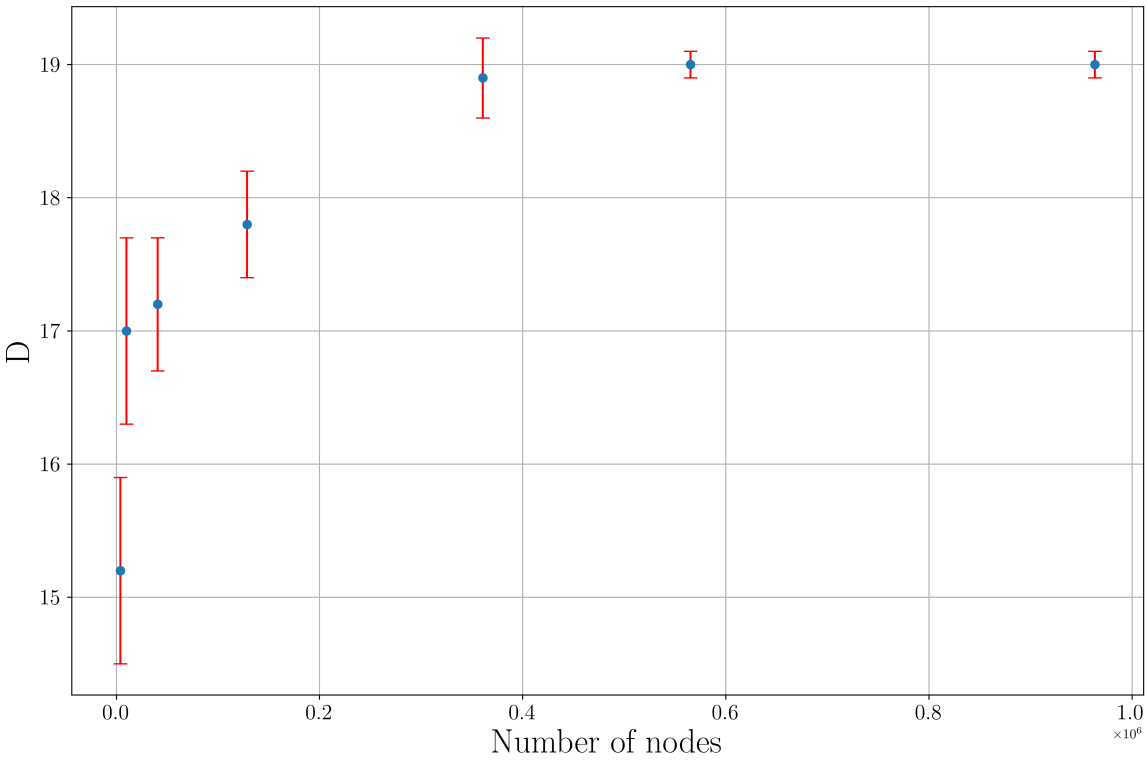

Fig. 65: D as a function of the number of nodes.

B Analysis of the mesh

To analyze the mesh, different simulations are run with varying mesh sizes. If the mesh is well-done, the value of a chosen key parameter should converge with the increasing mesh fineness. Two sets of simulations were performed for the mesh, one to analyze the convergence of D (the depth reached by the gravity current) and one to analyze the convergence of the entrainment coefficient α.

The geometry used was the one described in section (insert section) with Lx=30, Lz=5, θ=20°, and B_l=0.063 m^3 $/s^3$. The simulations to analyze D used a stratification of $N^2 = 0.02$ Hz^2; the simulations for alpha did not use any stratification.

The results can be seen in Figure 65. The values of both D and α converge asymptotically to a final value when the number of nodes is greater than 40000 with this geometry. This number of nodes corresponds to a mesh size of $r_s/4$ close to the wall and $2.8r_s$ far from the wall. In the final simulations, a mesh size of $r_s/6$ close to the wall and $2r_s$ far from the wall was used.

It can be concluded from this analysis that both D and *alpha* converge asymptotically to a final value as the mesh size becomes finer. This means that the mesh can be trusted.

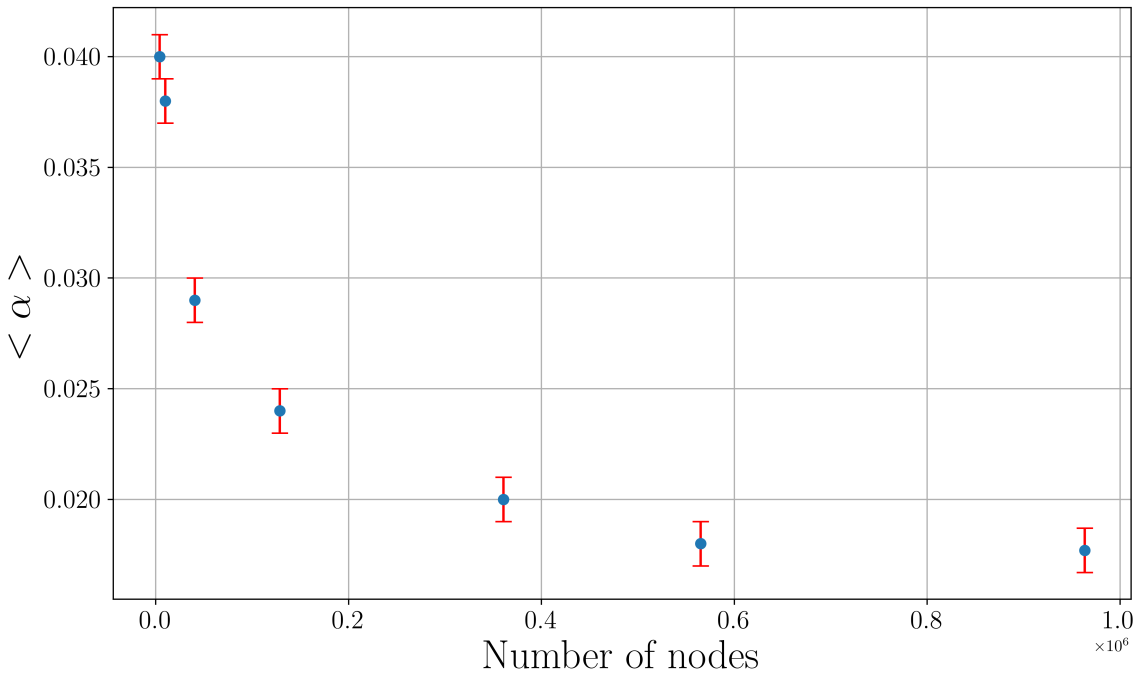

Fig. 66: The entrainment coefficient as a function of the number of nodes.

C Analysis of the LES models and boundary conditions

In the Calif^3-Isis code, there are three LES subgrid models available: the dynamical Smagorinsky, the WALE (Wall), and the Vreman model.

The Smagorinsky model was the first widely used subgrid-scale closure in large-eddy simulation, relying on an eddy viscosity proportional to the local strain rate magnitude (see eq. 27). Although the dynamical Smagorinsky model [73] introduced a scale-dependent, locally computed coefficient that improved accuracy in inhomogeneous and anisotropic flows, it still suffers from excessive damping near solid boundaries unless special treatments are applied. A solution to this problem is to apply a damping function near the wall (also called the wall law) that forces a velocity profile close to the wall. In Calif^3-Isis, this wall law is a model developed by Werner and Wengle [216] (see eq. 30).

The WALE (Wall-Adapting Local Eddy-viscosity) model [140] was developed to ensure correct near-wall scaling of the eddy viscosity without requiring ad hoc damping functions, making it more suitable for wall-bounded flows. In this model, the eddy viscosity is defined as:

$$\mu_s = \rho(C_\omega \Delta)^2 \sqrt{\frac{[\Sigma_{i,j}\overline{\zeta_{ij}\zeta_{ij}}]^{3/2}}{[\Sigma_{i,j}\overline{S_{ij}S_{ij}}]^{5/2} + [\Sigma_{i,j}\overline{\zeta_{ij}\zeta_{ij}}]^{5/4}}} \tag{57}$$

where C_ω is a model parameter, by default the value of C_ω is 0.5, and $\overline{\zeta}$ is defined as:

$$\overline{\zeta} = \frac{1}{2}(\nabla\overline{v}^2 + (\nabla\overline{v}^2)^t) + \frac{1}{3}tr\{\nabla\overline{v}^2\}I \tag{58}$$

Similarly, the Vreman model [211] introduced a mathematically consistent formulation based on the velocity gradient invariants, yielding a nonnegative eddy viscosity and improved robustness in transitional and shear-dominated flows. In this model, the eddy viscosity is defined as:

Table 8: Comparison of penetration depth D for different subgrid-scale models and boundary conditions.

	No-slip	Wall-law
Smagorinsky	18.5	19.0
WALE	19.0	18.5
Vreman	19.2	19.0

$$\mu_s = \rho C_\nu \sqrt{\frac{\beta_{12}\beta_{22} - \beta_{12}^2 + \beta_{11}\beta_{33} - \beta_{13}^2 + \beta_{22}\beta_{33} - \beta_{23}^2}{\overline{S_{ij}S_{ij}}}} \tag{59}$$

where

$$\beta_{ij} = \Sigma_m \Delta_m^2 \overline{S_{mi}S_{mj}} \tag{60}$$

where Δ_m denotes the filter width in the direction m and C_ν is a constant fixed at 0.025.

However, both WALE and Vreman, while avoiding the wall-damping problem compared to Smagorinsky, are not fully consistent with exact wall asymptotics and may still underperform in complex near-wall turbulence.

The modeling of the near-wall flow is a crucial aspect, since gravity currents develop along a solid boundary. In Calif^3-Isis, two types of wall boundary conditions are available: the no-slip condition and the wall-law approach. The wall-law, described by eq. 30, prescribes the near-wall velocity profile through an empirical formulation, while the no-slip condition enforces zero velocity for all components at the wall, leaving the near-wall dynamics to be fully resolved by the computation.

Six simulations were carried out by combining the three LES models with the two wall boundary conditions available in Calif^3-Isis. The simulations were performed for the same flow with $B_l = 0.063$ m^3/s^3, $N^2 = 0.02$ Hz^2, and θ =40°. For each combination of model and boundary condition, the penetration depth was measured, and the results are summarized in Table 8.

Table 8 shows the close agreement between the different subgrid-scale models for the value of D. All values differ by less than 3%, and the four closest results differ by less than 1%. The choice of model and wall law appears to affect the results only marginally. Therefore, the dynamical Smagorinsky model with a wall law was chosen for its simplicity.

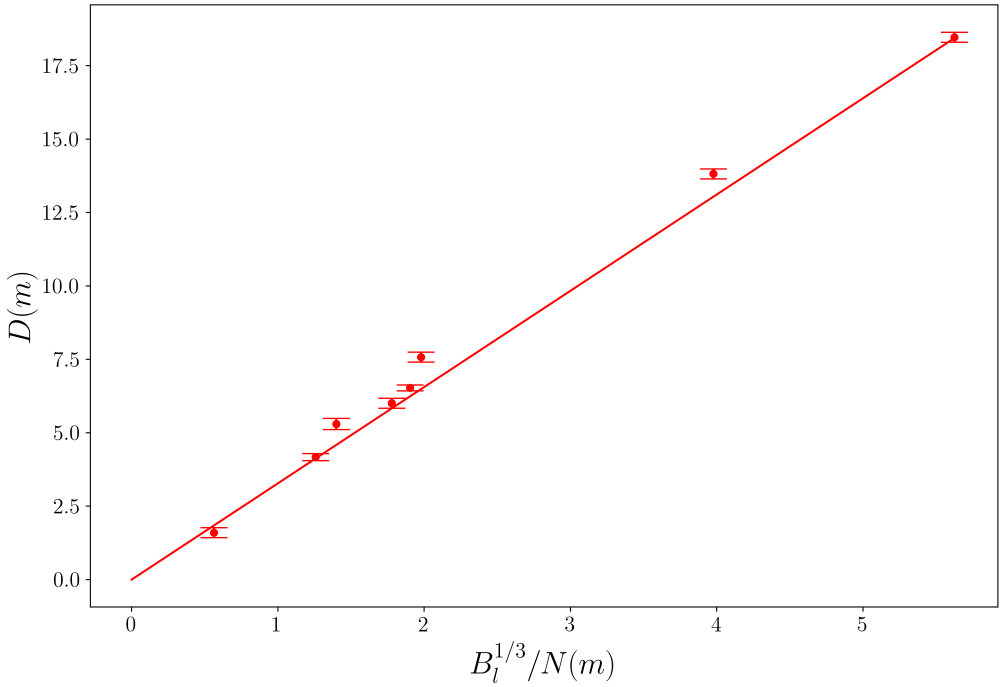

Fig. 67: Verification of the scaling for D.

D Analysis of the scaling for D

A scaling for D (the penetration depth of the gravity current) was introduced in eq. 35 as:

$$D_a = \frac{DN}{B_l^{1/3}}. \tag{61}$$

In Figure 67, verification that this scaling works in our simulations is provided. Different simulations with varying B_l and D were performed, and the resulting values of D were plotted against $B_l^{1/3}/N$. It can be clearly seen that there is a linear relationship that passes through the point [0,0] between D and $B_l^{1/3}/N$. This means that $\frac{DN}{B_l^{1/3}}$ is a constant so we can define a quantity $D_a = \frac{DN}{B_l^{1/3}}$.